Title	A CFD Study on the Propeller-Hull Interaction Flow in Waves Using Body-Force Distribution Model
Author(s)	Tokgoz, Emel
Citation	大阪大学, 2015, 博士論文
Version Type	VoR
URL	https://doi.org/10.18910/53979
rights	
Note	

Doctoral Dissertation

A CFD Study on the Propeller-Hull

Interaction Flow in Waves Using Body-Force

Distribution Model

Emel Tokgöz

June 2015

Graduate School of Engineering,

Osaka University

TABLE OF CONTENTS

List of symbols

α : Angle of attack ($\alpha = \psi - \beta i$)

α_0 : Zero lift angle ($\alpha_0 = {H_e}/{2\pi n r} - \psi$)

β_i : Hydrodynamic pitch angle

γ : Circulation density

Γ : Circulation

Δt : Time increment

Δx : Grid spacing in x direction

ζ : Free surface elevation (m)

η : Open water propeller efficiency

λ : Wave length (m)

ν : Kinematic viscosity

ν_t : Eddy viscosity

ρ : Water density (Kg m^{-3})

ψ : Geometric pitch angle

ω : Wave frequency (s^{-1})

ω_e : Encounter frequency (s^{-1})

A : Wave amplitude=wave height h/2 (m)

A_0 : Disk area of propeller

A_e : Expanded area of propeller

AP : Aft perpendicular

B : Beam length of the ship=Bwl (m)

Bwl	: Maximum beam at the waterline (m)
c	: Chord length of the propeller blade
C_B, CB	: Block coefficient
C_D	: 2-Dimensional drag coefficient
C_L	: 2-Dimensional lift coefficient
C_M	: Midship Coefficient
C_W	: Water plane area coefficient
dL, dD, dT, dQ	: Segmental lift, drag, thrust and torque (in order)
dP_x, dP_θ	: Pressure jump in axial and tangential direction
d	: The distance between propeller centerline and solid-surface
D	: Propeller diameter
D	: Experimental data
$E\%D$	: Comparison Error $(S_d\text{-}D)/D*100$
F_0	: External force (N)
Fb_x, Fb_y, Fb_z	: Body-force components in x, y and z directions
Fb_θ	: Body-force component in tangential direction
f_e	: Encounter frequency=$2\pi\omega_e$
F_y, F_z	: Side and vertical force coefficients
FP	: Forward perpendicular
Fr	: Froude number based on ship length
g	: Gravity (m/s^2)
H	: Geometric pitch of the propeller
H_e	: Effective pitch of the propeller
I	: Immersion depth of the propeller

I_x, I_y, I_z	: Moment of inertia around x, y and z axis
J	: Advance coefficient$=U_0/(n_d{*}D)$; n_d: propeller's rotational speed in rps
k	: Wave number
k_1	: Correction factor for blade to blade interaction
k_t	: Turbulent kinetic energy (m^2 s^{-2})
K	: Spring stiffness (N m^{-1})
K, M, N	: Moments in ship coordinate
K_t	: Thrust coefficient
K_q	: Torque coefficient
K_{XX}, K_{YY}, K_{ZZ}	: Radius of gyration (m)
L	: Ship length= Lpp (m)
L_s	: Half of the minimum spacing
LCB	: Longitudinal center of buoyancy (%)
Lpp	: Ship length between perpendiculars (m)
m	: Total mass of the moving parts (Kg)
n	: Non-dimensional number of revolutions
N	: Number of propeller blades
$\hat{p}$	: Piezometric pressure
p, q, r	: Roll, pitch and yaw angular velocity
Q	: Q-criterion
Q_x, Q_y, Q_z	: Propeller moments in x, y and z direction
r_e	: Radius of the representative blade section
R	: Propeller radius
R_B	: Hub radius

Re	: Reynolds number
$Reff$	: Effective Reynolds number
S	: Wet propeller area
S_o, S_∞	: Total propeller area
S_d	: Simulation value
S_{ij}	: Strain rate
t	: Time (s)
T	: Ship draft (m)
T_e	: Encounter period (s)
T_x, T_y, T_z	: Propeller forces in x, y and z direction
U_0	: Ship speed (m s^{-1})/free stream velocity
u_N	: Volume average axial velocity
U_r	: Resultant inflow velocity at propeller plane
U_t	: Tangential velocity at propeller plane
w_a	: Axial induced velocity at propeller plane
W_{ij}	: Vorticity tensor
w_n	: Total induced velocity at propeller plane
w_t	: Tangential induced velocity at propeller plane
w_x, w_y, w_z	: Vorticity in x, y and z directions
x	: Surge motion (m)
x, y, z	: x, y, z location in Cartesian coordinate system
X	: Hydrodynamic force (N)
X, Y, Z	: Forces in ship coordinate
u, v, w	: (1) Velocity component in flow field (m s^{-1})

(2) Surge, sway and heave velocity (m s^{-1})

List of tables

List of figures

THIS PAGE IS INTENTIONALLY LEFT BLANK

CHAPTER 1: INTRODUCTION

The computation of the flow field around the self-propelled ship is getting to be more essential to understand the propulsive efficiency in waves or in connection with maneuvering motion. For that reason, it is important to use a propeller model which can provide a correct propeller-hull-rudder interaction that gives an accurate prediction of self-propulsion parameters. There are two options to model a propeller if the RANS (Reynolds Averaged Navier-Stokes) code is used; one is based on a viscous method and another on inviscid method. Based on a viscous method, hull, rudder and propeller geometries are solved in the RANS grid, so they turn out to be parts of the viscous flow solution. The flow is a complex transient flow around a rotating propeller, so high mesh resolution is required around the propeller blade to capture the transient flow features. Thus, it complicates the grid generation and increases the computational cost significantly. The viscous approach is applied by Carrica et al. (2012), to study the mechanism of broaching for a model surface combatant in following regular waves by using discretized rotating propellers. So, it is known that the present CFD (Computational Fluid Dynamic) codes can handle the flow filed around a rotating propeller. These methods are very effective for the detailed propeller performance prediction using effective velocity field and advanced propeller code. However, if the real geometry and the rotation of the propeller are treated in CFD code using a sliding mesh, computation takes long time due to the difference in non-dimensional time (Carrica et al., 2012). Therefore, those methods are not easy to be applied to the iterative geometry manipulation, which is very important for the design process.

The inviscid method is applied when the detailed propeller flow is not essential for some studies like interaction of propeller-hull-rudder system. But, the important point here is to represent the propeller in the velocity field. In this case, the acceleration produced in the flow by the propeller blades can be represented by a body-force propeller model without the need of physical propeller geometry. The inviscid approach can be divided into two, which are prescribed and interactive models, in terms of how the propeller model is coupled with the RANS solver. In the prescribed body-force approach, the body-force terms are calculated once and put into RANS solver and the interaction of the propeller and hull is ignored. The axisymmetric prescribed body-force distributions based on ship speed or modified ship speed using effective wake fraction in calm water are usually used for a free running ship model. Therefore, the side force produced by propeller cannot be treated in the equation of motions. In an interactive model, the propeller and RANS codes interact with each other towards a solution and in this way the effective propeller inflow can be taken into account. Lifting line type, vortex lattice method and surface singularity potential flow models are some of the examples for the propeller models based on interactive approach.

Stern et al. (1988a) used a prescribed body-force model based on an actuator disk approach for the computation of the propeller-hull interaction, where the radial circulation distributions are based on the Hough and Ordway circulation distribution (Hough and Ordway, 1964) which has zero loading at the root and tip. Also, the interactive body-force distributions were calculated using a vortex based lifting surface method. The initial validation studies were carried out for the computation around propeller-shaft configurations (Stern et al., 1988b) and the Iowa axisymmetric body (Stern et al., 1991) using an interactive calculation procedure. After the publication of

Stern et al. (1988a), many researchers applied the same approach to propeller-hull interaction computations (Piquet et al, 1987, Yang et al., 1990, Dai et al., 1991 and Zhang et al., 1991). However, the researchers mentioned except Zhang et al. (1991), followed a non-interactive approach to include the propeller effects with prescribed body-force distributions. Briefly, many different propeller models ranging from prescribed models to interactive models are used to implement the body-force fields into RANS code.

1.1 OBJECTIVE

The main objective of this dissertation is to develop a new body-force model for the rotating propeller within viscous flow code. The basic concept is that the output velocity field at propeller plane (e.g. total velocity field including the interaction velocity field between the wake flow and induced velocity field) from CFD code is directly used to compute the thrust and the torque distributions in infinite blade assumption. Thus, it is very similar as the CFD methods to predict the thrust and torque using Kyushu University Method (KUM), an inviscid code, which uses a simplified quasi-steady blade element theory (BET) with the infinite-bladed propeller model (e.g. time averaged propeller induced velocity field, including finite blade number effect etc.) (Yamazaki, 1977). Yamazaki propeller model is based on the lifting line theory. In this theory, the propeller is simplified by a propeller plane without thickness and modelled by bound vortex sheets on the plane and free vortices shed from the tip and root to the downstream of the propeller. The number of vortex line/lifting line is the number of blades, so-called finite blade theory.

In calm water computations for propulsion, many researchers use the inviscid

propeller code and iterative procedure based on the propeller model, but they usually assume the shape of vortex system and the position where they calculate the induced velocity field to be subtracted from total velocity field to predict the effective inflow velocity (Simonsen and Stern, 2005). The effective velocity field is used to determine the thrust and torque distribution and again to calculate the induced velocity field to get the effective inflow velocity. It assumes the induced velocity field in CFD code is the same as the computed induced velocity field by inviscid code. On the other hand, extracting the right total velocity field is not easy because RANS solver works in three-dimensional grid block with a thickness, where the Yamazaki model is based on a two-dimensional cylindrical plane without thickness as shown in Fig. 1.1. The fluid velocity ($U(X)$) increases by ΔU (induced by propeller) over the thickness Δx of the RANS propeller block/disk as seen in Fig. 1.1. The total velocities are interpolated in the middle of the disk (X_p) because the velocity increases through the disk is approximately linear related to the x-direction (Simonsen and Stern, 2005). Several iterations between Yamazaki model and RANS are required to make sure the effective wake is converged.

In KUM, the thrust and torque distribution are calculated by BET using the total velocity (induced velocity calculated by infinite bladed wake helical vortex field is added to effective velocity) (Yamazaki, 1977). From this method, the total velocity in CFD code using quasi-steady body-force distribution seems to be used to predict the thrust and torque distribution (e.g. body-force distribution). Therefore, this concept is tried in this dissertation. Basically, the present method can be applied to any CFD code used recently. However, for the first attempt to apply this method, the computations are done for uniform flow case. By the results, it is validated that the new concept using total velocity can be applied. Of course, it is well-known that the effective velocity concept is not

4

required in uniform flow, but it seems that the total velocity can be verified.
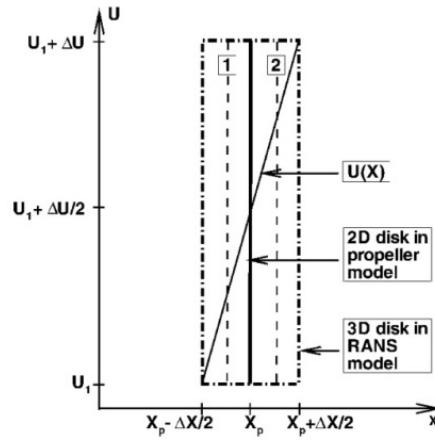
Fig. 1-1 Linear induced velocity subtraction (Simonsen and Stern, 2005).

This method in a viscous flow code is equivalent to KUM in potential flow theory. Within this approach, the inflow velocity components, including induced velocity effect by time averaged infinite bladed vortex system shed by propeller blade, to the propeller are determined by CFD code and thrust and torque distributions are calculated by BET with some modification similar to the potential flow theory (Benini, 2004). Therefore, the potential flow code is not required in the proposed method.

The other important objectives of this dissertation can be listed as:

- Studying the effect of free surface on flow around a rotating propeller to investigate the applicability of new body-force concept.

- Computation of the diffraction problem of fully-loaded KVLCC2 ship model with forward speed in regular head waves with wave lengths $\lambda/L=0.6$, 1.1 and 1.6 by coupling the new body-force propeller model with RANS code CFDSHIP-IOWA.

- Predicting the motions of KVLCC2 in fully-loaded condition in regular head

waves with wave lengths λ/L=0.6, 1.1 and 1.6 and its propeller performance by coupling the new body-force propeller model with the RANS code CFDSHIP-IOWA. Investigation of the complicated flow field around the self-propelled ship in waves and comparing wake flow with the PIV (Particle Image Velocimetry) measurements.

1.2 OVERVIEW OF THIS DOCUMENT

This dissertation consists of several chapters with increasing complexity. First of all, the development of a new body-force propeller model, which is treated as the infinite-bladed propeller model (time averaged propeller induced velocity field) with a simplified quasi-steady BET, is described. The applicability of this new body-force model is investigated by studying the effect of free surface on flow around a rotating propeller. Further, the forward speed diffraction problem of fully-loaded KVLCC2 tanker at Fr=0.142 in regular head waves is discussed numerically by using this body-force model. Finally, the motions of KVLCC2 at Fr=0.142 in regular head waves with wave lengths λ/L=0.6, 1.1 and 1.6 are predicted by using the proposed body-force propeller model.

Brief summaries of chapters are given as follows:

Chapter 2 presents the development of a new body-force model for the rotating propeller within viscous flow code and its application to uniform flow and propeller advancing with the angle of attack. The detailed mathematical formulation of the model, grid generation and the computational outline are explained. The model presented here aims to reduce the computational effort while keeping the effect of ship with motion in quasi-steady manner for propeller. Open water characteristics of the simulation results

are compared with the data obtained from the literature. In the further chapters, this body-force model will be applied for propeller-hull related flow problems.

Chapter 3 introduces the effect of free surface on the flow around a rotating propeller by varying the propeller immersion depth to investigate the applicability of the proposed body-force method. The computational method, grid generation and the computational outline are explained. Propeller open-water characteristics are simulated in still water for different immersion depths for the Modified-AU type fixed-pitch propeller. The propeller open characteristics are compared with the experimental data for validation. The results of the propeller inflow and the propeller wake are discussed in detail.

Chapter 4 discusses the ship forward speed diffraction problem numerically because of its importance to predict the ship motions in wave fields. The proposed body-force propeller model is coupled with the RANS code CFDSHIP-IOWA to study the forward speed diffraction problem of the KVLCC2 model tanker in fully-loaded condition. The test conditions, ship and propeller geometry are explained. Also, the CFD method (CFDSHIP-IOWA V4.5) utilized in the current work is described in detail. Herein, the propeller boss effect is also counted in. The simulations are done for the ship advancing at design Froude number Fr=0.142 under regular head waves with the same wave amplitude and three different wavelengths, which represents short waves, long waves and wavelength with maximal added resistance. The computations are also carried out without propeller for the same cases to analyze the propeller effect on the flow field. The results are discussed at the end.

Chapter 5 presents the prediction of the motions and the propeller performance of KVLCC2 model tanker at Fr=0.142 in regular head waves with wavelengths λ/L=0.6, 1.1 and 1.6 using proposed body-force propeller model. The body-force propeller model is

coupled with the RANS code CFDSHIP-IOWA. The experiment conducted in the towing tank of Osaka University, including the PIV measurement for the wake field is briefly explained. The complicated flow field around the self-propelled ship in waves is investigated and the wake flow is compared with the PIV measurements. The simulation results for the thrust and time histories are compared with the PIV measurement results.

Chapter 6 summarizes the development of the new body-force propeller model and the application of it for propeller-hull related flow problems, supplemented with possible future research.

1.3 CONTRIBUTIONS

The new body-force propeller model developed in this dissertation addresses the above mentioned problems. As it is stated, various body-force propeller models have been proposed to reduce computational cost, which assist self-propelled ship simulations. But, to predict the self-propulsion condition or the free running prediction with maneuvering motion, the present method seems to be used easily and the computed velocity field includes the deformation effect of wake vortex system due to motion. And, the output velocity field at propeller plane from CFD code is directly used to compute the thrust and the torque distributions in infinite blade assumption.

The contributions of this dissertation can be listed as:

- Simple calculation of body-force is achieved by very simple subroutine which significantly reduces the computational cost.

- Proposed body-force model can be implemented on the polar type of grid and Cartesian type of grid (Yokota et al., 2013) which proves the application

flexibility of the method to any grid point.

- Implementation of the body-force propeller model is convenient considering the free surface modeling.

- Side forces produced by the propeller can be treated in the momentum equations.

- Propeller body-forces interacting with flow field solver and propeller forces/moments are considered in the 6DOF (Degrees of freedom) solver.

CHAPTER 2: DEVELOPMENT OF A BODY-FORCE PROPELLER MODEL

In this chapter, I present the development of a new body-force model for the rotating propeller within viscous flow code and its application to the uniform flow and a propeller advancing with angle of attack. The solid-surface effect on the propeller loading and power is also investigated. A simplified quasi-steady blade element theory with the infinite-bladed propeller model (time averaged propeller induced velocity field) is coupled with a RANS code to determine the thrust and the torque distributions. The model presented here aims to reduce the computational effort while keeping the effect of ship with motion in quasi-steady manner for propeller. Open-water validation simulations are done for the Modified-AU methodical type fixed-pitch propeller. Further, this body-force model will be employed for propeller-hull related flow problems.

2.1 INTRODUCTION

BET was established as a computational tool to predict the propeller performance using the CFD output velocity components at propeller plane. BET is based on the assumption that each element of a propeller can be considered as an airfoil segment. The propeller blade with radius R, is divided into 50 sections in radial direction and the sections are divided equally ($dr=(R-R_B)/50$, where R_B is the propeller boss radius). The lift (L) and drag (D) forces are then calculated from the resultant velocity, which is expressed by Eq. (1), acting on the airfoil. The variables in the following equations and

figures are non-dimensioanlized by propeller radius R, free stream velocity U_0 and the water density ρ and their combinations. Velocities and forces acting on a blade element are shown in Fig. 2.1.
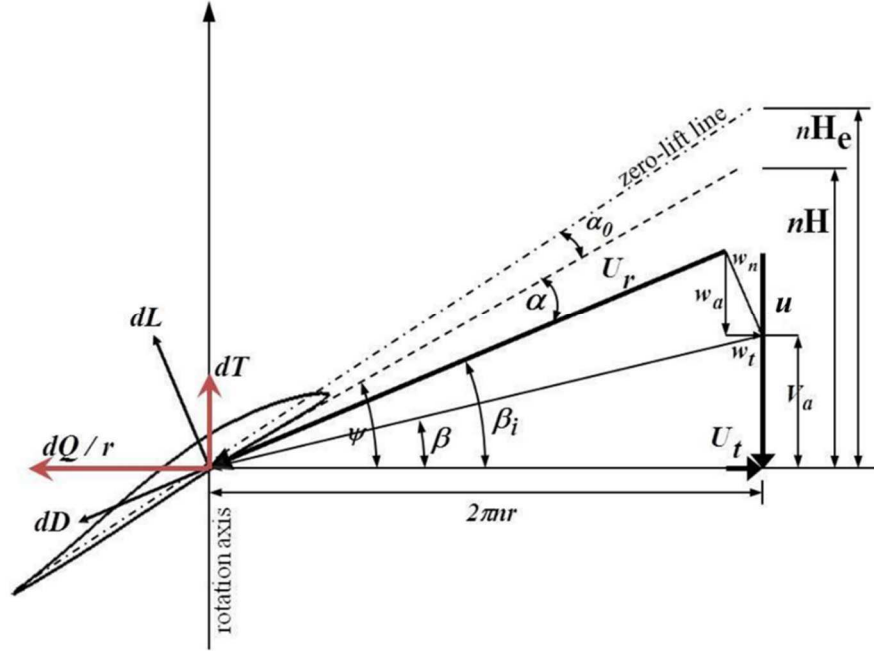
Fig. 2-1 Forces acting on a blade element.

The equations solved at each radial segment are given as;

$$U_r = \sqrt{(u)^2 + (2\pi nr - U_t)^2}, \tag{1}$$

where u is the axial velocity including induced velocity in CFD code and U_t is the tangential velocity including induced velocity in CFD code, n is the non-dimensional number of revolutions of the propeller. The axial induced velocity is represented by w_a and the tangential induced velocity is represented by w_t in Fig. 2-1. The total induced velocity is obtained as $w_n = \sqrt{w_a{}^2 + w_t{}^2}$. Note that the induced velocities are not known in the condition with ship. So, induced velocities are not used in this chapter.

$$\text{hydrodynamic pitch angle: } \beta_i = arctan\left(\frac{u}{2\pi nr - U_t}\right), \tag{2}$$

$$C_L = 2\pi k_1 \sin(\alpha + \alpha_0), \tag{3}$$

$$k_1 = 1.07 - 1.05\left(\frac{c(r_e)}{R}\right) + 0.375\left(\frac{c(r_e)}{R}\right)^2, \tag{4}$$

where r_e is the radius of the representative blade section,

$$C_D = \text{ drag coefficient}, \tag{5}$$

$$dL = 0.5C_L U_r^2 c(r) dr, \tag{6}$$

$$dD = 0.5C_D U_r^2 c(r) dr, \tag{7}$$

$$dT = dL\cos\beta_i - dD\sin\beta_i, \tag{8}$$

$$dQ = (dL\sin\beta_i + dD\cos\beta_i)r, \tag{9}$$

$$dP_x = \frac{dT\text{N}}{2\pi r dr}, \tag{10}$$

$$dP_\theta = \frac{dQ\text{N}}{2\pi r^2 dr}, \tag{11}$$

$$Fb_x = \frac{dT}{\Delta x}\frac{\text{N}}{2\pi r dr}, \tag{12}$$

$$Fb_\theta = \frac{dQ}{\Delta x}\frac{\text{N}}{2\pi r^2 dr}, \tag{13}$$

where Δx is the grid spacing in axial direction at body-force point and N represents the number of blades.

Two dimensional sectional lift coefficient of the propeller blade is calculated using Eq. (3) by taking into account the effect of blade to blade interaction and so on. This effect is included as a correction factor k_1, which is calculated by Eq. (4) (Yamazaki, 1977). Also, two dimensional sectional drag coefficient of the propeller blade is assumed to be 0.01. The effective pitch (H_e) is taken as 1.08 times of the geometric pitch of the propeller (H). Velocities (including propeller induced effect) on the propeller blade are calculated within RANS code, thus the potential flow code is not required in the proposed method as mentioned in Chapter 1. The chord length and the pitch distribution of the propeller are

used within this theory. Similar as the infinite bladed theory, the time averaged circulation density is calculated at one position as $\gamma = Nd\Gamma/2\pi rdr$. Thus the time averaged local pressure jump in axial and tangential direction are expressed by Eq. (10) and (11) multiplied by the number of blades and they are considered to act uniformly over the sector corresponding to each radial slice (dr). Finally, the body-forces (force/volume) acting in radial and angular direction on the propeller plane are computed by Eq. (12) and (13), respectively. The body-forces acting in y and z direction are calculated by $Fb_y = Fb_\theta cos\beta_i$ and $Fb_z = Fb_\theta sin\beta_i$, in sequence. The overall thrust (T) and torque (Q) of the rotor are obtained by integrating the individual contribution of each element, shown in Eq. (8) and Eq. (9), along the radius of the propeller using Eq. (14) (Benini, 2004).

$$T = \int_0^{2\pi} \int_{R_B}^{R} Fb_x \Delta x r dr d\theta, \quad Q = \int_0^{2\pi} \int_{R_B}^{R} Fb_\theta \Delta x r^2 dr d\theta \qquad (14)$$

2.2 COMPUTATIONAL METHOD

2.2.1 Grid Generation

The computational grid and the coordinate system used for the flow field calculations in the cases of uniform flow and static drift are shown in Fig. 2-2. The grid was generated primarily with consideration of the propeller location and the propeller wake. The propeller is located at the origin (x=0). Equal grid spacing covering the propeller boundary, was used on the yz plane. For the rest, geometric progression was used. The minimum grid spacing Δx is taken as $0.01R$. The computational domains for all cases which are non-dimensionalized by R, represented in Table 2-1.
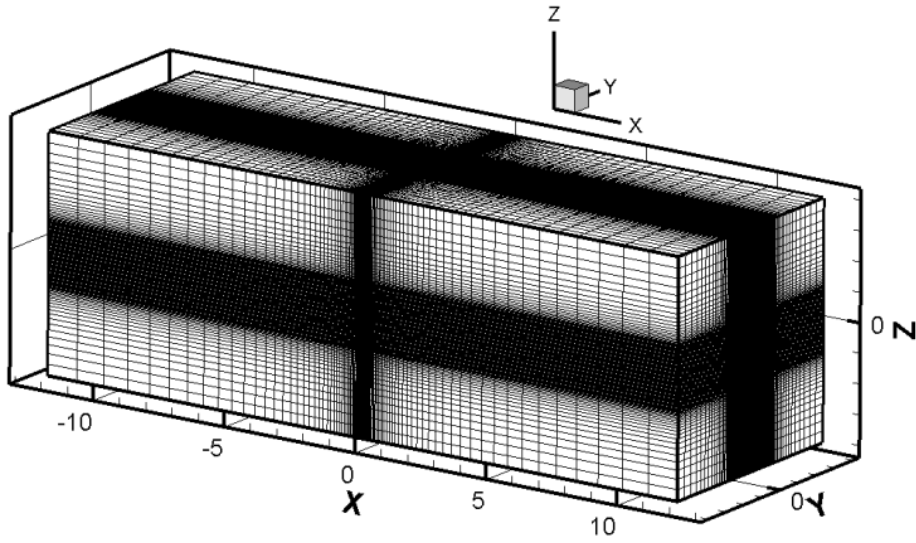
Fig. 2-2 Computational grid and coordinate system.

Table 2-1 Computational domain and grid points.

Case	Uniform flow & Static drift	Solid-surface (1)	Solid-surface (2)
Grid points (ξ^1 x ξ^2 x ξ^3)	101x111x111	101x111x95	101x111x88
computational domain length	24 (-12 — 12)	24 (-12 — 12)	24 (-12 — 12)
computational domain width	8 (-4 — 4)	8 (-4 — 4)	8 (-4 — 4)
computational domain depth	8 (-4 — 4)	5.2 (-4 — 1.2)	5 (-4 — 1)

For studying the solid-surface effect (see Subsection 2.3.3) on the propeller loading and power, the computational grid was regenerated in z direction. The grid was regenerated according to the solid-surface level. The important point to study the solid-surface effect on propeller loading is that the surface level should go through the stream tube contraction as seen in Fig. 2-3. Herein, two different grids were regenerated for the cases d/D=0.6 (solid-surface case-1) and d/D=0.5 (solid-surface case-2), where the distance

between the solid-surface and the propeller centerline is denoted by d in Fig. 2-3 and the propeller diameter is expressed by D. Equal grid spacing was used covering the propeller boundary as in uniform flow case and above the propeller reaching to the solid-surface level. In this case, above the propeller the grid is denser than the previous case which allows us to study the flow field in detail.
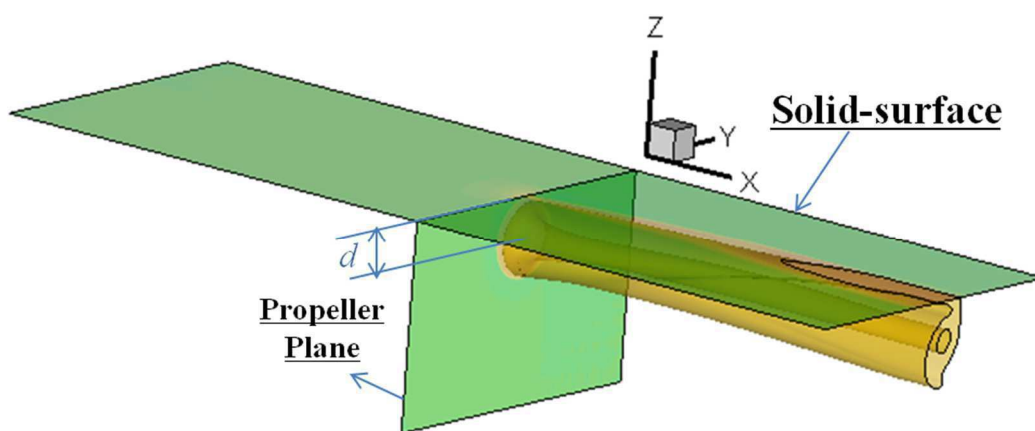
Fig. 2-3 Solid-surface presentation.
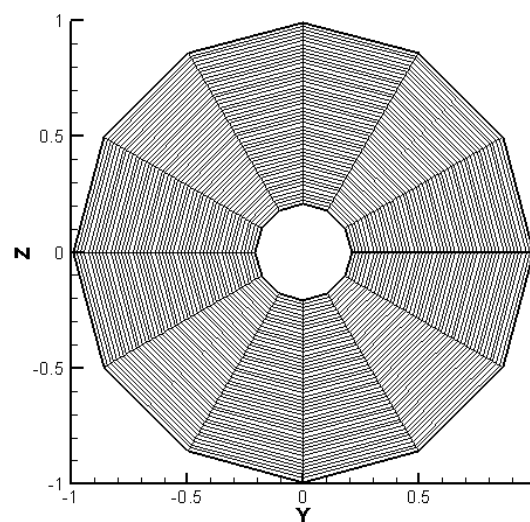
Fig. 2-4 Polar coordinate system on the propeller plane (x=0).

The propeller disc is divided into 50 radial and 12 circumferential sections for body-force calculations. The polar coordinate system on the propeller plane is shown in Fig. 2-4. In total 663 grid points were used. This polar coordinate system is just used for body-force calculations by BET. As it will be mentioned in Subsection 2.2.2, the velocity components on the propeller plane are transformed from the Cartesian coordinate system which is shown in Fig. 2-2, to polar coordinate system.

2.2.2 Computational Outline

The finite difference and finite element methods are the most commonly used numerical methods to solve the Navier-Stokes equations. On the other hand, finite analytic method (FAM) which is introduced by Chen et al. (1990) has better stability properties than the conventional methods at high Reynolds numbers. In the CFD method, 12-points Finite Analytic Method (FAM) for space discretization and the Euler implicit scheme for time discretization are used along with the PISO (Pressure-Implicit Splitting Operator) algorithm for velocity pressure coupling. The sub-grid scale (SGS) turbulence model is used as a zero-equation turbulence model to avoid the divergence in the computations. A simplified SGS turbulence model in the form of eddy viscosity is applied to resolve the complicated 3D vortical flow, which determines the forces and moments. The eddy viscosity is derived as;

$$v_t = L_s{}^2 \sqrt{2\bar{e}_{ij}\bar{e}_{ij}} \tag{15}$$

where,

$$e_{ij} = \frac{1}{2}\left(\frac{\partial u^i}{\partial x^m}\delta^{mj} + \frac{\partial u^j}{\partial x^n}\delta^{in}\right), \ \frac{1}{Reff} = \frac{1}{Re} + v_t \tag{16}$$

x^i is the Cartesian coordinate and L_s (length scale) is the half of the minimum spacing

and *Reff* is the effective Reynolds number (Ohmori, T. and Miyata, H., 1993).

For Cartesian coordinate systems, the momentum equations and the continuity equation in tensor representation are shown as;

$$\frac{\partial u_i}{\partial t} + \left(u_j - \frac{\partial v_t}{\partial x_j}\right)\frac{\partial u_i}{\partial x_j} - \frac{\partial v_t}{\partial x_j}\frac{\partial u_j}{\partial x_i} = -\frac{\partial p}{\partial x_i} + \frac{1}{Reff}\left(\frac{\partial^2 u_i}{\partial x_j \partial x_j}\right) + Fb_i, \qquad (17)$$

$$\frac{\partial u_i}{\partial x_i} = 0 \qquad (18)$$

where $u_i=(u,\ v,\ w)$ are the Reynolds-averaged velocity components, $x_i=(x,\ y,\ z)$ are the independent coordinate directions and $Fb_i = \left(Fb_x,\ Fb_y,\ Fb_z\right)$ are the non-dimensional body-force terms which represents the time-averaged influence of the propeller on the fluid in the propeller region in *x, y* and *z* directions, respectively.

The Modified-AU methodical series with 145.65-mm diameter, constant pitch, zero skew, 6-deg rake, 5 blades, and MAU n=25 sections were used for the experiments. The detailed propeller geometry offsets and wing section offsets can be found in (Yazaki, 1961, p. 10&13). Within the computations, the values are non-dimensionalized with the propeller radius (*R*). The velocity components are transformed from Cartesian coordinate system by linear interpolation to the polar coordinate system (Fig. 2-4) within the global iterations to compute the body-force terms on the propeller plane as seen in the flowchart in Fig. 2-5. The tangential velocity U_t is computed using *v* and *w*, in CFD code. After transforming the velocity components, the body-force distributions are calculated using BET as indicated in Section 2.1. Following, the body-force distributions are transformed back to Cartesian coordinate system by linear interpolation and included in the momentum equations in Eq. (17).

At first, the computations were carried out using the same boundary conditions and flow parameters by introducing the body-force terms just on the propeller plane (Tokgoz

et al., 2012). The minimum grid spacing Δx was taken as $0.05R$ and equal grid spacing covering the propeller boundary was used on the yz plane, but the number of grid points and the computational domain are kept the same. The axial-velocity was plotted approximately at $0.7R$ of the propeller along the x axis as shown in Fig. 2-7 and fluctuations were observed around the propeller plane. Within the BET, k_1 correction factor is modified to tune the thrust values. Therefore, the body-force terms are distributed into five planes as shown in Fig. 2-6 (a), while including them in the source functions of the momentum equations. The body-force terms are multiplied with a coefficient for corresponding planes as shown in Fig. 2-6 (b). In this figure the red lines represent the planes in x direction. This distribution of the body-force terms is called distributed body-force model in this research. Figure 2-7 shows that after distributing the body-force, the axial-velocity increases smoothly as expected. The dashed lines represent the axial-velocity for the distributed body-force model. Likewise, the pressure distribution becomes continuous in relation to the axial-velocity distribution. Figure 2-8 presents the axial velocity contours on the propeller plane and the pressure distribution around the propeller plane when the advance coefficient J=0.9091 (Left: body-force model, Right: distributed body-force model). And, it shows that axial velocity contours on the propeller plane, correspond with the graph shown in Fig. 2-7. For the distributed body force model, the velocity is less than the previous model. The pressure distribution along x axis for distributed body force propeller model is more continuous. Eventually, the computations in this research were done with the distributed body force model and the results will be shown related to this model.
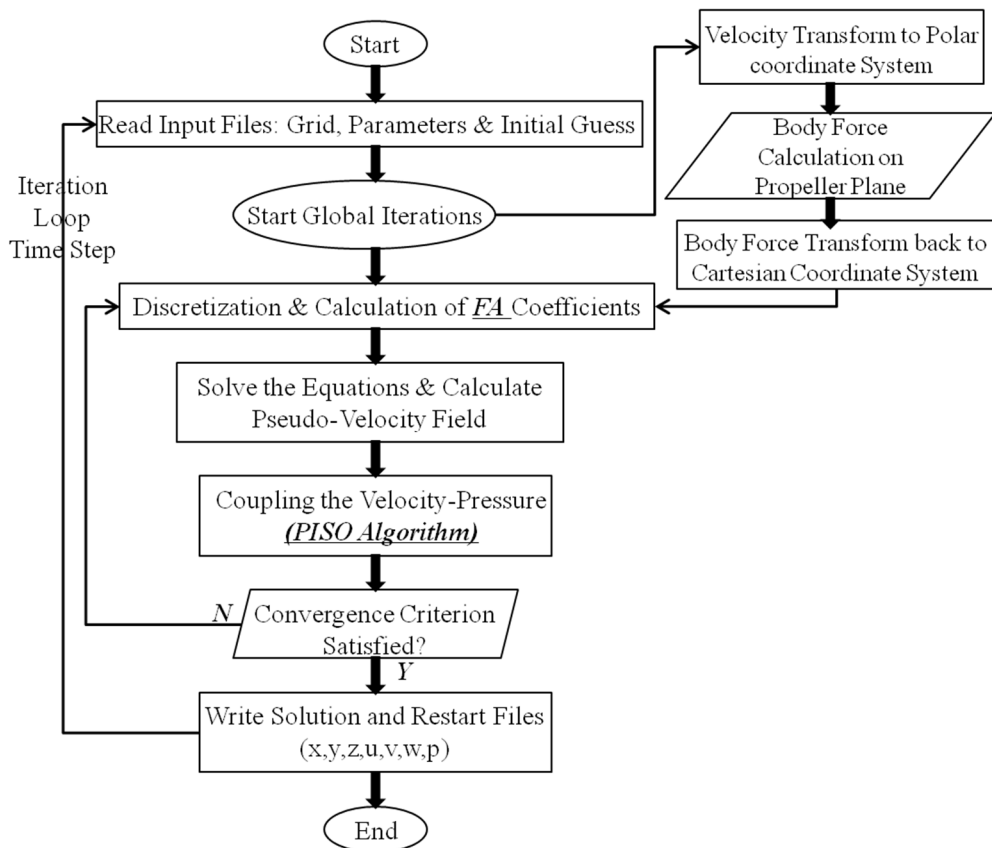
Fig. 2-5 Computational flowchart.

(a)   (b)
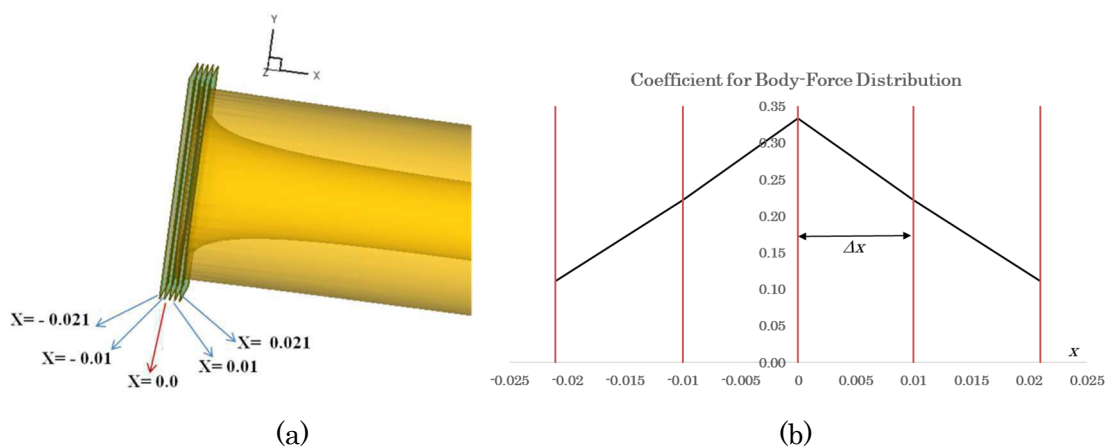
Fig. 2-6 (a) Plane positions for distributing the body-force.

(b) Coefficient for body-force distribution.
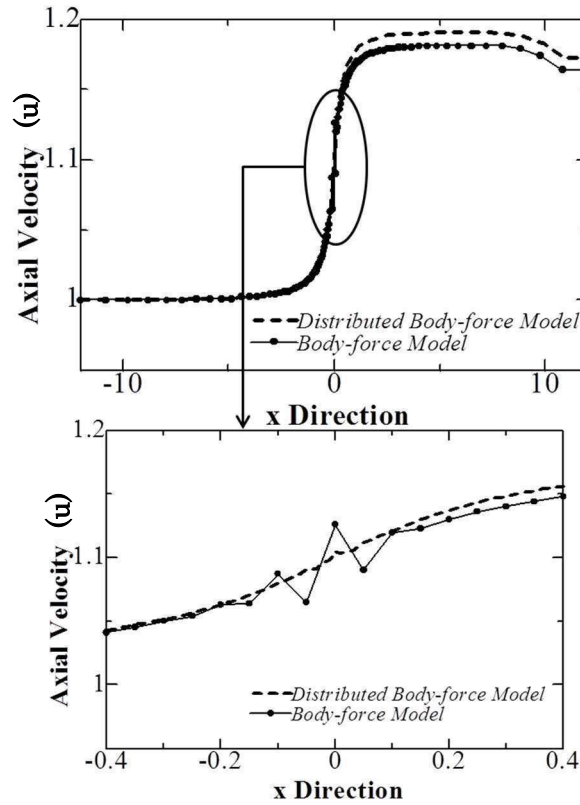
Fig. 2-7 Axial velocity graphs J=0.9091.

Total number of global iterations and time steps used were 80 and 1500, respectively. The time increment (i.e., Δt) was chosen as 0.01. As a convergence criterion, residual for all the variables was set to 10^{-4}.
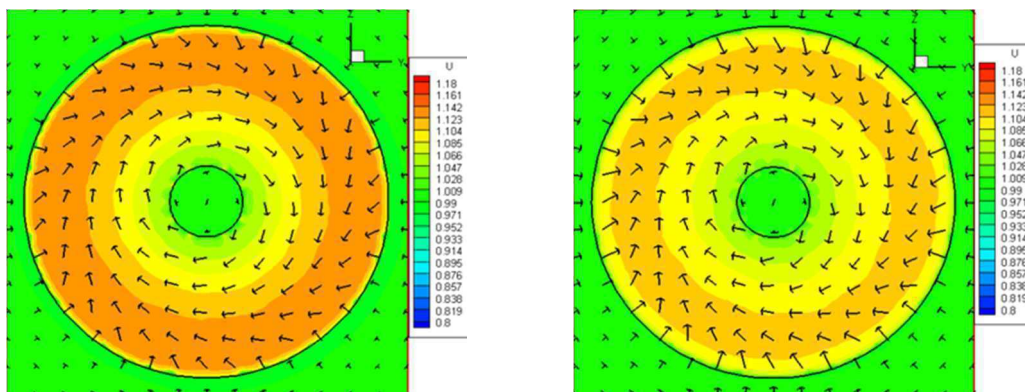
Axial-velocity contours and cross plane vectors
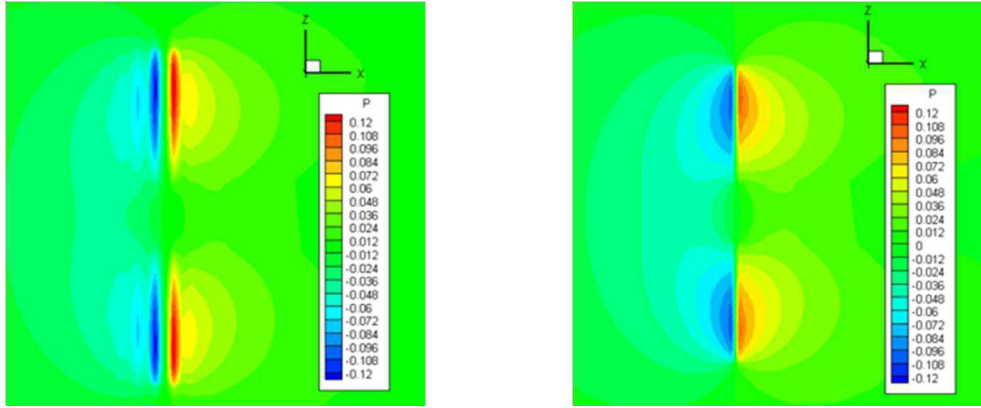
Pressure distribution

Fig. 2-8 Axial velocity contours and pressure distribution for Left: Body-force model, Right: Distributed body-force model.

2.3 RESULTS

2.3.1 Uniform Flow Case

The flow corresponding to the propeller open test was computed using the flow parameters Re=10,000 (laminar flow) and Fr=0.0. The free surface effect is not included in the simulations for this subsection. Uniform velocity was applied at all the external boundaries except the outlet and zero-gradient conditions for velocity and pressure were applied at the outlet (i.e., x=12) as boundary conditions. Computations were carried out for several number of revolution of the propeller. The non-dimensionalized number of revolution ($n = n_d R/U_0$, where n_d is the number of revolutions in per second) used for the first computation was n=0.464 and the corresponding advance coefficient was J=1.08. The advance coefficient for the first computation was chosen corresponding to nearly zero thrust value on the open water curve. The result of this flow computation was used

for the next increased number of revolutions of the propeller after satisfying the convergence criterion for thrust and torque coefficients. Therefore, the propeller performance could be predicted for various advance coefficient values.

Body-force represents the pressure jump in the axial direction. The negative pressure is observed for region upstream and positive pressure is observed downstream of the propeller as shown in Fig. 2-9 for n=0.8 and the corresponding J=0.625. Note that the effect of propeller hub is ignored in the present chapter.

The flow characteristics are analyzed by illustrating axial-velocity contours and cross plane vectors. The axial-velocity contours and cross–plane vectors for J=0.625 are shown in Fig. 2-10. As it can be seen, the axial velocity starts increasing in the upstream and reaches its maximum value soon in the downstream due to the induced velocities. The cross-plane vectors for the upstream region of the propeller show the stream tube contraction. The stream tube contraction is formed as a result of the change in the axial momentum. The rotational motion can be observed in the downstream region of the propeller.
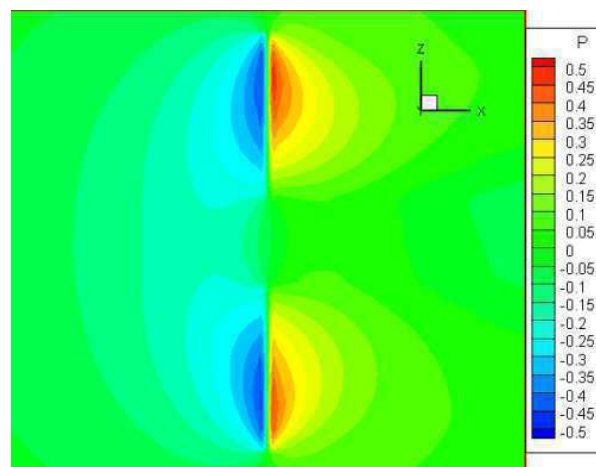
Fig. 2-9 The pressure distribution at J=0.625.
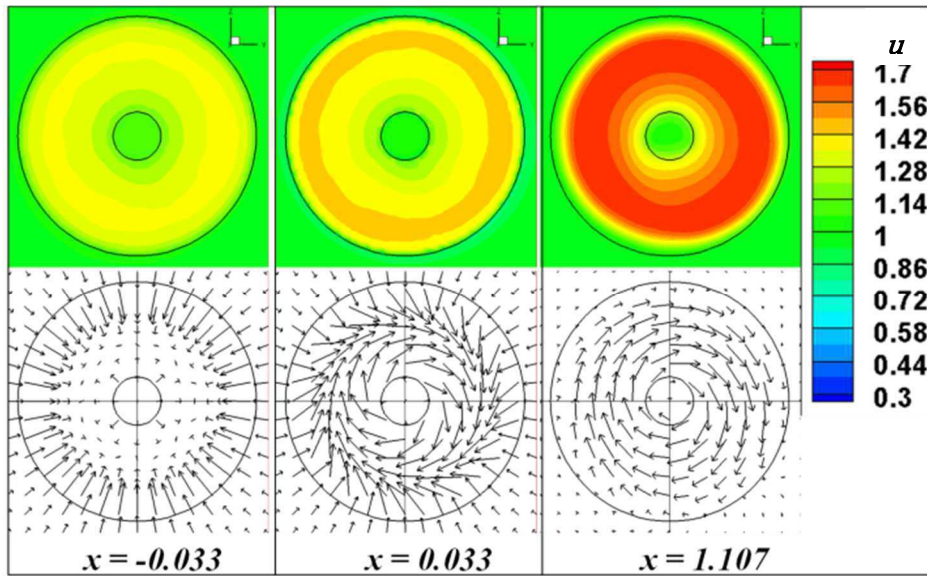
Fig. 2-10 Axial velocity contours and cross plane vectors at J=0.625.

The body-force distributions on the propeller plane in x, y and z directions are illustrated in Fig. 2-11 (a), (b) and (c), respectively. The axial-velocity contours correlate with the axial body-force distributions (Fb_x).

The iso axial-velocity surface, when the axial velocity is equal to 1.45, is illustrated in Fig. 2-12 for n=0.8. The induced velocities increase as a result of the increased propeller loading and have an unsteady influence on the propeller slipstream. So, the twisting is recognized when the propeller loading was increased.

(a)   (b)   (c)
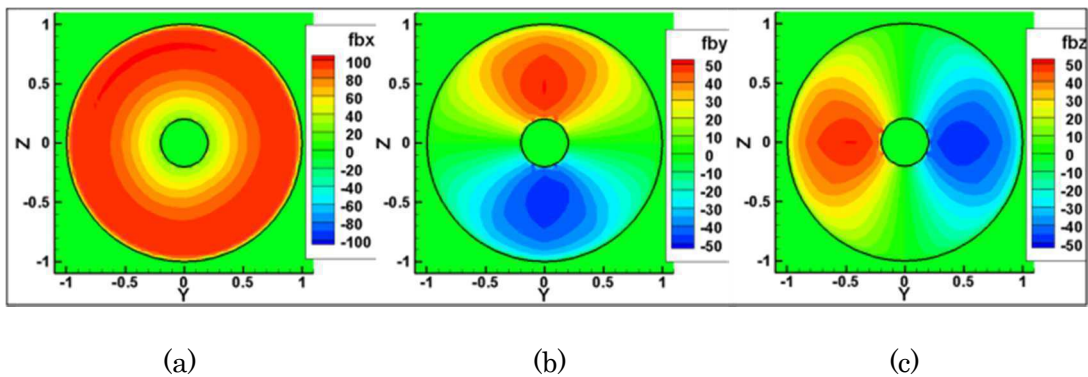
Fig. 2-11 Body-force distributions on the propeller plane (when J=0.625).
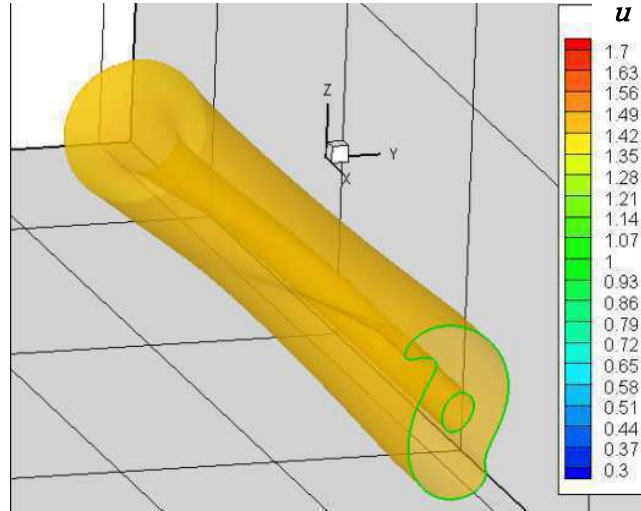
Fig. 2-12 Iso axial velocity surface when u=1.45.

After the propeller plane, the flow field is not potential due to vorticities generated by the propeller. Thus, the velocity field resulted from the computations was used within Eq. (19) to Eq. (21) to calculate the vorticity components in (x, y, z) directions.

$$w_x = \frac{\partial w}{\partial y} - \frac{\partial v}{\partial z} \tag{19}$$

$$w_y = \frac{\partial u}{\partial z} - \frac{\partial w}{\partial x} \tag{20}$$

$$w_z = \frac{\partial v}{\partial x} - \frac{\partial u}{\partial y} \tag{21}$$

The axial-vorticity contours and vectors for n=0.95 are demonstrated in Fig. 2-13. As it is seen, near the hub there is a negative vorticity and near the tip region of the propeller there is a strong positive vorticity. In the far downstream region where x=1.107 as shown in Fig. 2-13 (c), the vorticity near the blade tip dissipates while it reduces. As for the hub vorticity, we can observe the similar effect due to the lack of the hub geometry. By looking at the vectors, the bound vortex sheet in the radial direction on the propeller

plane (x=0, Fig. 2-13 (a)) is captured. Also, the free vortex shed from the propeller is seen. From the 3D vortex field, the stream traces are plotted near the blade tip and the hub as shown in Fig. 2-14. The inner one is the hub vorticity. As is it seen, the trajectory of a fluid particle, passing through the propeller blade close to the tip region, changes as a function of advance coefficient. Small disturbances occur in the case of a smaller J (larger number of revolutions). The bound vortex sheet is arranged in radial direction on the propeller disk and the free vortex shed from it is seen in this figure. The vortex sheet shed from the propeller is assumed to be in a helical form. The flow field on and behind the propeller disk is non-potential as a result of the vortices generated by the propeller itself. Thus, the induced velocities occur due to the vortices.

(a)   (b)   (c)
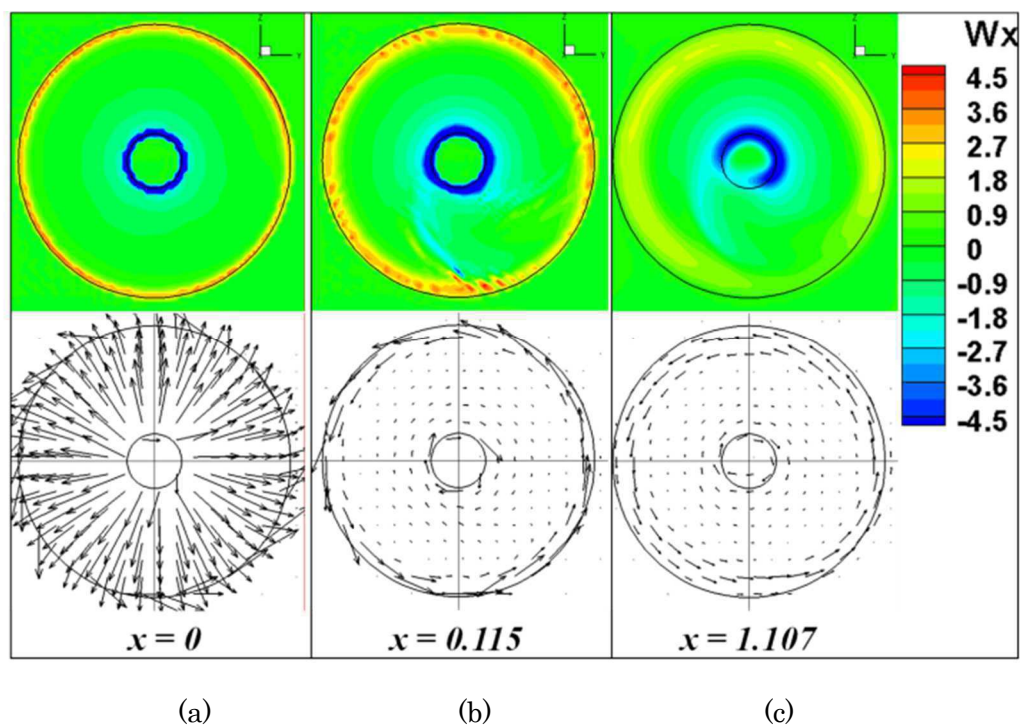
Fig. 2-13 Axial vorticity contours and vectors.
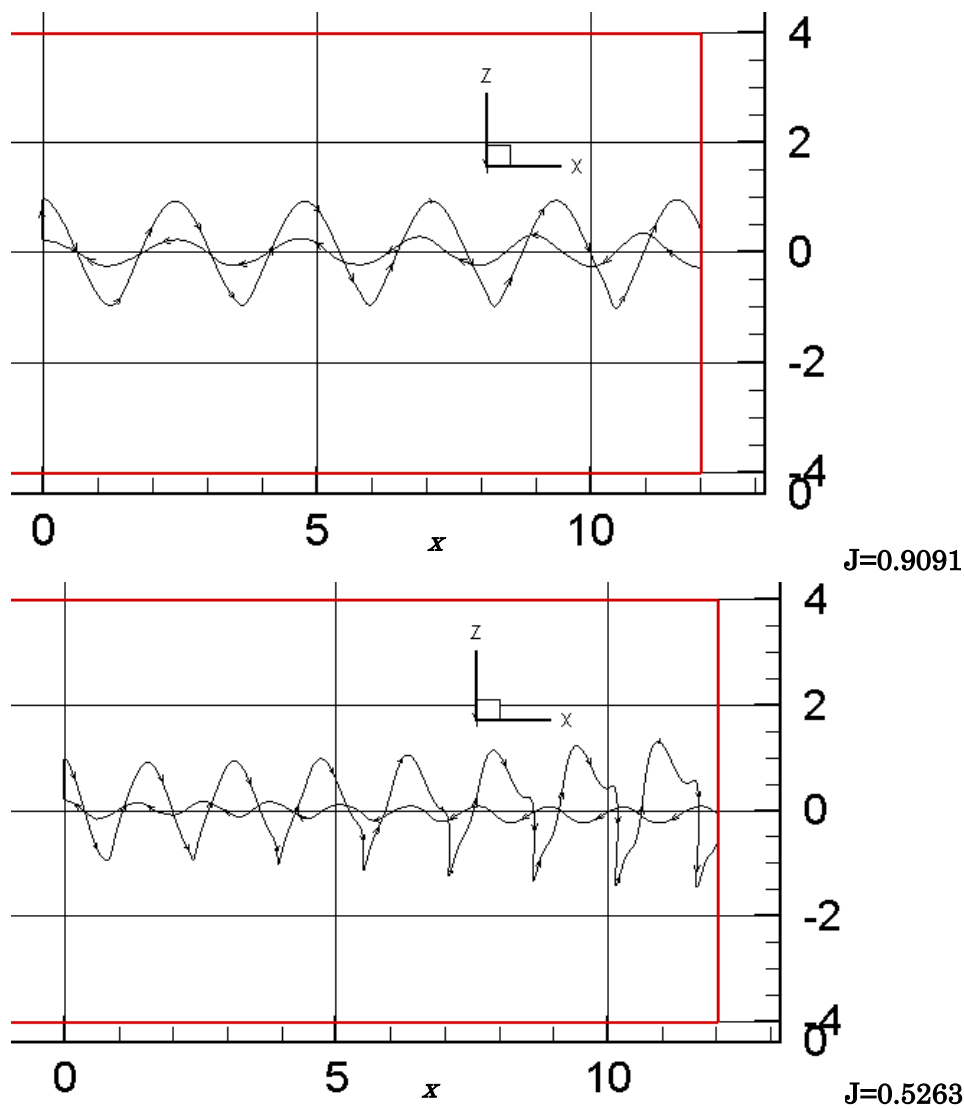
Fig. 2-14 The stream traces at different values of the advance coefficient.

2.3.2 Static Drift Case

The proposed body-force model was also used for the propeller advancing with an angle of attack (α). Figure 2-15 illustrates the static drift case. The computations were performed for three different side flow cases; v=0.1, 0.2 and 0.3 which are 10%, 20% and 30% of the uniform flow, respectively. The boundary conditions were modified according to side flow values. The computations for static drift case were carried out for low loading

case when J=0.9091 (n=0.55).

The increased side flow can be observed by looking at the cross-plane vectors in positive y direction in Fig. 2-16. It is presented in Fig. 2-16 that the axial-velocity distributions are not symmetric due to the asymmetrical force distribution. It is seen that the drift of the flow becomes more significant as the angle of attack increases. After the propeller plane, in the slipstream, the rotational flow is observed as expected.
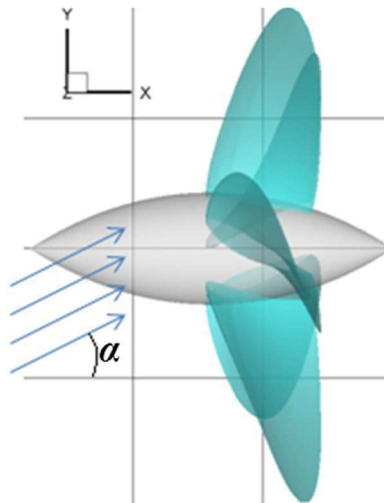
Fig. 2-15 Side flow representation.

The longitudinal force distributions differ as a result of the side flow. In Fig. 2-17, the body distributions in x- and y- directions on the propeller plane are illustrated for the propeller advancing with two individual angle of attack values and a zero angle of attack. For the latter, the body-forces are distributed symmetrically as seen in Fig. 2-17 (a); so in terms of Fb_y and Fb_z the negative and positive forces cancel each other out. Thus, for the uniform flow case there is no side flow acting. Side forces were calculated from the body-force distributions in y-direction. When the side flow velocity is 10% of the uniform flow velocity (Fig. 2-17 (b)), the non-dimensionalized side force is calculated by

Eq. (22) as $T_y=$ -0.0426 and $T_y=$ -0.08574 is computed while v=0.2 (Fig. 2-17 (c)). And for v=0.3, T_y=-0.1292. According to the calculations, the side force increases as a result of the increased side flow. Above all, the calculated side forces values are non-ignorable, thus it is believed that this method can be used for ship to ship interaction computations.

$$T_y = \int_0^{2\pi} \int_{R_B}^{R} Fb_y \Delta x r dr d\theta \qquad (22)$$

Iso axial-velocity surfaces at J=0.9091 which corresponds to the number of revolutions n=0.55, are illustrated in Fig. 2-18 when u=1.13. The drifting of the stream tube is clearly seen. Due to the increased axial-velocity, drifting angle is a little bit smaller than expected.

The thrust and torque coefficients raised slightly for static drift cases with reference to the uniform flow computation results along with the increased angle of attack values as seen in Table 2-2.

Table 2-2 Comparison of the open water characteristics of the static drift cases.

Case	n	J	T	Q	K_t	$10K_q$
v=0	0.55	0.9091	0.53669	0.22648	0.11089	0.23397
v=0.1	0.55	0.9091	0.53815	0.22654	**0.11119**	0.23403
v=0.2	0.55	0.9091	0.54587	0.2278	**0.11278**	0.23533
v=0.3	0.55	0.9091	0.56035	0.23037	**0.11577**	0.23799
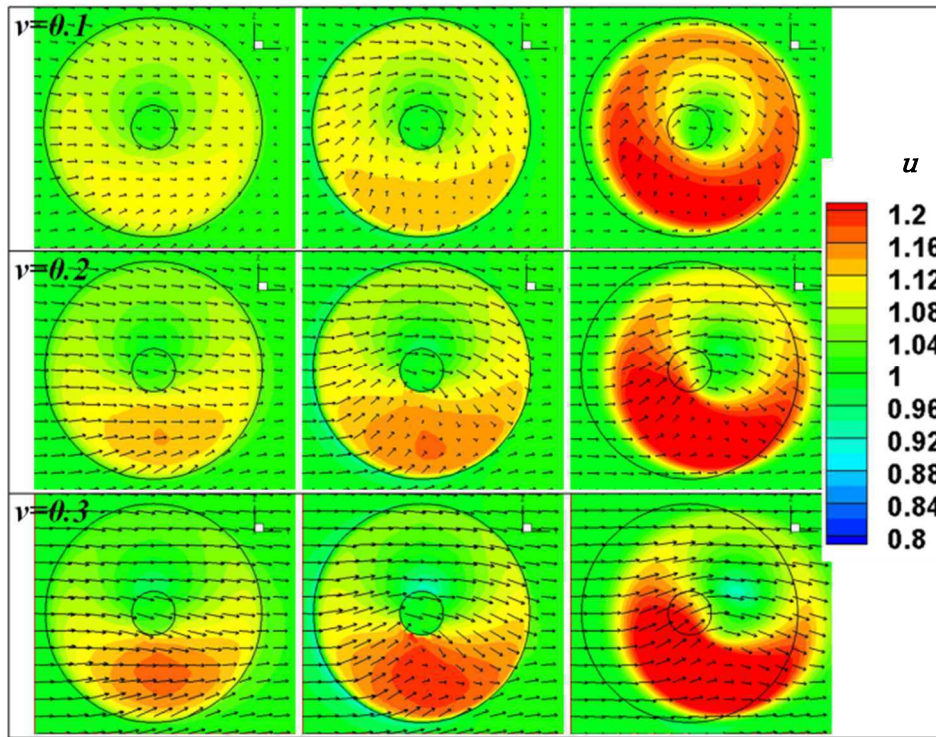
(a) x=-0.033   (b) x=0.033   (c) x=1.107

Fig. 2-16 Axial velocity contours and cross plane vectors (when J=0.9091).
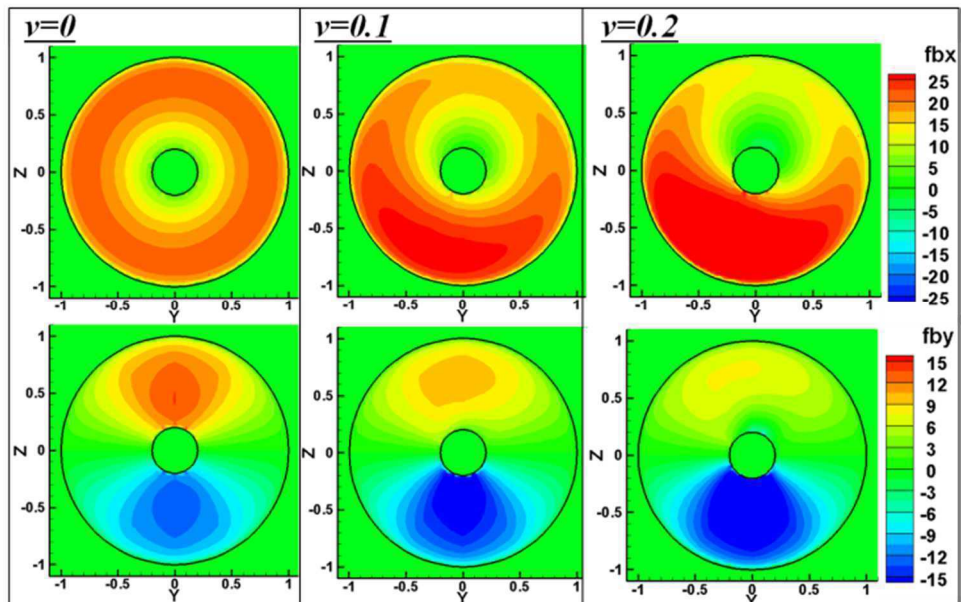
(a)   (b)   (c)

Fig. 2-17 Body-force distributions (J=0.9091).

Top view of the stream tubes
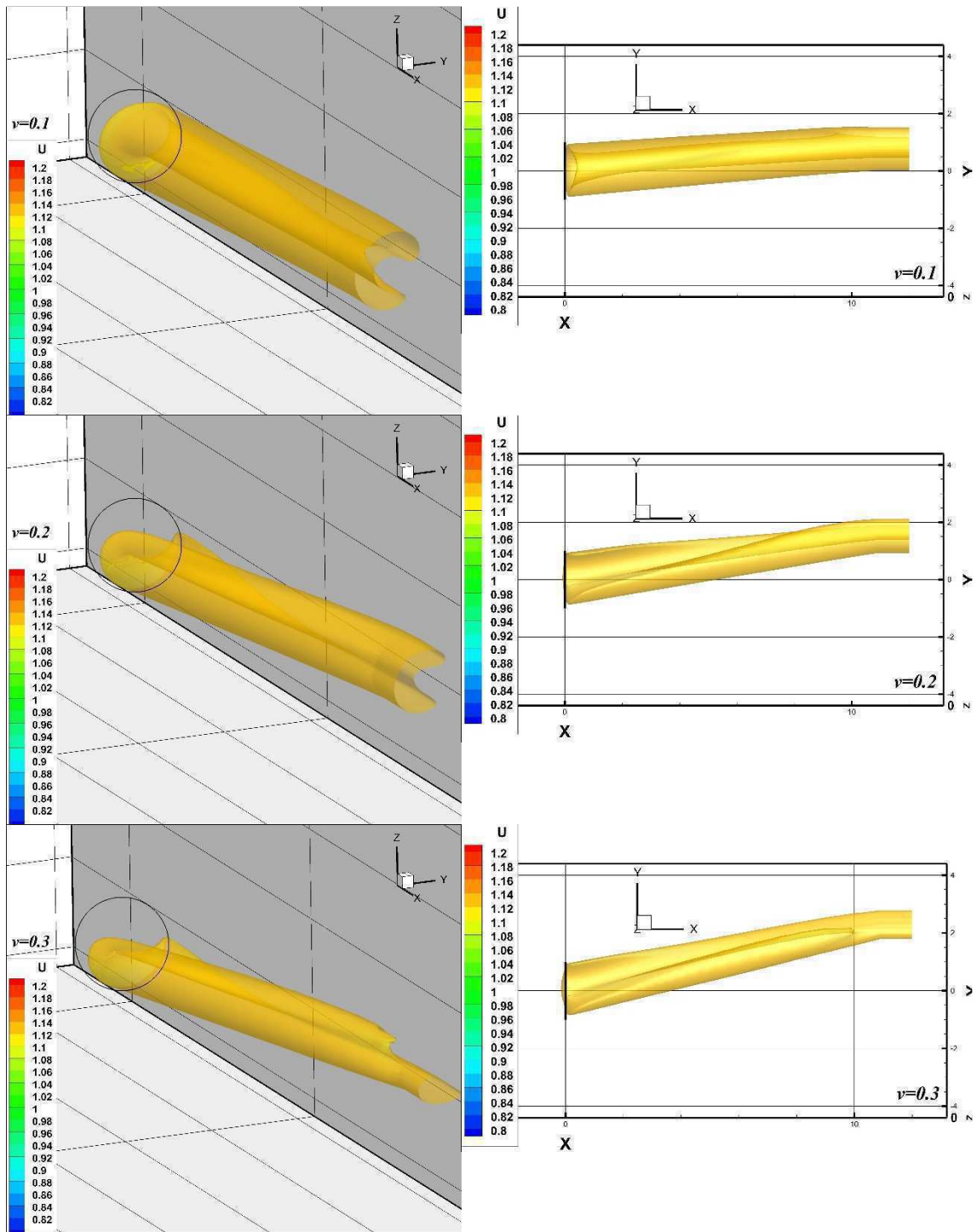
Fig. 2-18 Iso axial velocity surfaces at J=0.9091 for static drift case when *u*=1.13.

2.3.3 Solid Surface Case

The effect of the varying propeller immersion on the propeller loading and power is studied as well. The computations were run for two loading cases while d/D=0.6 and d/D=0.5 (solid-surface at the propeller tip). The longitudinal body-force and the induced velocity distributions on the propeller plane are not symmetric as shown in Fig. 2-19. While the solid-surface level is lessened, the axial-velocity and body-force decrease close to the solid-surface region. Also it is seen in Fig. 2-19 (c) that tangential induced velocities increase near the solid-surface level. The propeller loading decreases in accordance with the decreased body force near the solid-surface region. For higher loading cases, the reduction of the propeller performance is more obvious.

(a)   (b)   (c)
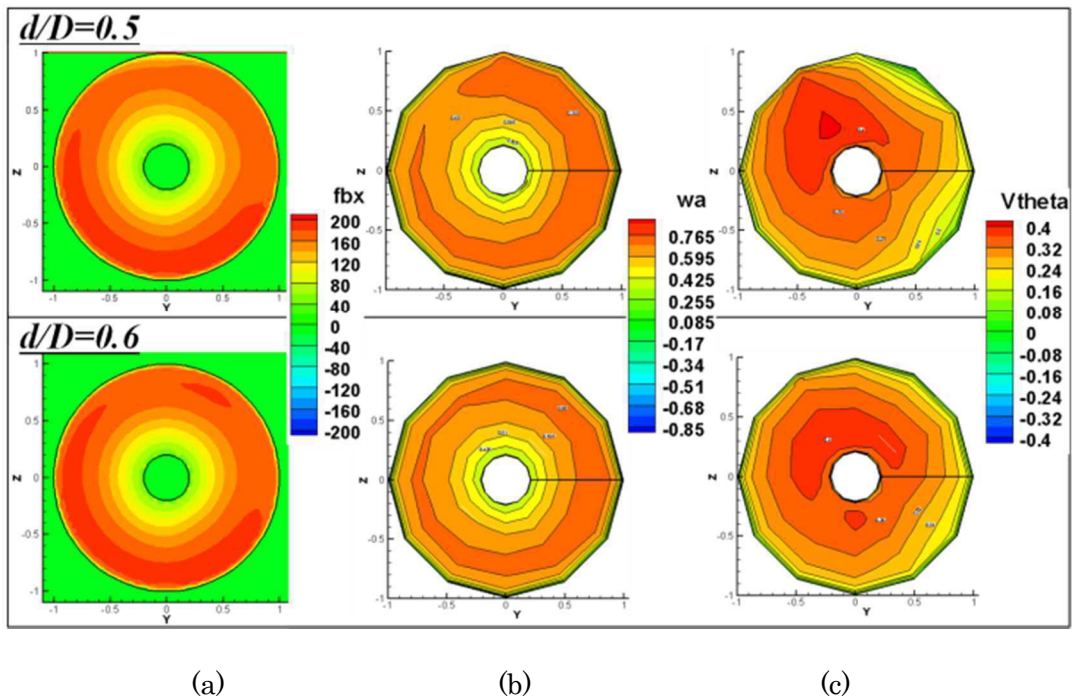
Fig. 2-19 Axial body-force distributions and induced velocity contours (J=0.5).

Open water characteristics results are summarized in Table 2-3 for solid-surface cases with two different propeller loadings. The thrust and torque coefficients decrease for lessened solid-surface level and the reduction is more obvious for higher loadings (J=0.5). When the solid-surface level is at the propeller tip, even for low loading case the reduction of the propeller performance is distinctive.

Table 2-3 Comparison of the open water characteristics of the solid-surface cases.

Case	n	J	T	Q	K_t	$10K_q$	η
$d/D=2$	0.55	0.9091	0.53669	0.22648	0.11089	0.23397	0.68572
$d/D=0.6$	0.55	0.9091	0.52304	0.22247	**0.10807**	**0.22982**	**0.68034**
$d/D=0.5$	0.55	0.9091	0.50766	0.21795	**0.10489**	**0.22515**	**0.67402**
$d/D=2$	1	0.5	4.69889	1.44288	0.29368	0.4509	0.5183
$d/D=0.6$	1	0.5	4.62307	1.42968	**0.28894**	**0.44677**	**0.51465**
$d/D=0.5$	1	0.5	4.53259	1.41225	**0.28329**	**0.44133**	**0.5108**

2.4 COMPARISON WITH THE EXPERIMENTAL DATA

The proposed method was implemented to predict the performance of the Modified-AU type fixed-pitch propeller. The propeller performance coefficients; thrust coefficient, torque coefficient and open water propeller efficiency in sequence, are calculated as;

$$K_t = \frac{T}{\rho\, n_d{}^2 D^4}, K_q = \frac{Q}{\rho\, n_d{}^2 D^5}, \eta = \frac{J}{2\pi}\frac{K_t}{K_q} \tag{23}$$

Figure 2-20 presents the results of the open water characteristics of the proposed model. The dashed lines demonstrate the body-force model results. The accuracy of the predicted open water characteristics of the proposed model depends on the advance

coefficient value. For instance, the thrust and the torque coefficients are underestimated for low advance coefficient values. A good agreement is seen for the thrust values, while large deviations occur for the predicted torque values. A possible reason for this disruption can be the constant sectional drag coefficient value used within the BET, which has a larger influence on the torque than on the thrust. The 2D lift and drag coefficients C_L and C_D depend on the angle of attack and can be found experimentally or numerically for a 2D aero foil. Moreover, the effect of the propeller blade Reynolds number can be introduced by choosing the proper lift and drag coefficients. These values can be tuned for specific propeller operating conditions if it is required.
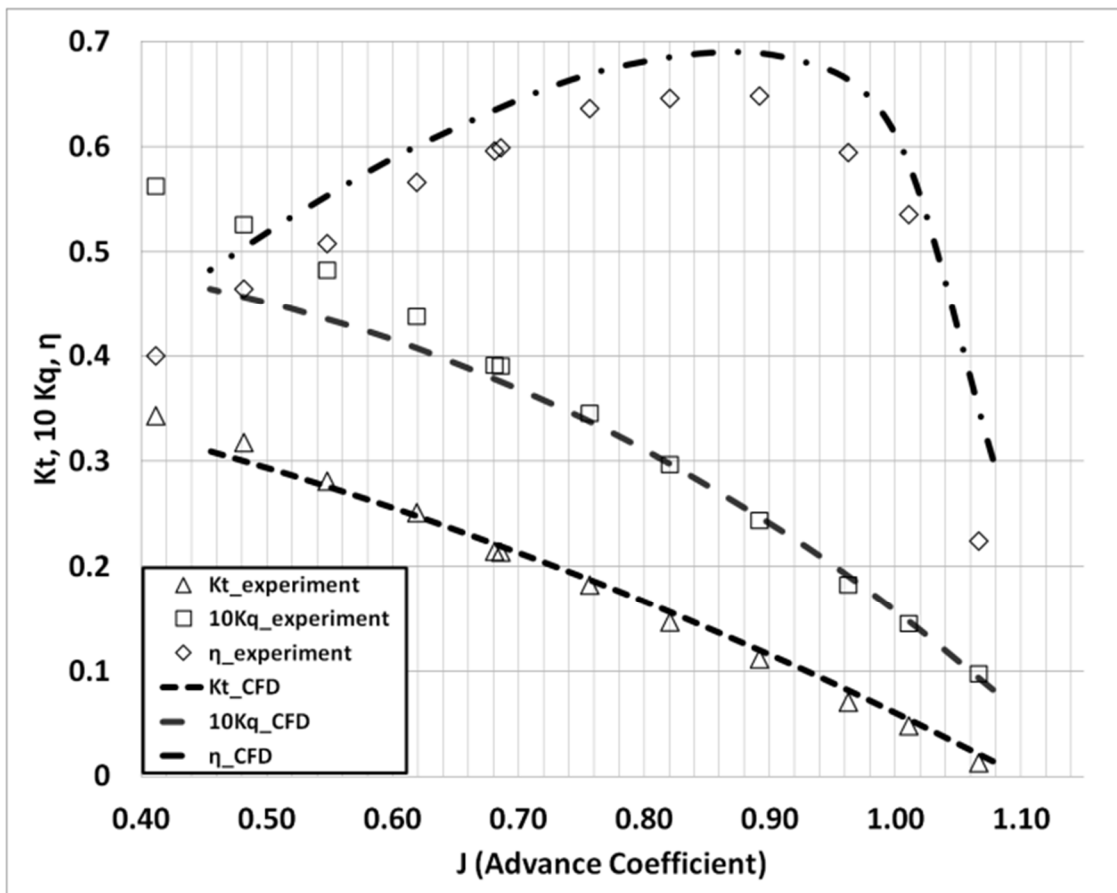
Fig. 2-20 Open water characteristics.

CHAPTER 3: APPLICATION OF THE BODY-FORCE MODEL TO THE FREE SURFACE EFFECT

In this chapter, the effect of free surface on the flow around a rotating propeller is studied by varying the propeller immersion depth to investigate the applicability of the new body-force method. A simplified quasi-steady BET with the infinite-bladed propeller model is coupled with the RANS code CFDSHIP-IOWA to calculate the flow around the propeller near the free surface. Propeller open-water characteristics are simulated in still water for different immersion depths for the Methodical-AU type fixed-pitch propeller. The propeller open characteristics are compared with the experimental data.

3.1 INTRODUCTION

Many researches of the flow field around a rotating propeller attached to a ship have been done using different numerical approaches without the free surface effect (Simonsen and Stern, 2005). However, the propulsive performance is affected by the presence of the free surface and the hull wake in reality. The free surface effect should be included in the inflow and wake. Thus in this chapter, the effect of free surface on the flow around a rotating propeller and the open water characteristics are studied by varying the propeller immersion depth to investigate the applicability of the body-force concept although the unsteady and free surface elevation effect around the blade are considered to be important. Herein, the propeller is represented by body-force field without the requirement of modeling the real propeller geometry. A simplified quasi-

steady BET with the infinite-bladed propeller model (time averaged propeller induced velocity field) is coupled with the RANS code CFDSHIP-IOWA to determine the body-force field. Finally, the numerical results of the open water characteristics of MAU type propeller are compared with the experimental data for validation.

3.2 COMPUTATIONAL METHOD

3.2.1 Grid Generation

Open water experiments with a five bladed 15 cm diameter propeller are carried out in still water for varying propeller immersion to investigate the propeller characteristics at racing condition in waves (Naito and Nakamura, 1979). Herein, for studying the effect of propeller immersion on the open water characteristics, four numerical grids were generated regarding the experiment cases; for immersion depth ratios of I/R=1.53, 1.2, 1 and 0.5, where I is the immersion depth (as shown in Fig. 3-1) and R is the propeller radius. The computational grid and the coordinate system used for the computations at I/R=1.53 are illustrated in Fig. 3-1. The grid generation method is the same as explained in Subsection 2.2.1. The grid was generated primarily with consideration of the propeller location, propeller immersion depth and the propeller wake. The propeller is located at the origin (x/R=0). Equal grid spacing covering the propeller boundary, was used on the yz plane as shown in Fig. 3-1 (left). For the rest, geometric progression was used. The minimum grid spacing Δx is taken as $0.01R$. The other three grids were just regenerated in z direction depending on the immersion depths of the propeller. Around the free surface which is at $z/R=0$, the grid is finest to capture the free surface elevation and

study the flow field in detail. Above the free surface, the grid is generated with a $0.5R$ depth for all cases. The computational domains for all cases which are non-dimensionalized by propeller radius R, represented in Table 3-1.
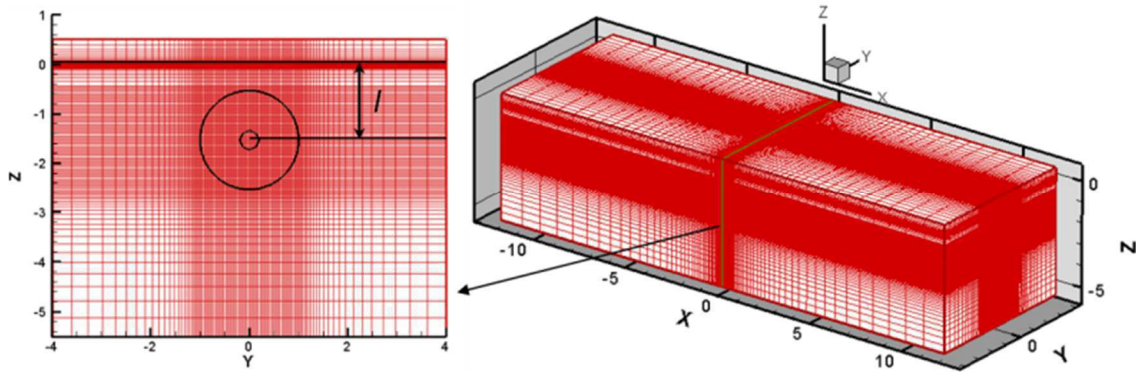
Fig. 3-1 Detailed grid representation on the propeller plane (Left)
Computational grid and coordinate system (Right).

Table 3-1 Computational domain and grid points.

Case	l/R=1.53	l/R=1.2	l/R=1.0	l/R=0.5
Grid points (ξ^1 x ξ^2 x ξ^3)	101x111x131	101x111x131	101x111x131	101x111x136
computational domain length	24 (-12 — 12)	24 (-12 — 12)	24 (-12 — 12)	24 (-12 — 12)
computational domain width	8 (-4 — 4)	8 (-4 — 4)	8 (-4 — 4)	8 (-4 — 4)
computational domain depth	6 (-5.5 — 0.5)	5.2 (-5.1 — 0.5)	5.5 (-5 — 0.5)	5 (-4.5 — 0.5)

The whole grid domain with boundary conditions is shown in Fig. 3-2. For the inlet boundary condition, velocity field is specified, pressure is zero gradient, and the turbulence is set to the free stream values. For the outlet boundary condition, streamwise viscous effects are taken zero. For side boundaries, zero gradient condition

is implemented. For the top boundary, far-field boundary condition is used by specifying the velocity field and zero gradient of the pressure and turbulence variables. For the bottom boundary, far-field boundary condition is used by specifying the axial velocity component and pressure to zero while all other variables are zero gradient. A single phase level set method is employed to model the free surface, which is located at *z/R*=0.
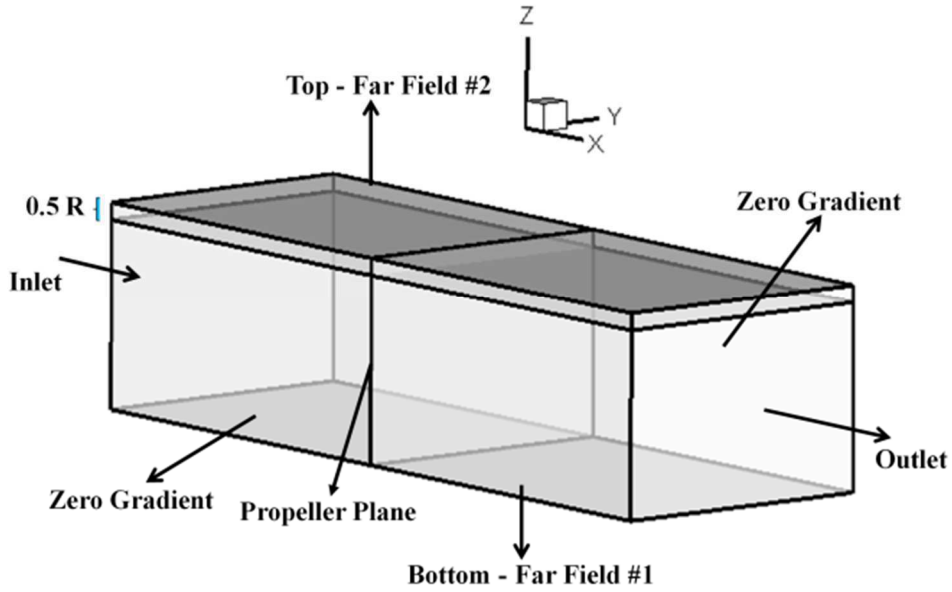
Fig. 3-2 Grid domain with boundary conditions.

3.2.2 Computational Outline

All the computations are carried out using RANS solver CFDSHIP-IOWA. It solves the continuity equation (Eq. (18) in Subsection 2.2.2) and unsteady incompressible RANS equation shown as in non-dimensional form and Cartesian tensor notation;

$$\frac{\partial u_i}{\partial t} + u_j \frac{\partial u_i}{\partial x_j} = -\frac{\partial \hat{p}}{\partial x_i} + \frac{1}{Re} \frac{\partial^2 u_i}{\partial x_j \partial x_j} - \frac{\partial}{\partial x_j}(\overline{u_i u_j}) + F b_i \tag{24}$$

where *x* is positive in axial direction, *y* is in starboard direction and *z* is in upper direction, respectively. $\hat{p}$ is the piezometric pressure $\hat{p} = p + \frac{1}{Fr^2} z$, $\overline{u_i u_j}$ are the Reynolds

stresses, v is the kinematic viscosity and $Re = {U_0 R}/{v}$ is the Reynolds number. The Reynolds stresses are related to the mean rate of strain through an isotropic eddy viscosity v_t as shown in Eq. (25) below, where δ_{ij} is the Kronecker delta and k_t is the turbulent kinetic energy. All the variables and properties are non-dimensionalized by R, free stream velocity U_0, the water density ρ and their combinations.

$$-\overline{u_i u_j} = v_t \left(\frac{\partial u_i}{\partial x_j} + \frac{\partial u_j}{\partial x_i} \right) - \frac{2}{3} \delta_{ij} k_t \tag{25}$$

For the time discretization, second-order Euler backward difference is used, the convective terms are discretized by second-order upwind method and the viscous terms in momentum and turbulence equations are discretized by second-order central difference scheme. For the velocity-pressure coupling the projection method is used (Paterson, Wilson and Stern, 2003).

The MAU type propeller used in the experiments has diameter (D) of 0.15 m, constant pitch (pitch ratio of 1.007), blade thickness ratio of 0.0530, expanded blade area ratio 0.6935 and the boss ratio of 0.1848. Within the computations, the values are non-dimensionalized by R. The flow parameters Re and $Fr = {U_0}/{\sqrt{gR}}$ (Froude number) are determined according to the number of revolutions of the propeller (n_d) and the advance coefficient ($J = {U_0}/{n_d D}$). To compare with the experimental data, the number of revolutions of the propeller (n_d) is taken as 10 rps. The non-dimensionalized number of revolutions which is $n = {n_d R}/{U_0}$, used in the computations. Kinematic viscosity of water is assumed to be 10^{-6} m²/s and acceleration of gravity (g) is taken as 9.81m/s². The computations are done for J=0.2 to J=1.0 for various immersion depths. The time increment is taken as Δt =0.01.

In the previous chapter, a polar coordinate system was used for the body-force

calculations and the interpolation for the velocity and body-force terms were required in this process. In the current chapter, the body-force calculations are directly carried out on the Cartesian coordinate system. The same computations, which are explained in Chapter 2, were also carried out by Yokota et al. (2013) using a Cartesian grid for the body-force calculations. Numerical results showed good agreement with the experimental data and the computational results presented in Chapter 2 (Yokota et al., 2013). For the thrust and torque calculations, the same mathematical formulations are utilized as written in Section 2.1 with some modifications. On each grid point within the propeller diameter, the following equations are solved to obtain the time-averaged body-force field at the propeller plane;

$$C_D = 0.009 + 0.202 \left| C_{L0.7r} - C_{Lopt0.7r} \right|^{2.5},$$

$$C_{Lopt0.7r} = \begin{cases} 1.690 \sqrt{\dfrac{t(r)}{c(r)} - 0.04} - 0.1, & \dfrac{t(r)}{c(r)} \ge 0.04 \\ -0.1, & \dfrac{t(r)}{c(r)} < 0.04 \end{cases} \tag{26}$$

where $t(r)$ is the maximum blade thickness.

$$dL = 0.5 C_L U_r^2 c(r), \quad dD = 0.5 C_D U_r^2 c(r), \tag{27}$$

where C_L is expressed by Eq. (3) and U_r is expressed by Eq. (1).

$$Fb_x = \frac{dT}{\Delta x} \frac{N}{2\pi r}, \quad Fb_y = \frac{dQ}{\Delta x} \frac{N}{2\pi r^2} sin\theta, \quad Fb_z = -\frac{dQ}{\Delta x} \frac{N}{2\pi r^2} cos\theta \ , \tag{28}$$

where $in\theta = \frac{z}{\sqrt{y^2+z^2}}$, $cos\theta = \frac{y}{\sqrt{y^2+z^2}}$ and dT, dQ are obtained from Eq. (8), (9), respectively.

The two dimensional lift coefficient (Eq. 3) is used and the effect of blade to blade interaction is included as a correction factor k_1, which is obtained by Eq. (4). The effective pitch (H_e) is taken as 1.1 times of the geometric pitch of the propeller (H). The chord, pitch and thickness distribution of the propeller are utilized in the computations.

However, the effect of rake and skew distribution are not considered in this chapter.

The graphs representing the chord length and thickness distribution are shown in Fig. 3-3. Since the propeller is divided into 50 radial sections for calculating the loading of the propeller, chord and thickness distribution is interpolated. The thickness distribution of the propeller is needed to calculate the two dimensional drag coefficient as indicated in Eq. (26) for AU, MAU type propellers (Moriyama, 2013). The time averaged body-forces acting in x, y and z directions on the propeller plane are calculated by Eq. (28) using the time averaged local pressure jump and the thrust (Eq. (8)) and torque (Eq. (9)) acting on the representative blade element. Finally, the body-force terms are added in the momentum equations shown by Eq. (24). The total thrust and torque exerted by the propeller can be obtained by integrating the time averaged pressure differences acting in axial and tangential direction over the propeller radius as shown by Eq. (29).

$$T = \iint dP_x dy dz, \ Q = \iint dP_\theta r dy dz \tag{29}$$
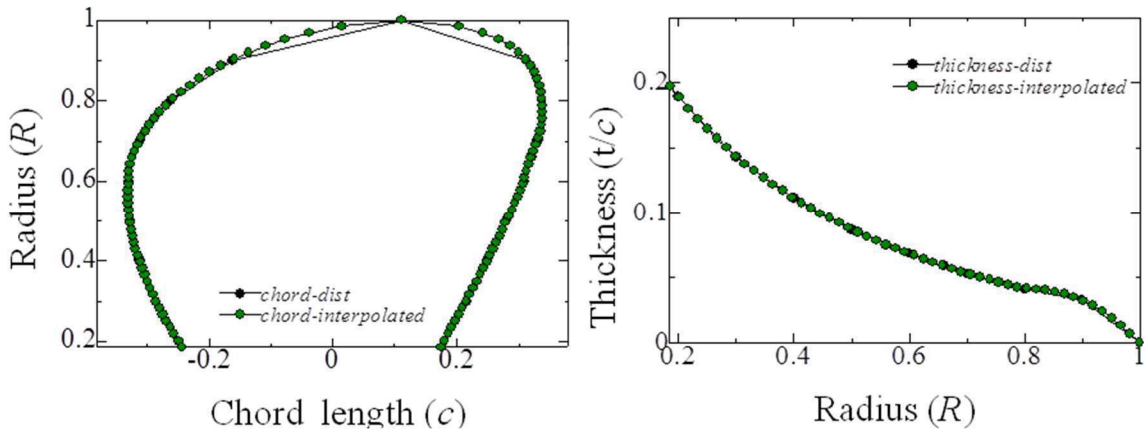
Fig. 3-3 The chord length and thickness distribution of the propeller.

3.3 RESULTS

3.3.1 Propeller Inflow and Propeller Plane

The axial-velocity contours of the close upstream and downstream of the propeller on *xz* plane are shown in Fig. 3-4. The air above the free surface is blanked in the figure. As it is seen in the upstream region the axial-velocity increases in a similar manner for both cases while the inflow advances to the propeller plane. However, when the immersion depth is smaller (Right) at this advance coefficient, propeller goes out of the water. Therefore, the axial-velocity becomes relatively low in the downstream on the upper half of the propeller. As a result, propeller performance characteristics reduce.
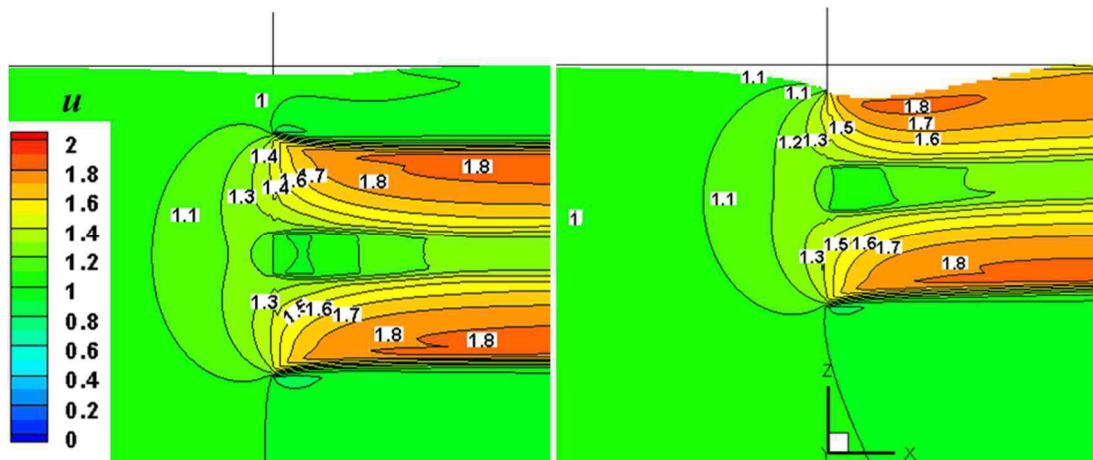
Fig. 3-4 Axial-velocity contours of upstream and downstream of the propeller
at J=0.6 (Left) *I/R*=1.53 (Right) *I/R*=1.0.

To check the inflow velocity changes and its effect to the slipstream in detail, the axial-velocity profiles at various upstream sections are plotted. In Fig. 3-5, it is observed that the axial-velocity magnitude are very similar for *I/R*=1.53 (a) and *I/R*=1.2 (b). However the velocity starts dropping while getting close to the propeller plane as seen in the case

for *I/R*=1.0 (c). Figure 3-5 shows that the axial-velocity magnitude in the upstream for deeper cases are higher than the shallower case *I/R*=0.5 (d). The maximum axial-velocity magnitude is remarkably reduced for *I/R*=0.5. Also the axial-velocity profile changes and the distribution of the axial-velocity become narrower than the deeper cases. As it can be noticed, the axial-velocity distribution difference becomes distinctive while approaching to the propeller plane. This graph indicates that the inflow velocity is remarkably affected by the free surface. This low inflow velocity profile for shallower case decreases the axial-momentum in the slipstream.

Fig. 3-5 Variation of axial-velocity profiles at several upstream locations at J=0.6 at *y/R*=0: (a) *I/R*=1.53 (b) *I/R*=1.2 (c) *I/R*=1.0 (d) *I/R*=0.5.

The axial-velocity contours and vectors on the propeller plane are displayed in Fig.3-6 for different immersion depths at J=0.4. When the propeller immersion ratio decreases the axial-velocity distributions become asymmetrical due to the free surface deformation. The suction force is not the same laterally. As it is seen, the axial-velocity increases on the port side for I/R=1.0 and I/R=0.5. By looking at Fig. 3-7, it can be said that the axial body-force distributions correlate with the axial-velocity contours. The axial body-force increases on the port side when the immersion depth decreases.
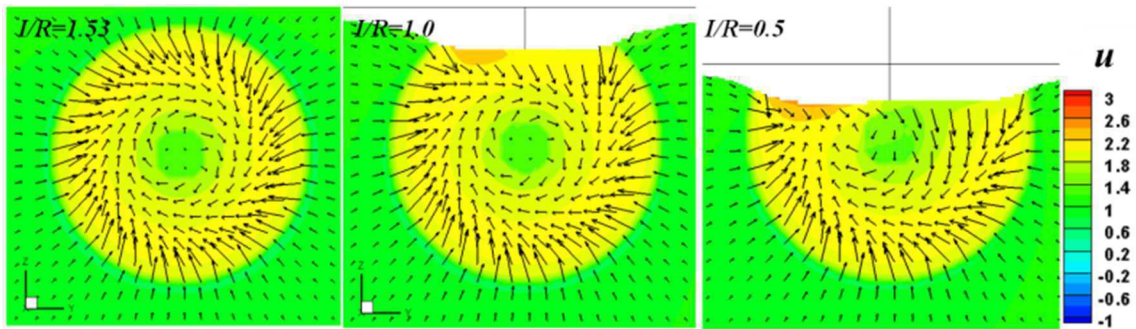
Fig. 3-6 Axial-velocity contours and vectors on the propeller plane at J=0.4.
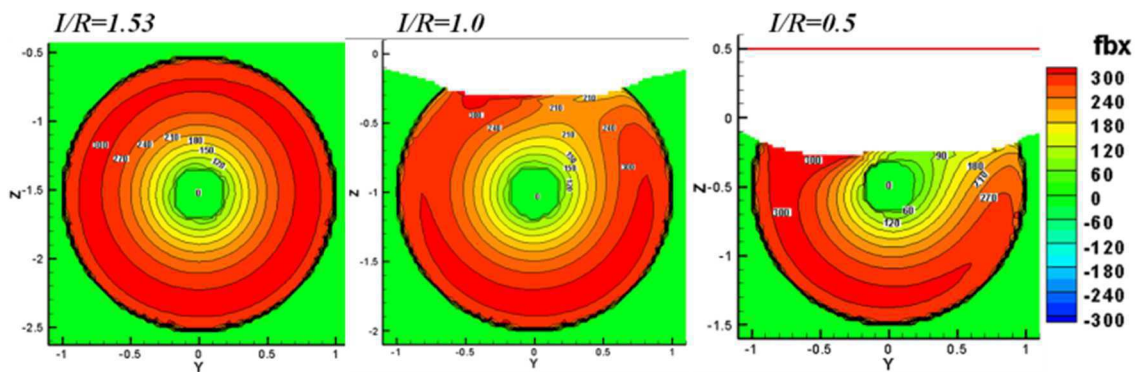
Fig. 3-7 Axial body-force distributions on the propeller plane at J=0.4.

Figure 3-8 shows the axial-velocity change in the upstream region (at x/R=-0.8) for three different loadings at different immersion depths. The inflow velocity increases and the distribution of the axial-velocity changes with the increased propeller loading. Also, while the immersion depth decreases the axial-velocity reduces and this reduction becomes significant as the propeller loading increases. For I/R=1.53 (a) and I/R=1.0 (b), there is no significant change in the axial-velocity. In conclusion, it is shown that the velocity in the upstream region of the propeller is affected by the propeller loading and the immersion depth of the propeller.
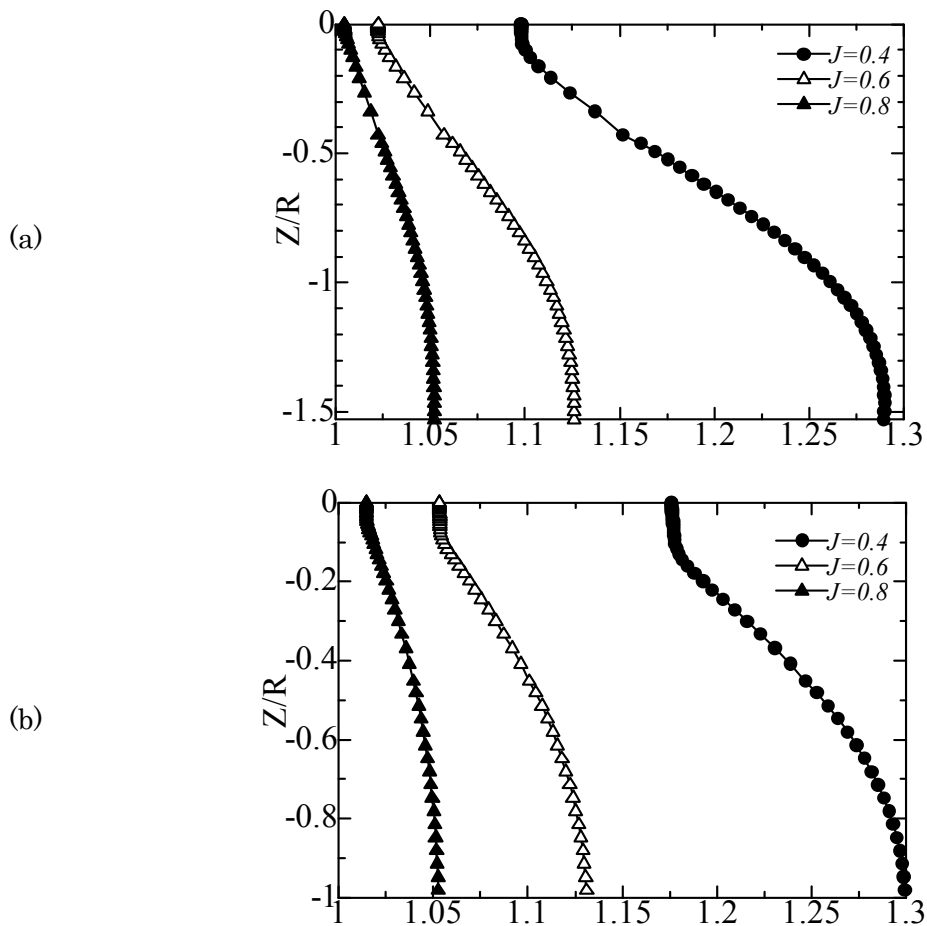
(a)

(b)

Fig. 3-8 Variation of axial-velocity profiles at different loadings at x/R=-0.8, y/R=0: (a) I/R=1.53, (b) I/R=1.0, (c) I/R=0.5.

(c)
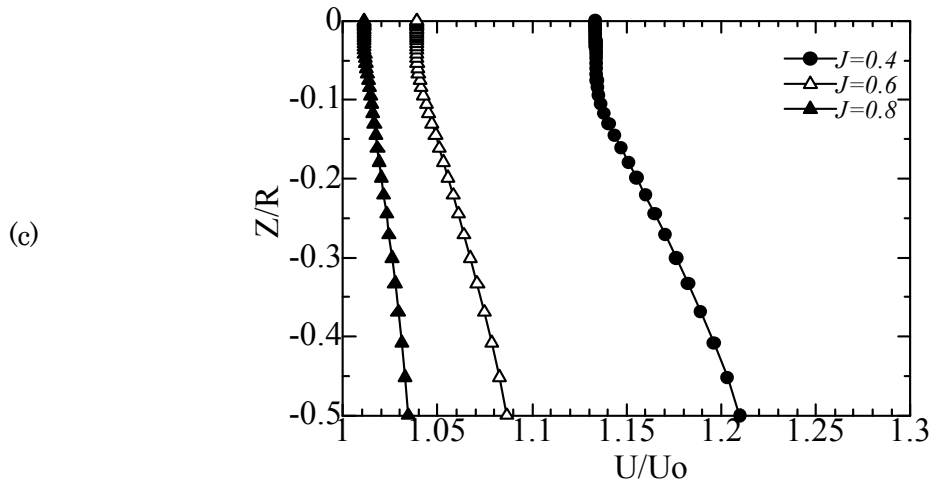
Fig. 3-8 Variation of axial-velocity profiles at different loadings at *x/R*=-0.8,
y/R=0: (a) *I/R*=1.53, (b) *I/R*=1.0, (c) *I/R*=0.5.

3.3.2 Propeller Wake

Figure 3-9 shows the axial-velocity profiles at various downstream locations for different immersion depths at J=0.6. For the immersion depth ratios *I/R*=1.53 (a) and *I/R*=1.2 (b), the velocity magnitude and distribution are very close, but for *I/R*=1.0 (c) the distribution of the axial-velocity changes. As it is seen in Fig. 3-9 (d) the velocity magnitude in the downstream is lower for shallower case. Therefore, thrust is expected to be lower for this case. Moreover, the axial-velocity distributions are different for both cases in the upstream and downstream of the propeller plane.
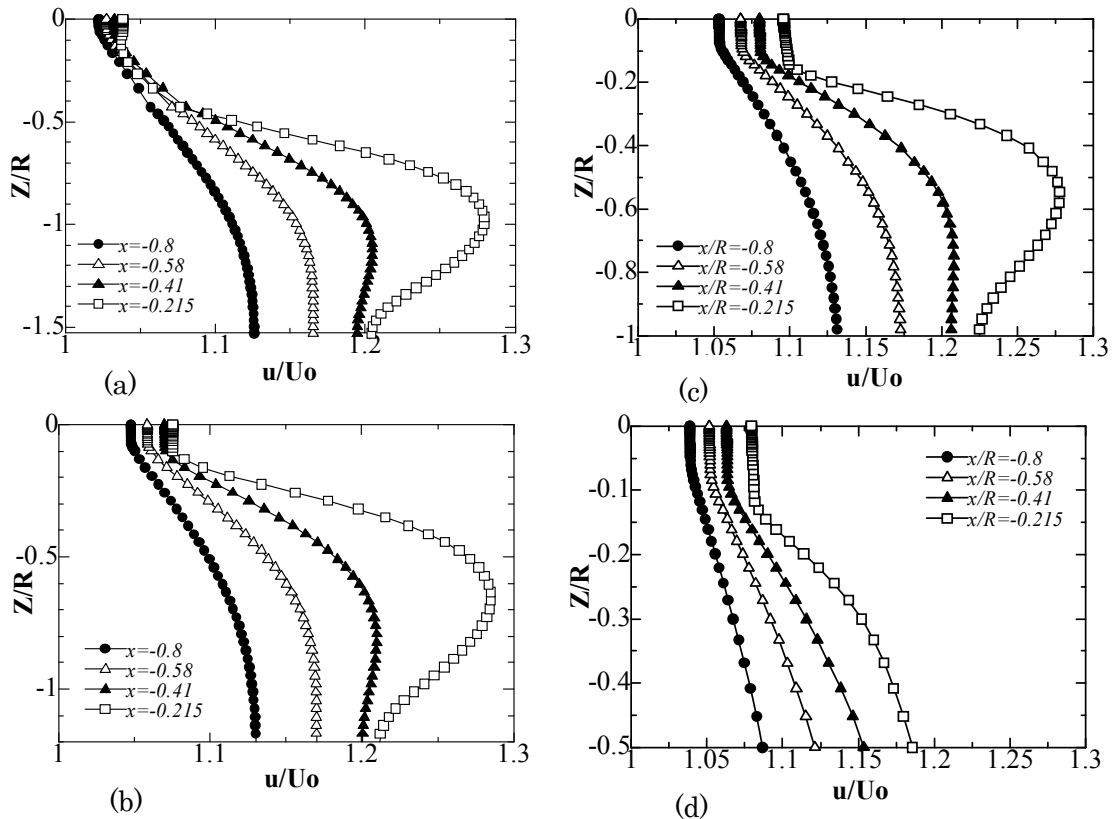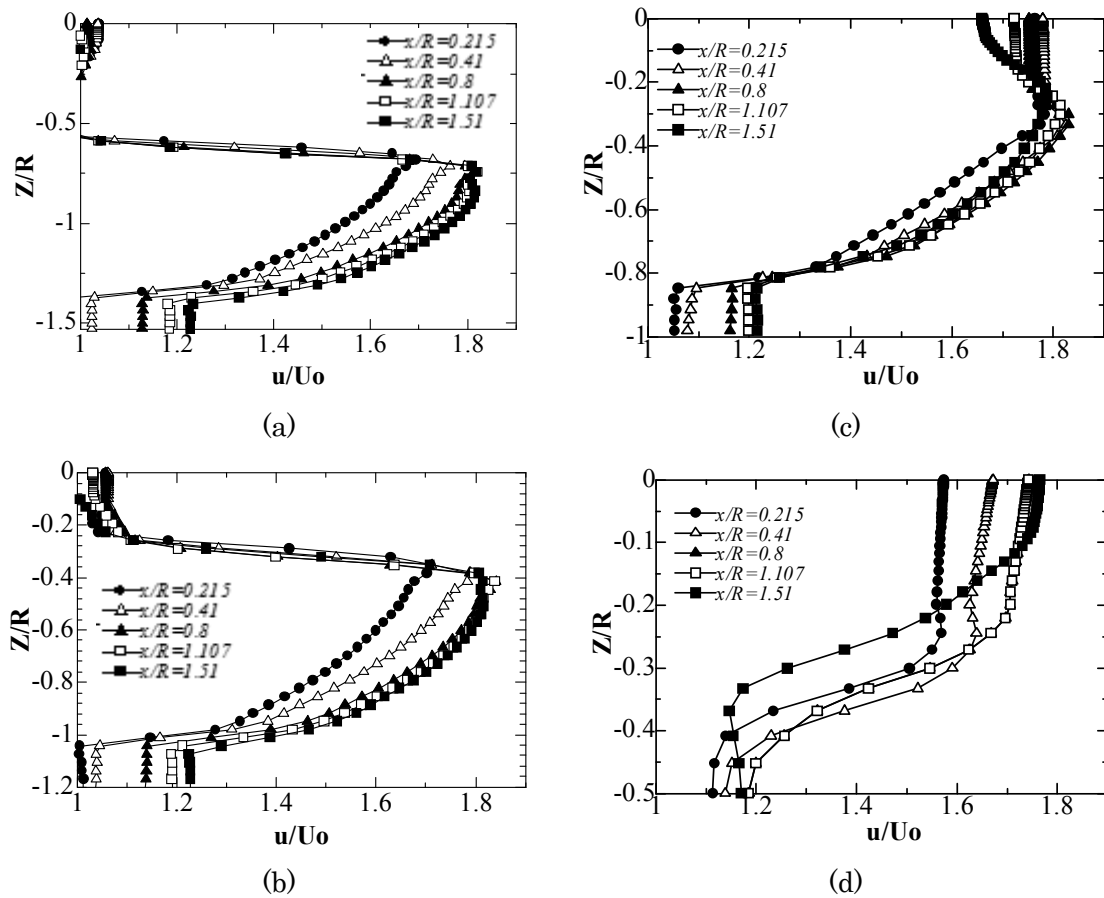
Fig. 3-9 Variation of axial-velocity profiles at several downstream locations at J=0.6 at
y/R=0: (a) *I/R*=1.53 (b) *I/R*=1.2 (c) *I/R*=1.0 (d) *I/R*=0.5.

As the propeller gets closer to the free surface the deformation of the free surface

becomes significant as seen in Fig. 3-10 which shows the elevation of surface level at

J=0.4 for different immersion depths. In Fig. 3-11 the elevation of surface level at

different immersion depth at J=0.4 is plotted along the *x* axis. The propeller rotation

deforms the free surface around the propeller plane and after the propeller plane the

surface level rises. As the immersion depth decreases the disturbance of the free surface

becomes more significant. When the number of revolution of the propeller increases the

free-surface deforms distinctively as seen in Fig. 3-12. According to the following graphs,

free surface deformation is affected by the propeller loading and the immersion depth.
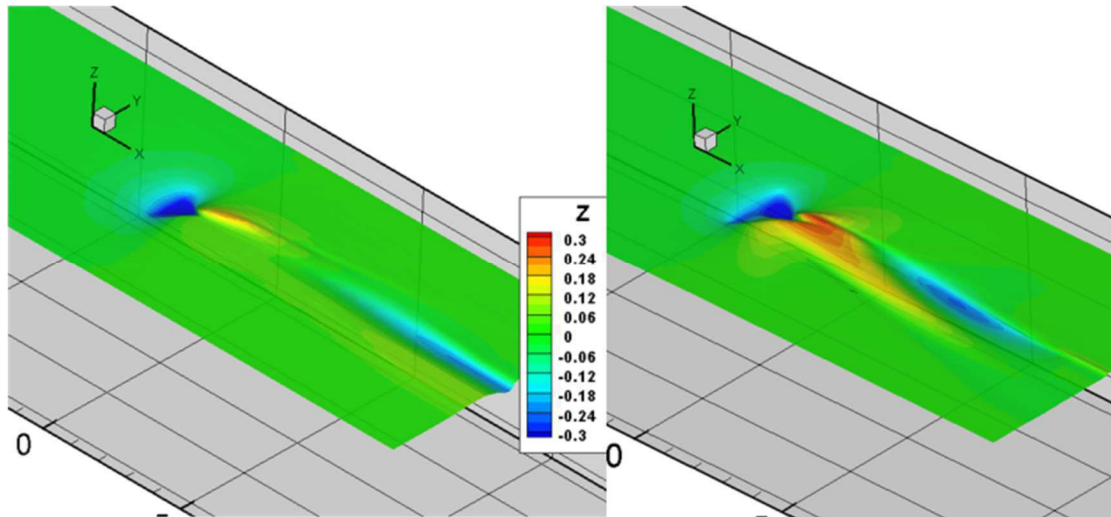
Fig. 3-10 Elevation of surface level at J=0.4 Left (*I/R*=1.0) Right (*I/R*=0.5).
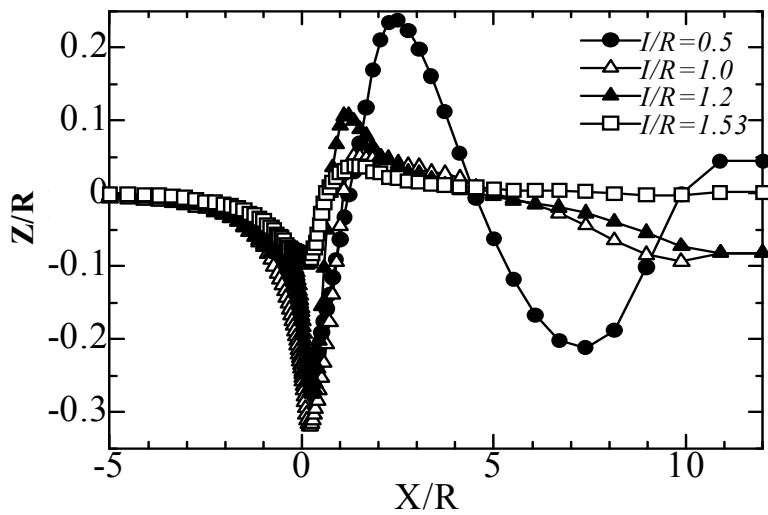
Fig. 3-11 Elevation of free surface level (*z/R*) at *y/R*=0 for different immersion depths at

J=0.4.
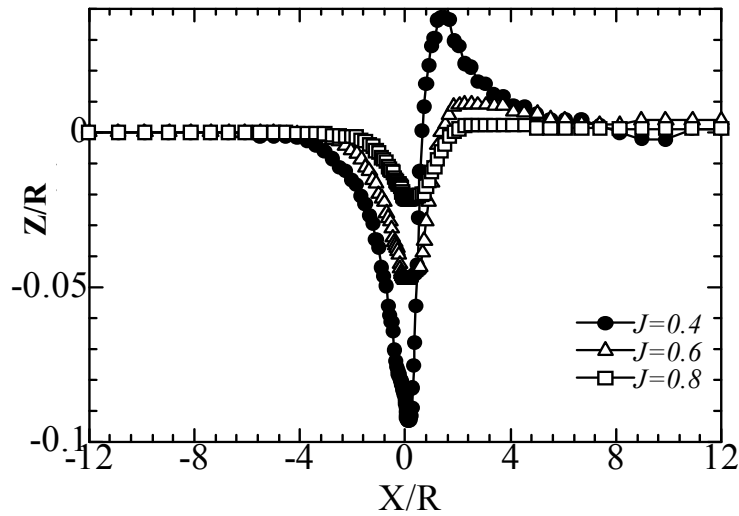
Fig. 3-12 Elevation of free surface level (z/R) at y/R=0 for I/R=1.53
at three different loadings.

3.4 COMPARISON WITH THE EXPERIMENTAL DATA

The body-force model was implemented with the effect of the free surface to predict the performance of the MAU type fixed-pitch propeller. The computational results are compared with the experimental data to validate the applicability of the proposed method (Naito and Nakamura, 1979).

Figure 3-13 presents the results of the open water characteristics of the proposed model at different immersion depths. The dashed lines demonstrate the body-force model results, the symbols represent the experimental data and the solid black line is the experimental data for I/R=1.53. The accuracy of the predicted open water characteristics of the proposed model depends on the advance coefficient value. For instance, the thrust and the torque coefficients are overestimated for low advance coefficient values. A good agreement is seen for I/R=0.5, while large deviations occur at high loadings for I/R=1.2 and I/R=1.0. According to the experimental results the thrust and torque values reduces
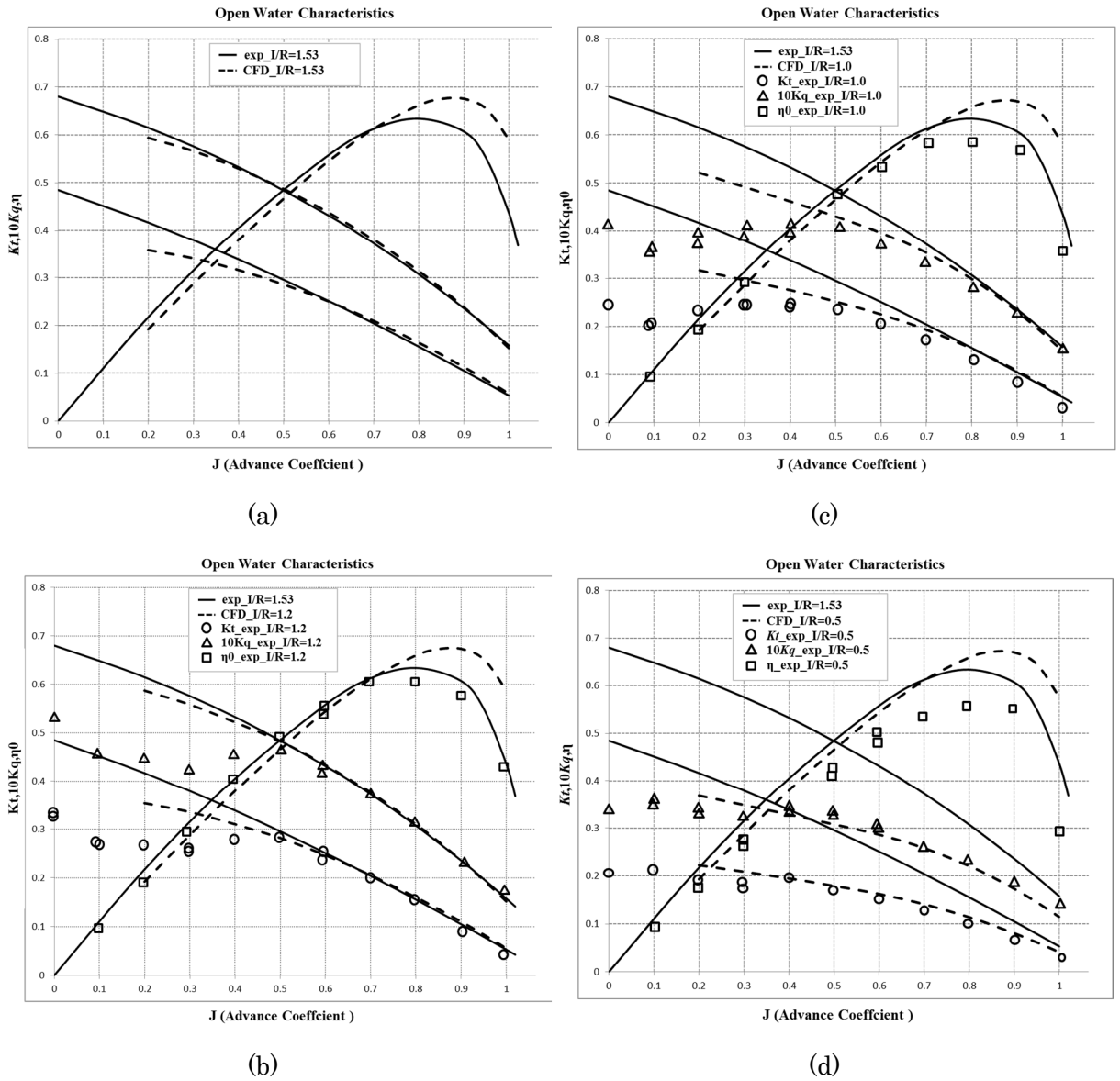
Fig. 3-13 The comparison between the computations and the experimental data for: (a) *I/R*=1.53 (b) *I/R*=1.2 (c) *I/R*=1.0 (d) *I/R*=0.5.

rapidly for high loadings on the contrary of the deeper case (*I/R*=1.53). Even though the

performance coefficients are lower than the deeper case for low advance coefficient

values, our time-averaged body-force model could not capture well this rapid reduction

of the thrust and torque coefficients. The proposed time-averaged body-force model could

not explain the non-linear phenomenon of the flow at the high propeller loadings. However, for design conditions the propeller performance can be predicted well.
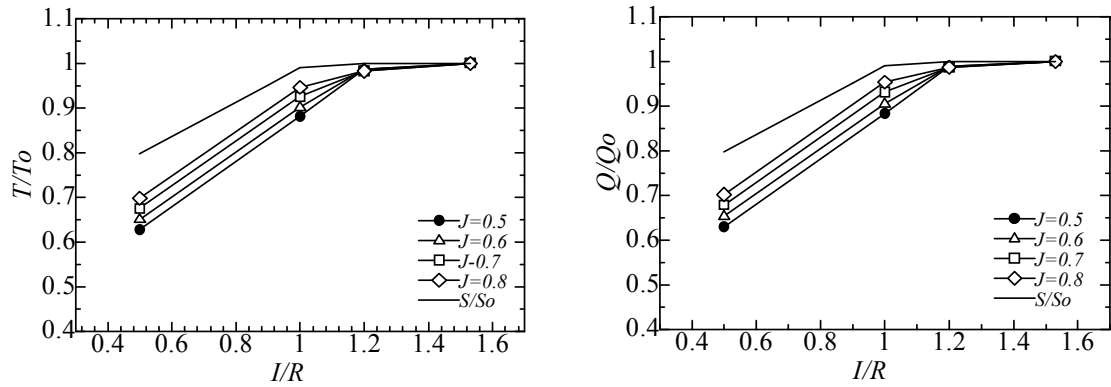
(a)
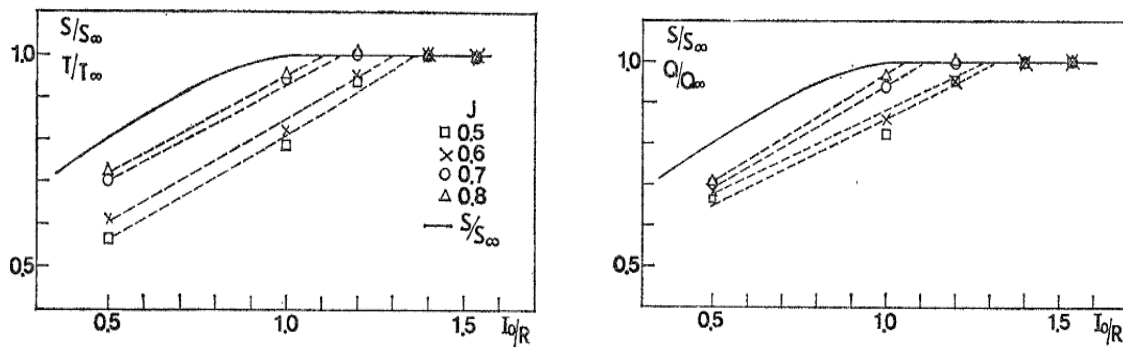
(b)

Fig. 3-14 Relation between propeller immersion and ratio of propeller load at shallow immersion to that at deep one (a) CFD (b) Experiment by Naito and Nakamura (1979).

For light loadings, there is no significant difference between the cases in the propeller performance characteristics as seen in Fig. 3-13 (b & c). The performance results are slightly higher for I/R=1.53 compared to I/R=1.0 for light loadings. However, when the propeller immersion ratio is I/R=0.5, even for light loadings the propeller performance difference is distinctive. Figure 3-14 represents the relation of the propeller immersion

by comparing the ratio of the propeller load at shallow immersion to deep one for different advance coefficient values from CFD (a) and the experimental results (b). S_o (or S_∞ in Fig. 3-14 (b)) indicates the total propeller area and S indicates the wet propeller area. T_o (or T_∞ in Fig. 3-14 (b)) and Q_o (or Q_∞ in Fig. 3-14 (b)) represents the thrust and torque coefficients for deep case (I/R=1.53). As it is seen, the difference between the thrust and torque values becomes significant when J becomes smaller (number of revolution of the propeller gets higher) and also when the immersion depth decreases. Both graphs (a & b) show the same tendency for thrust and torque coefficients.

CHAPTER 4: COMPUTATION OF THE PROPELLER-HULL INTERACTION FOR DIFFRACTION PROBLEM

In this chapter, the diffraction problem with forward speed is discussed numerically because of its importance to predict the ship motions in wave fields. The body-force propeller model, which is presented in Chapter 2, with a simplified quasi-steady BET coupled with the RANS code CFDSHIP-IOWA to study the forward speed diffraction problem of the tanker KVLCC2 in fully-loaded condition. Herein, the propeller boss effect is also included. The simulations are done for the ship advancing at design Froude number Fr=0.142 under regular head waves with the same wave amplitude (A=0.009375L, where L is the ship length) and three different wavelengths (λ/L=0.6, 1.1 and 1.6). The computations are also carried out without propeller for the same cases to analyze the propeller effect on the flow field wake fields in waves.

4.1 INTRODUCTION

A new body-force model has been proposed in Chapter 2 and simulations around the KVLCC2 tanker model were carried out for the propeller-hull-rudder interaction in calm water by Win (2014). In this chapter, the ship forward speed diffraction problem (i.e. a ship advancing in regular head waves but restrained from motions) is discussed numerically because of the importance to analyze the propeller loads in wave fields. The tanker KVLCC2 is studied in fully-loaded condition. A simplified quasi-steady BET with the infinite-bladed propeller model is coupled with the RANS code CFDSHIP-IOWA. The

effect of the propeller in the flow field can be represented by momentum source terms in the form of a body-force propeller model and the propeller boss effect is included. Within this body-force model, the total velocity components are determined by CFD code. The induced velocity effect is included by time averaged infinite bladed vortex system shed by propeller blade. In this method, the body-force terms interact with the flow field solver and the forces & moments (6 components in total) are considered in the 6DOF solver. Since the calculation of the body-forces is achieved easily, the present objective is to reduce the significant computational cost when the effect of ship motions or waves is included.

4.2 COMPUTATIONAL METHOD

4.2.1 Test Conditions, Ship and Propeller Geometry

The computations are performed for KVLCC2 ship model with hub and propeller in fully-loaded condition. The main particulars of the model scale ship are summarized Table 4-1 and the propeller data are provided in Table 4-2 below. Figure 4-1 displays the KVLCC2 ship model body plan and hull form in fully loaded condition. In Fig. 4-2 (a), KVLCC2 anticlockwise and clockwise propeller models are displayed. The open water characteristics test results of the right-handed and left-handed propellers operating with 15 & 30 rps are provided by (Okawa, 2015). Within the numerical calculations, the propeller was not represented by its physical geometry, but the pitch and chord distributions of the propeller, which are non-dimensionalized by the ship length, were employed as plotted in Fig. 4-2 (b). The design speed of the ship model is 0.795 m/s,

service speed of the full scale ship is 15.5 knots, which corresponds to Froude number Fr=0.142. Reynolds number is Re=2.05×10^6. The simulations are carried for calm water and three different wave length cases. As a short wave length case λ/L=0.6 is chosen. The case λ/L=1.1 has the maximal added resistance (Sadat-Hosseini et al., 2013). The λ/L=1.6 is used to present long wave length. The wave amplitude A=0.03m which corresponds to A/L=0.009375 is used for all the simulations with consideration of the wave steepness h/λ≤1/30. For propeller settings, the number of revolution is taken as n_d=16.4 rps, corresponding to the advance coefficient J=0.492. It is suggested by experimental self-propulsion test in calm water.

Table 4-1 Main particulars of KVLCC2 ship model (OU 1/100 model).

		Fully-loaded cond.
Length between perpendiculars	L_{PP} (m)	3.200
Beam	B_{WL} (m)	0.580=B
Depth	D (m)	0.30
Draft	T (m)	0.208
Displacement	∇ (m^3)	0.313
Longitudinal center of buoyancy	LCB(%L_{PP}), fwd+	3.48
Vertical Center of Gravity (from keel)	KG (m)	0.186=KG$_D$
Radius of gyration	K_{XX} (m)	0.4B
	K_{YY} (m)	0.25Lpp
	K_{ZZ} (m)	0.25Lpp
Block coefficient	C_B	0.8098
Mid-ship section coefficient	C_M	0.9980
Water plane area coefficient	C_W	0.9000

Table 4-2 Main particulars of KVLCC2 propeller (1/100 scale model).

Propeller Type	FPP
No. of blades	4
Diameter (D(m))	0.0986
Hub ratio	0.155
Expanded Area ratio (A_e/A_0)	0.431
Skew degree	21.15
Rake degree	0.0
Rotation	Right hand
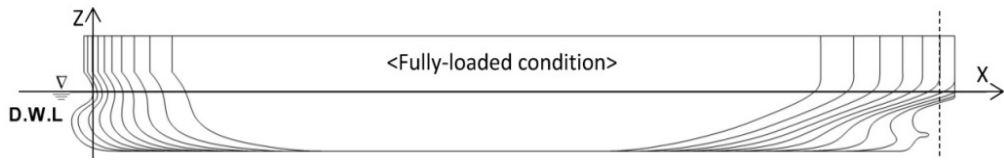
Side view
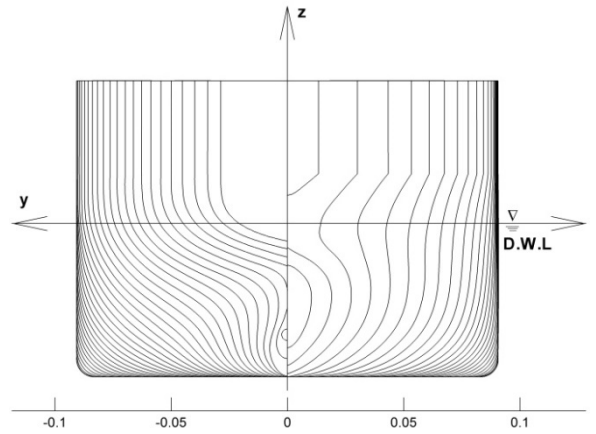
3-D view   Bow and stern view

Fig. 4-1 KVLCC2 body plan and hull from.

(a)

(b)
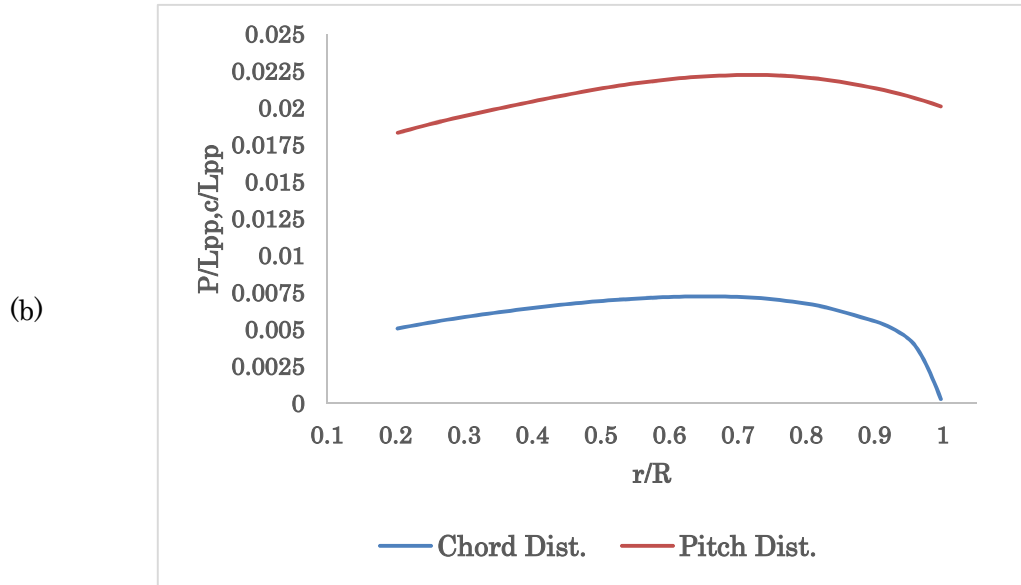
Fig. 4-2 (a) KVLCC2 propeller model (Left: anticlockwise, Right: clockwise).
(b) Chord and pitch distribution of the KVLCC2 propeller model.

4.2.2 CFD Method

The simulations are performed with RANS solver CFDSHIP-IOWA which is designed to simulate wide range of ship hydrodynamic problems. It uses multi-block structured grid with overset gridding capability to generate complex geometries and allows to do local refinement where needed. The overset interpolation information is determined by dynamic SUGGAR code, which is utilized for moving body problems and interaction with a motion controller like the 6DOF solver in CFDSHIP-IOWA (Carrica et al., 2007). High performance parallel computation is performed by a MPI-based domain decomposition approach, where each decomposed block is mapped to one processor. It also includes semi-captive, full 6DOF capabilities for multi objects with parent/child hierarchy, two-equation turbulence models, second-order finite-difference and PISO or projection

methods for pressure-velocity coupling. For the propulsion, the actual propeller, or interactive or prescribed body-force propeller model can be utilized. Herein, the body-force propeller model, which is mentioned in Chapter 2, is employed as an interactive propeller model.

In the simulations for current chapter, SST k-ω turbulence model with no wall function is used (Menter, 1994). A single phase level set method (Carrica, Wilson et al., 2007), which uses a signed distance function (also known as level-set function), is used to model the free surface. The level-set function is 'zero' value for the free-surface location, positive in water and negative in air. All the variables and properties are non-dimensionalized by ship length between perpendiculars L_{pp}, ship speed U_0, the water density ρ and their combinations.

The governing equations are discretized using higher-order finite-difference approach with body-fitted curvilinear grids. For the time discretization in the turbulence and momentum equations, second-order Euler backward difference is used, the convective terms are discretized by second-order upwind method and the viscous terms in momentum and turbulence equations are discretized by second-order central difference scheme. For the velocity-pressure coupling the projection method, a two-stage fractional step scheme, is used with the PETSc (Portable Extensible Toolkit for Scientific Computation) toolkit. PETSc is a parallel numerical software library for partial differential equations computations. Between three and five inner iterations are looped in each time step to solve the discretized governing equations system and solutions are considered to be converged when the error for velocities, pressure, and level-set reach to less than 10^{-5}, 10^{-8}, and 10^{-5} respectively (Sadat-Hosseini et al., 2013).

The 6DOF rigid body equations of motion are solved by the following equations:

$$m[\dot{u} - vr + wq] = X - T_x$$

$$m[\dot{v} - wp + ur] = Y - T_y$$

$$m[\dot{w} - uq + vp] = Z - T_z$$

$$I_x\dot{p} + \left(I_z - I_y\right)qr = K - Q_x \qquad (30)$$

$$I_y\dot{q} + (I_x - I_z)rp = M - Q_y$$

$$I_z\dot{r} + \left(I_y - I_x\right)pq = N - Q_z$$

Herein $u,\ v,\ w$ are surge, sway, heave velocities, $p,\ q,\ r$ are the roll, pitch, yaw angular velocities in the ship system and $I_x,\ I_y,\ I_z$ are moment of inertia around $x,\ y$ and z axis. The forces in $x,\ y,\ z$ axis directions in ship coordinate are $X,\ Y,\ Z$ and the moments are $K,\ M,\ N$, where $T_x,\ T_y,\ T_z$ are the forces and $Q_x,\ Q_y,\ Q_z$ are the moments transferred from the propeller coordinate system to ship coordinate system.

The computational domain with boundary conditions is shown in Fig. 4-3. The computational domain extends from $-0.5 < x/L < 2.35$, $-1 < y/L < 1$ and $-1 < z/L < 0.22$ in dimensionless coordinates based on ship length, where L=Lpp and $x,\ y,\ z$ are the Cartesian coordinates. The ship bow (FP) is located at $x/L = 0$ and the stern (AP) is located at $x/L = 1$. The y-axis is positive in starboard direction and the z-axis is positive in the upward direction. The undisturbed free surface is located at $z/L = 0$.

The boundary conditions used for the computations are listed in detail in Table 4-3. The far field boundary conditions are implemented for the top and bottom of the background domain. Zero gradient boundary condition is implemented for the sides of the background. For the inlet, wave boundary conditions calculated from the linear potential flow solution, are applied as (Weymouth et al., 2005):

$$\zeta(x,t) = A\cos(kx - \omega_e t), \qquad (31)$$

$$u(x,z,t) = \omega A e^{kz}\cos(kx - \omega_e t), \qquad (32)$$

$$w(x,z,t) = \omega A e^{kz} \sin(kx - \omega_e t),\qquad(33)$$

$$p(x,z,t) = \frac{\omega^2 A e^{kz}}{k}\cos(kx - \omega_e t) - \frac{\omega^2 A^2 e^{2kz}}{2},\qquad(34)$$

where ζ is the unsteady free surface elevation, $k=2\pi/\lambda$ is the wave number, ω is the wave circular frequency and ω_e is the encounter frequency.

Table 4-3 Boundary conditions.

Location	Type	u	v	w	p	k_t	ω_t
Inlet	Wave	Eq. (31)	0	Eq. (32)	Eq. (33)	0	0
Outlet	Exit	$\nabla^2 u=0$	$\nabla^2 v=0$	$\nabla^2 w=0$	$\nabla p=0$	$\nabla k_t=0$	$\nabla \omega_t=0$
Sides	Zero Gradient	$\nabla u=0$	$\nabla v=0$	$\nabla w=0$	$\nabla p=0$	$\nabla k_t=0$	$\nabla \omega_t=0$
Top	Far field #2	u_∞	v_∞	w_∞	$\nabla p=0$	$\nabla k_t=0$	$\nabla \omega_t=0$
Bottom	Far field #1	u_∞	$\nabla v=0$	$\nabla w=0$	0	$\nabla k_t=0$	$\nabla \omega_t=0$
Hull/stern	No-slip	0	0	0	$\nabla p=0$	0	$60/\mathrm{Re}\beta\Delta y^2$

The exit boundary condition is used for the outlet. No-slip boundary condition is applied for all the solid surfaces. Additionally, rotating boundary condition for the hub is imposed. The rotational effect is introduced into the RANS code as user defined boundary condition which is set on each grid point on the hub surface. This condition for a right handed propeller is shown as a schematic in Fig. 4-4 (a) for one axial section of the hub. The Reynolds-averaged velocity components on the hub surface (v and w) can be calculated by Eq. (35) and Eq. (36), where r_{hub} is the hub radius as shown in Fig 4-4 (a). The rotating velocity vectors (v and w) on the hub surface are illustrated in Fig 4-4 (b). The axial-velocity contours on the propeller plane and streamlines are drawn around hub and propeller as displayed in Fig. 4-4 (c) in $\lambda/L=0.6$. The swirling streamline around the hub surface can be observed from this figure.

$$v = 2\pi n r_{hub} \sin\theta\qquad(35)$$
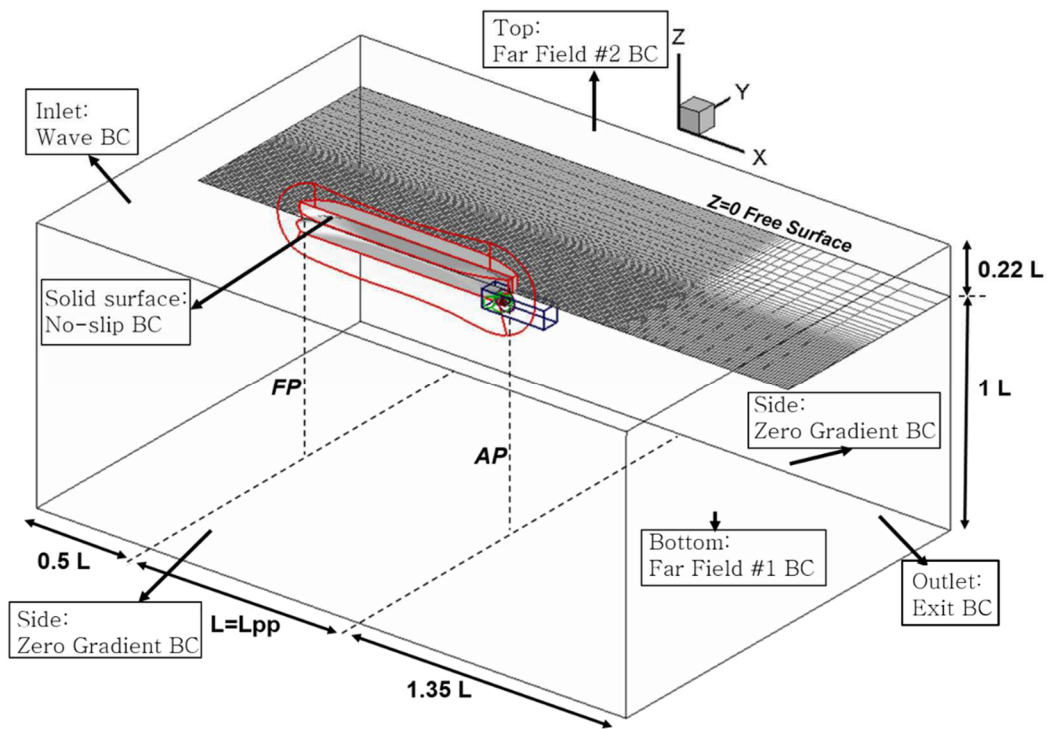
$$w = -2\pi n r_{hub} \cos\theta\qquad(36)$$

Fig. 4-3 Computational domain and boundary conditions.

(a)

(b)
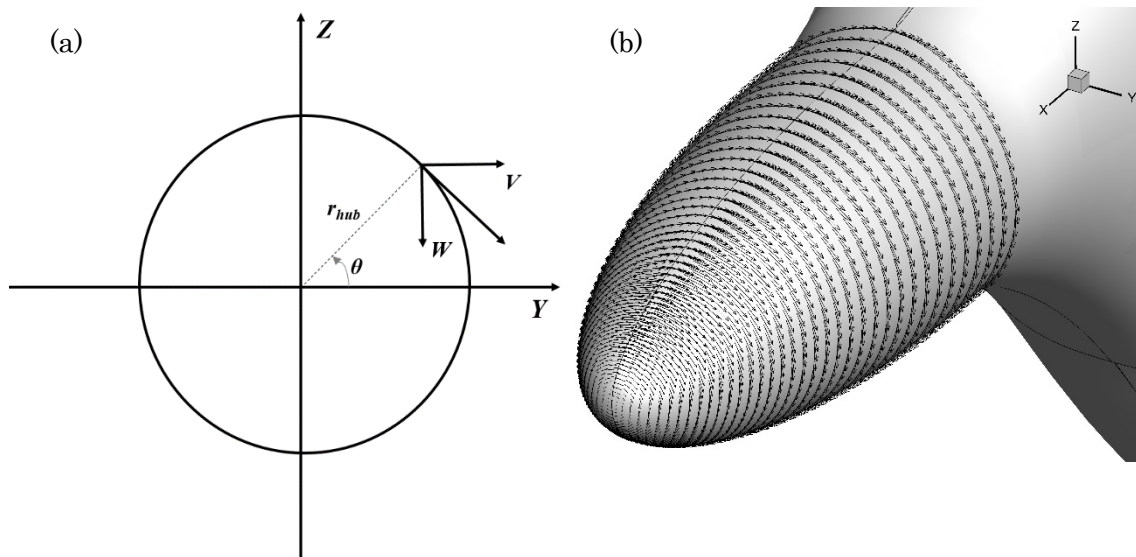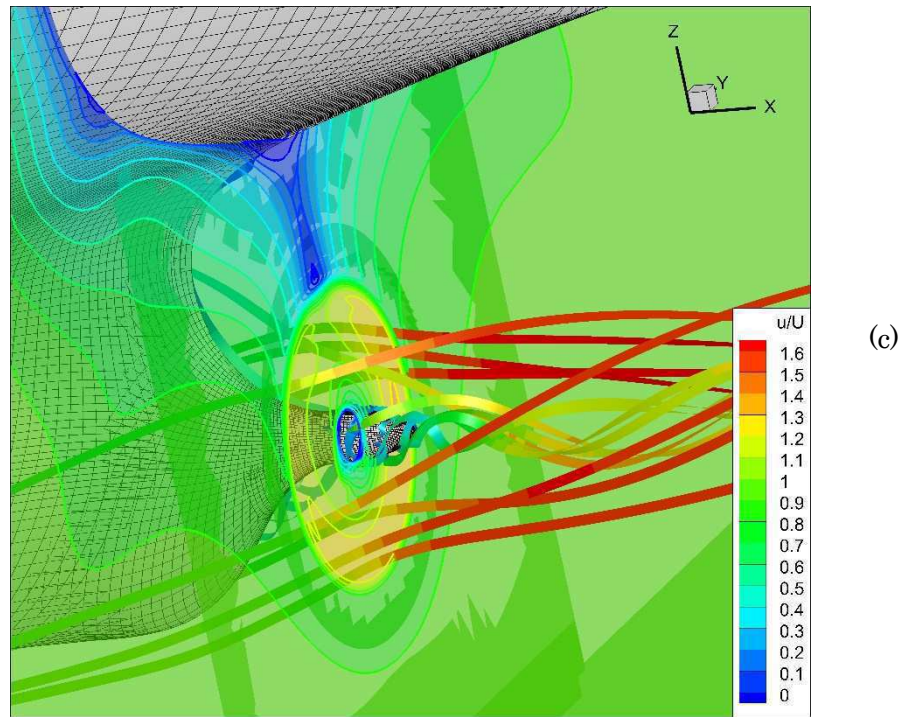
Fig. 4-4 (a) Schematic of rotating hub boundary condition (b) Rotating vectors on hub surface. (c) Swirling streamlines around hub.

The whole computational domain consists of nine blocks; boundary layer (port & starboard), stern bulb (port & starboard), hub (port & starboard), propeller, wake refinement and the background. The computational grid blocks are overlapping and combined together as illustrated in Fig. 4-5. Since the wall function is not used in this research, the non-dimensional grid size normal to the hull surface is taken as 1×10^{-6} to capture the boundary layer and turbulence. The grid is generated carefully around the free surface to capture the wave length and wave height and also to avoid strong numerical dissipation. The grid points along the x-axis is nearly 80 per wave length and along the z-axis is about 15 per wave amplitude. A Cartesian wake refinement block is created near the ship stern enclosing the propeller region to capture the complicated wake field in detail. The outmost part of the domain is the Cartesian background block

to present the flow field far from the ship. The grid topology and the grid points for the computational blocks are summarized in Table 4-4. In total of 8M (Million) grid points are used for the computations.

Fig. 4-5 Overset grid system for KVLCC2.

Table 4-4 Grid system details.

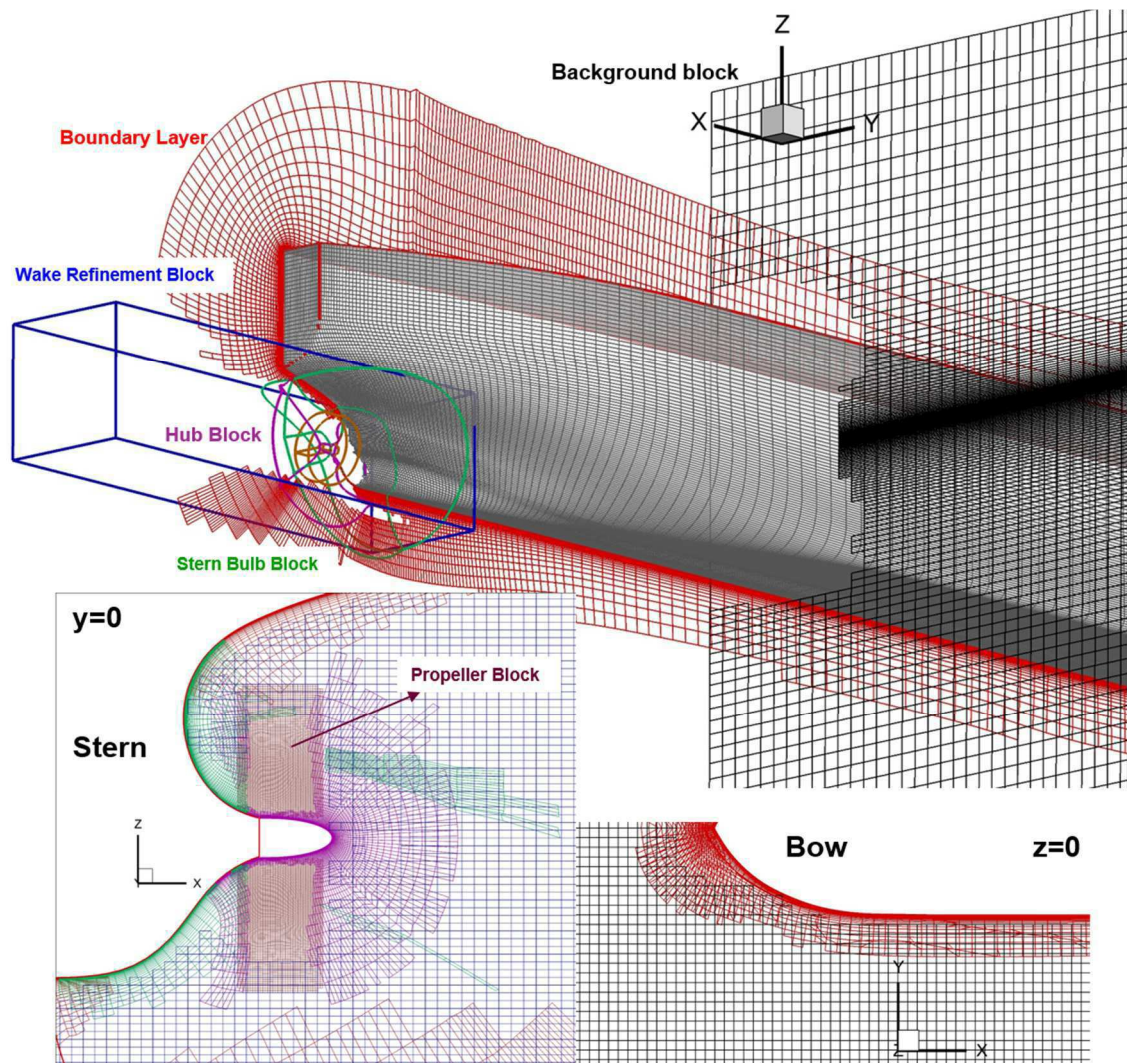| Block Name	Topology	$imax \times jmax \times kmax$ (Grid Points)
Boundary Layer (starboard)	O	$154 \times 50 \times 144$
Boundary Layer (port)	O	$154 \times 50 \times 144$
Stern Bulb (starboard)	O	$55 \times 50 \times 40$
Stern Bulb (port)	O	$55 \times 50 \times 40$
Hub (starboard)	O	$55 \times 50 \times 40$
Hub (port)	O	$55 \times 50 \times 40$
Propeller	O	$35 \times 111 \times 105$
Wake Refinement	H	$151 \times 81 \times 81$
Background	H	$216 \times 121 \times 151$

4.3 RESULTS

4.3.1 Volume Mean Nominal Velocity

To understand the velocity change on the propeller plane, the volume average nominal wake velocity u_N is computed by integrating the axial velocity distribution on the propeller plane as shown in Eq. (37). Figure 4-6 shows the CFD results of u_N for one encounter period for λ/L=0.6, 1.1 and 1.6, compared with calm water. The incident wave crest is at the propeller plane (x/L=0.98) when t/T_e=0. The colored solid lines for waves represent the diffraction problem results and the dashed lines represent the results for the ship in waves with 2DOF motions: free to heave and pitch (Wu et al., 2013). There is no significant phase lag in the simple harmonic oscillation for the diffraction results while there is around t/T_e=0.2 phase lag and clear 2nd harmonic components for longer wave cases with motions. For short wave case λ/L=0.6 with motions, the phase lag and 2nd harmonic components are very small and similar to the diffraction problem due to

small ship motions. The effect of the velocity change on the propeller plane on the propeller performance will be discussed in Chapter 5. The time average of the volume average nominal velocities $\overline{u_N}$ are summarized in Table 4-5. The $\overline{u_N}$ in waves with ship motions is higher than the calm water and diffraction values. It is also stated by Wu et al. (2013) that the largest $\overline{u_N}$ difference occurs when the λ/L=1.1 with motions. The calm water value, which is written in Table 4-5, was computed when the ship has sinkage and trim by (Wu et al., 2013). It is seen in Table 4-5 and Fig. 4-6; the $\overline{u_N}$ values for the diffraction problem are very close to the calm water one.

$$u_N = \frac{1}{\pi(R^2 - r_{hub}^2)} \int_{r_{hub}}^{R} u\, dA \tag{37}$$
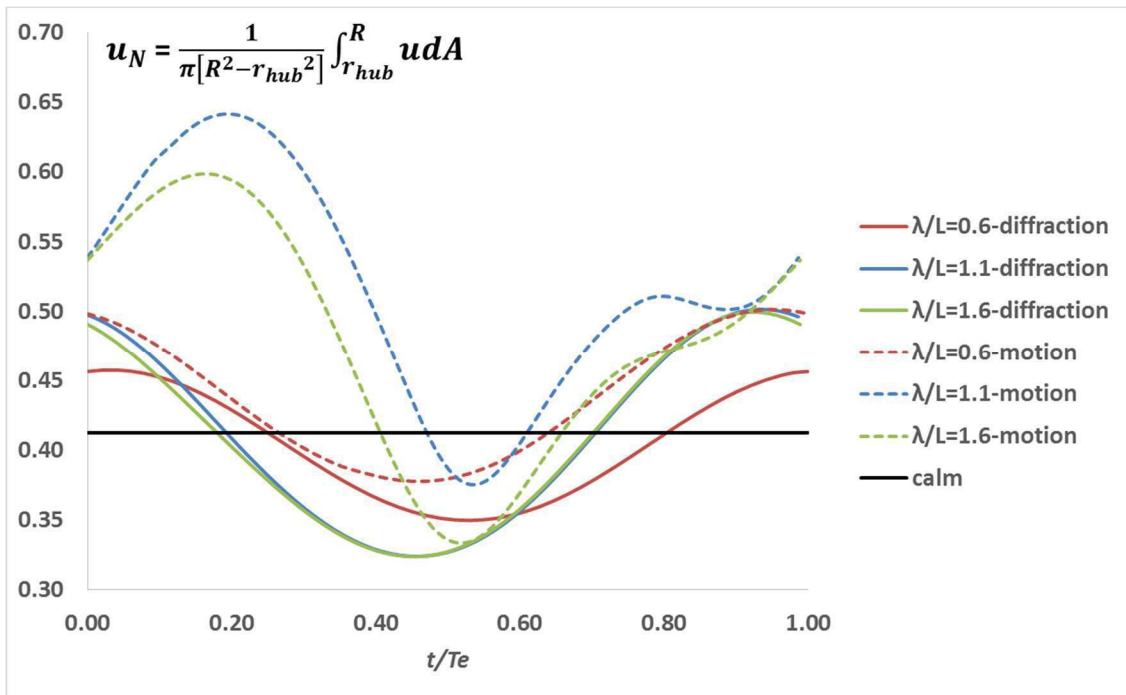
Fig. 4-6 Volume average nominal wake velocity.

Table 4-5 Time average of volume average velocity.

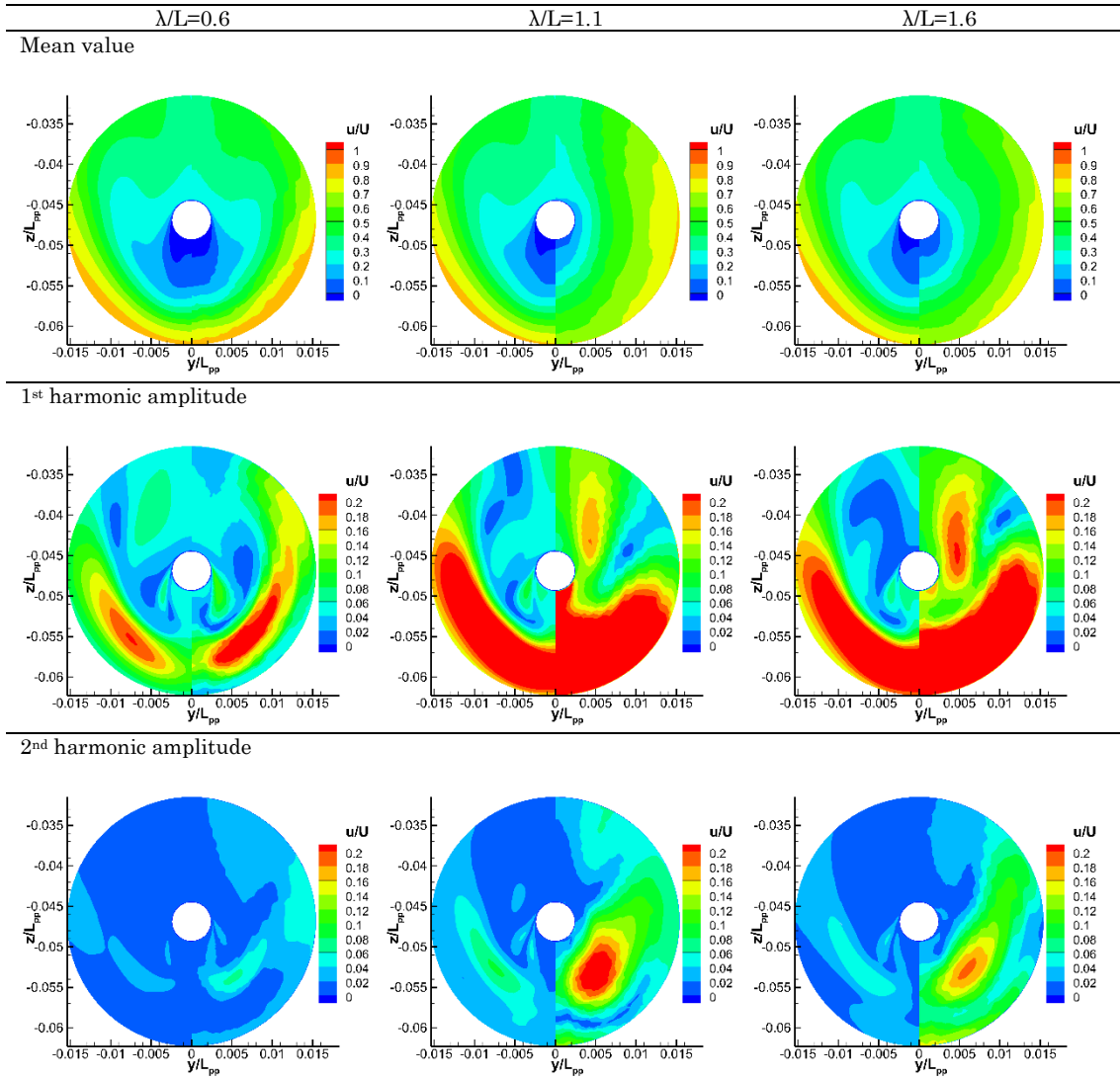|	$\overline{u_N}$ (diffraction)	$\overline{u_N}$ (with motions)
calm	-	0.4124
λ/L=0.6	0.4035	0.4391
λ/L=1.1	0.4111	0.5176
λ/L=1.6	0.4089	0.4780

Fig. 4-7 Fourier analysis on axial velocity distribution (Left: Diffraction cases, right: Ship in waves with motions).

Figure 4-7 (Left) shows the axial velocity harmonic components by Fourier analysis for λ/L=0.6, 1.1 and 1.6 (from left to right) for the diffraction problem. Figure 4-7 (Right) shows the axial velocity harmonic components by Fourier analysis for λ/L=0.6, 1.1 and 1.6 (from left to right) for ship with motions by Wu et al. (2013). The incident wave crest is at the ship bow (x/L=0.0) when t/T_e=0.

For the mean value component, Fig. 4-7 (Left) shows that the mean values for the diffraction problem when λ/L=0.6,1.1 and 1.6, are very similar to the one in calm water. It supports the conclusion in Wu et al. (2013) for the cases with motions: due to small ship motions, only shorter wave λ/L=0.6 has similar pattern to the one in calm water as seen in Fig. 4-7 (Right). The 1st harmonic amplitude is increased under the shaft for longer waves λ/L=1.1 and 1.6 for diffraction cases, which has similar pattern. It is caused by bilge vortex shedding from the hull body to the propeller plane. The 1st harmonic amplitude is increased under the shaft for longer waves λ/L=1.1 and 1.6 for ship with motions. It is caused by secondary vortex that is related to the low speed area changes. The 2nd harmonic amplitude also rises slightly for the longer waves λ/L=1.1 and 1.6, which is produced by the bilge vortex as well for diffraction and motion-free cases. The amplitudes are larger for the motion-free cases.

4.3.2 Analyses with the Body-force Model

It is stated that the velocity change at the propeller cross section is important for ship propulsive performance in waves. Figure 4-8 shows the axial-velocity contours and cross-flow vectors on the propeller plane in one encounter period for λ/L=0.6. When t/T_e=0.0, the wave crest is at the ship bow. Left figures are for the nominal wake and the right

ones represent the results with propeller. It is also shown by Wu et al. (2013) that the velocity inside the boundary layer is greatly affected by ship motions and waves due to pressure gradient and movement of bilge vortices. However, for diffraction problem (restrained from body motions), the lower speed area around the shaft and the bilge vortex shedding from the hull to downstream, only change slightly due to the waves as it is seen from the left figures. By looking at the right figures, the increased axial-velocity due to the induced velocities and the rotational motion are observed. The axial-velocity changes within one encounter period, it clearly increases due to waves on the starboard side after t/T_e=0.495 due to lower wave orbital velocity (the wave elevation rises).

The time history of the thrust coefficient for the calm water and diffraction problem cases are shown in Fig. 4-9 (Top). As it is seen, the thrust coefficient oscillation is simple harmonic and the amplitude increases with the increased wave length ratio. The mean thrust coefficient for the calm water is around 0.1936 and very close to the mean values for the diffraction cases, which are 0.193862 for λ/L=0.6, 0.193296 for λ/L=1.1 and 0.193264 for λ/L=1.6. According to these thrust coefficient values, the $\overline{u_N}$ for the diffraction cases is expected to be similar to the calm water one. Higher inflow velocity into the propeller plane results in lower thrust. It is also mentioned by Wu et al. (2013) that higher $\overline{u_N}$ in waves due to ship motions produces smaller thrust than the calm water case. As it is realized in Table 4-5, the $\overline{u_N}$ values in waves with motion are higher than the diffraction cases. Thus, the thrust values in waves with motion are expected to be lower than the diffraction problem values.

The time history of the wave elevation ($\zeta = Acos(-\omega_e t + kx)$) at the propeller plane is shown in Fig. 4-9 (Bottom). It is observed that there is nearly a 180 degree phase lag for all the wave length ratios; when the wave crest is at the propeller plane the thrust

coefficient has the minimum value. This is produced by the propeller inflow velocity change due to the wave orbital velocity. The same phenomena is captured for a propeller operating in waves in open water. The oscillating amplitude for thrust rises with the increased wave length as observed in Fig. 4-9 (Top).
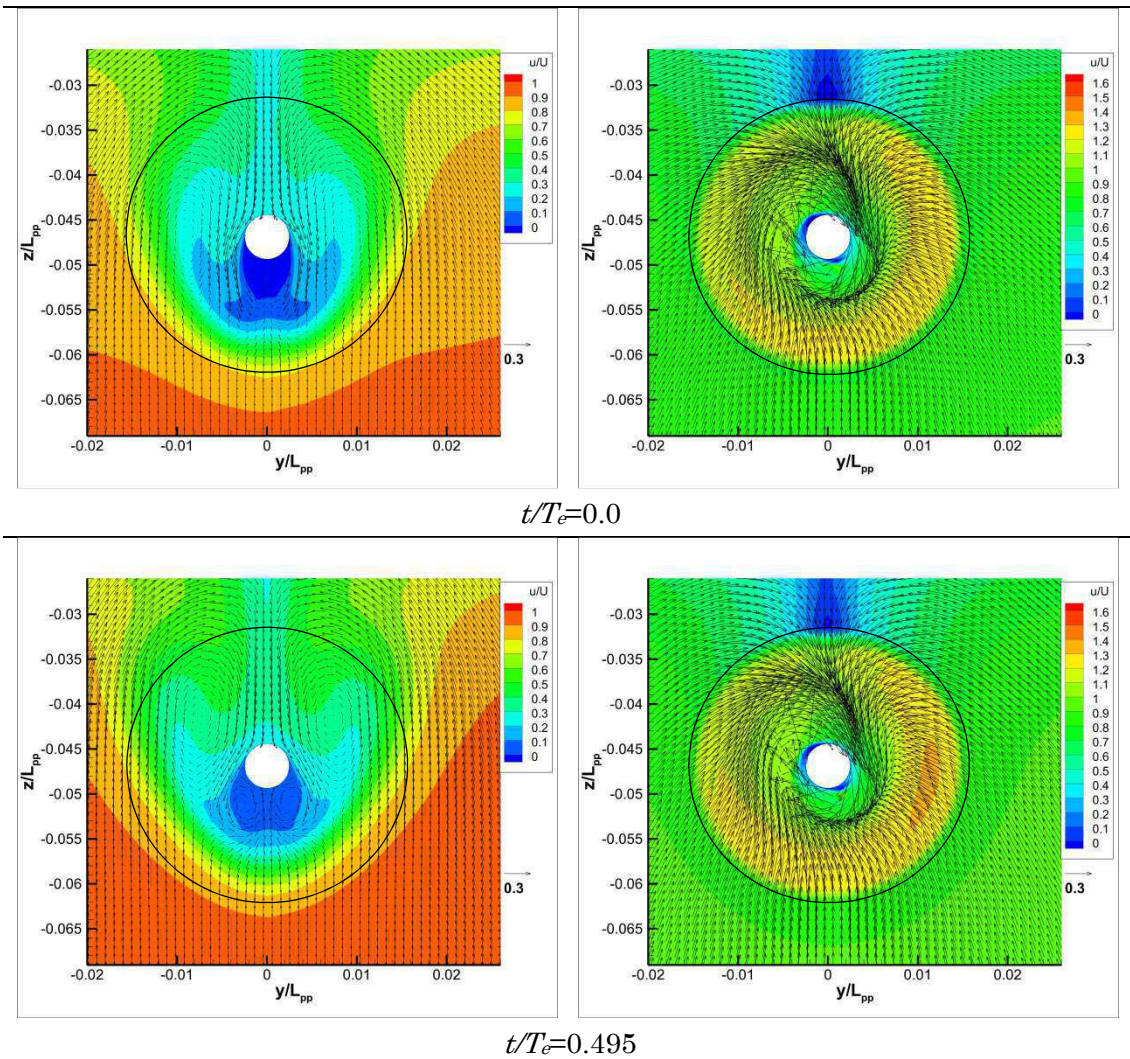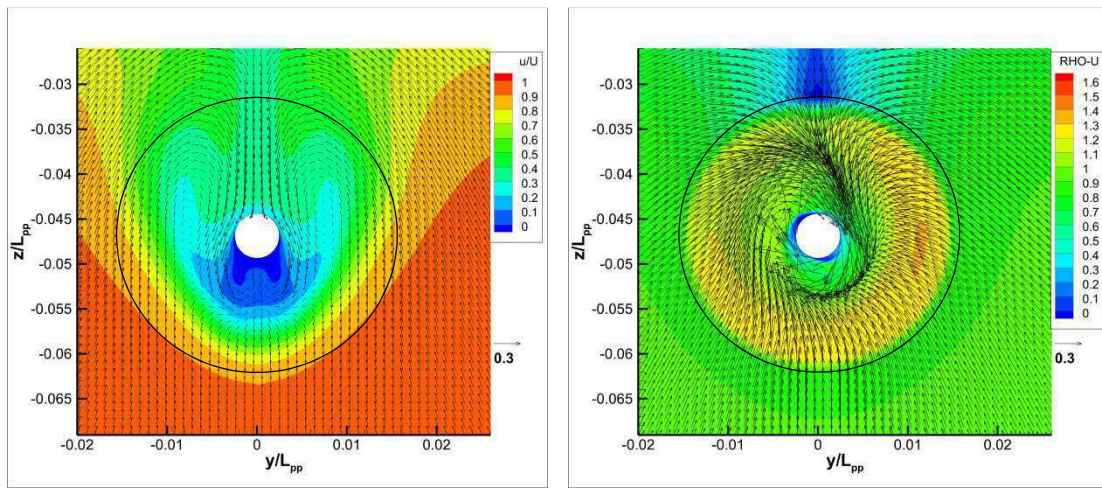

t/T_e=0.0

t/T_e=0.495

Fig. 4-8 Axial velocity in one encounter period for λ/L=0.6 for diffraction case
(Left: without propeller, right: with propeller).

t/T_e=0.75

Fig. 4-8 Axial velocity in one encounter period for λ/L=0.6 for diffraction case
(Left: without propeller, right: with propeller).
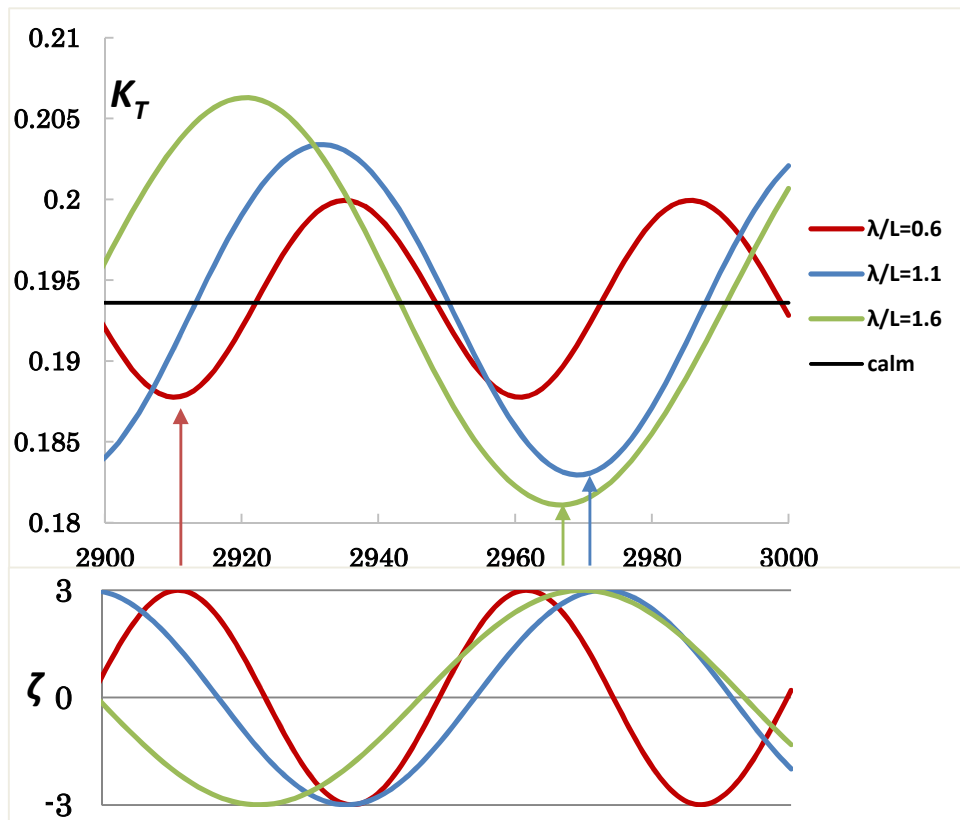
Fig. 4-9 Thrust coefficient and wave elevation time histories for diffraction.

4.4 DISCUSSION

A numerical study of the forward speed diffraction problem has been done for KVLCC2 model tanker. Six cases were considered; ship advancing in regular head waves (λ/L=0.6, 1.1 and 1.6) with propeller and without propeller for λ/L=0.6, 1.1 and 1.6. The body-force distribution model was employed to represent the propeller in the flow field. It is presented that the mean value for the diffraction problem is very similar to the calm water one based on the volume averaged axial velocity analysis, Fourier analysis, and thrust coefficient predictions. The thrust coefficient oscillates due to waves and the oscillation amplitude increases for longer waves. Moreover, the body-force model could capture the effect of propeller on the flow field.

CHAPTER 5: COMPUTATION OF A SELF-PROPELLED SHIP IN WAVES

In this chapter, the motions and the propeller performance of KVLCC2 at Fr=0.142 in regular head waves with wavelengths λ/L=0.6, 1.1 and 1.6 are predicted using body-force propeller model, which is presented in Chapter 2. The body-force propeller model with a simplified quasi-steady BET is coupled with the RANS code CFDSHIP-IOWA. The complicated flow field around the self-propelled ship in waves is investigated and the wake flow is compared with the PIV measurements. The simulation results for the thrust and time histories are compared with the PIV measurement results.

5.1 INTRODUCTION

The EFD (Experimental Fluid Dynamics) measurements and CFD simulations of KVLCC2 tanker at design Froude number Fr=0.142 in regular head waves without propeller were studied by Hayashi (2012) and Wu et al. (2013). The ship wake behavior in waves was analyzed in detail because of its significant effect on the propeller performance. From the EFD results, it was shown that the velocity in boundary layer is greatly affected by ship motions and waves due to the pressure gradient and movement of bilge vortices (Hayashi, 2012 and Wu et al., 2013).

5.2 EFD METHOD

The free surge tests were carried out in Osaka University towing tank. The basin length is 100 m, width is 7.8 m and depth is 4.35 m. It is equipped with a towing carriage, which is 7.4m long, 7.8m wide, and 6.4 m deep, running from 0.01 to 3.5 m/s. The basin is equipped with a plunger-type wave maker that can generate regular and irregular waves up to 500 mm wave height and wave length of 0.5 to 15m. The dimensions of the towing tank and the equipment details were also mentioned by (Okawa, 2015). The ship motion is 3DOF in PIV measurements: free to surge, heave and pitch. The main carriage is connected to a light weight carriage by means of a spring to allow the model to be free in surge motion while it is free to heave and pitch as shown in Fig. 5-1. The experimental system in waves was explained in detail by (Okawa, 2015). The system gives a constant external force and very small spring effect. The surge motion is adjusted for the PIV measurements by using this system. Also the mass of the model including the hull and pitch free gimbals, the mass of dynamometer and light weight carriage were mentioned (Okawa, 2015). The 2D PIV system, which is shown in Fig. 5-2 (Okawa, 2015), is used to measure the velocity distribution at the sections (including propeller plane at x/L=0.98) shown in Fig. 5-3. 32, 75 and 90 mm (millimeters) is the distance from AP (Aft Perpendicular) based on the 3.2 m long ship model. As presented in Fig. 5-2, three potentiometers are used to record surge, heave and pitch motions. Also, a wave height meter is utilized to measure the incident wave elevation.
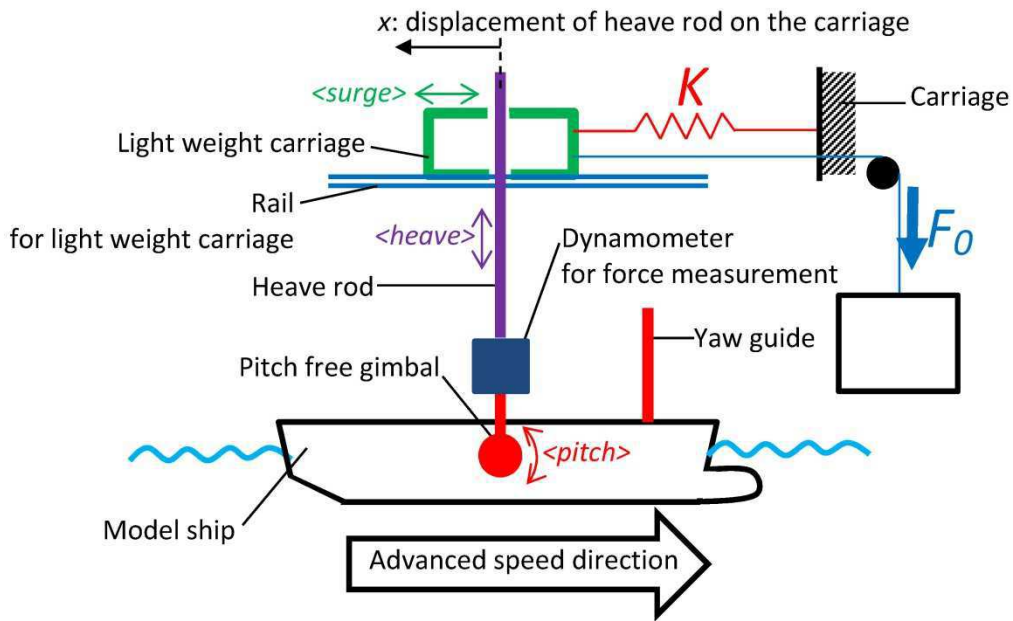
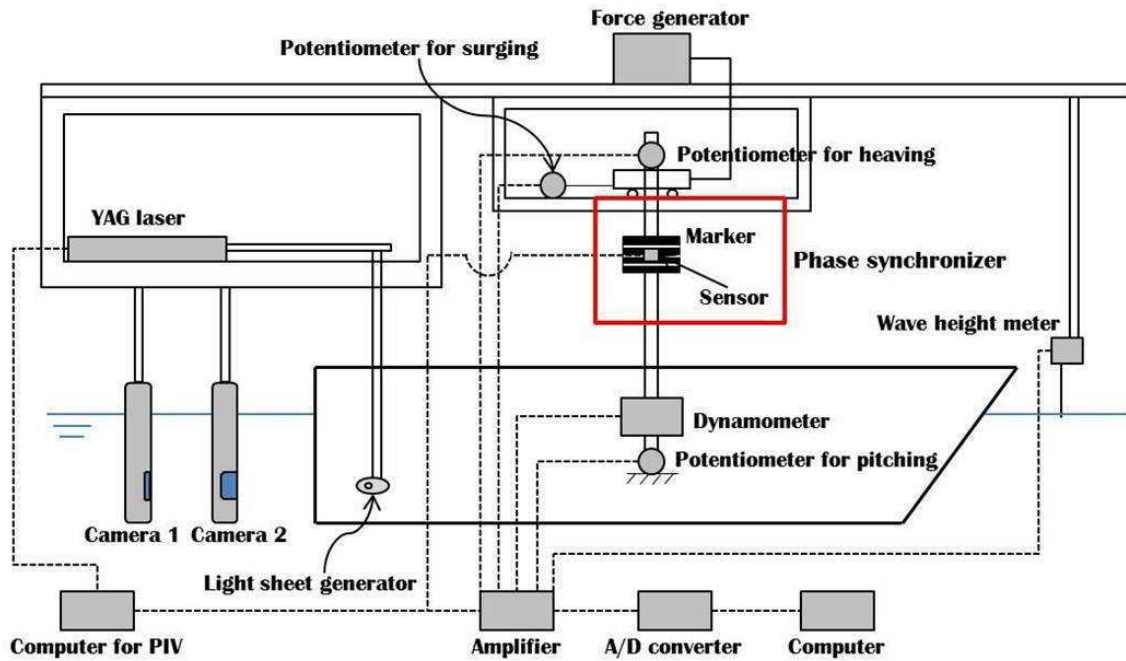Fig. 5-1 Experimental setup for free surge condition in waves.

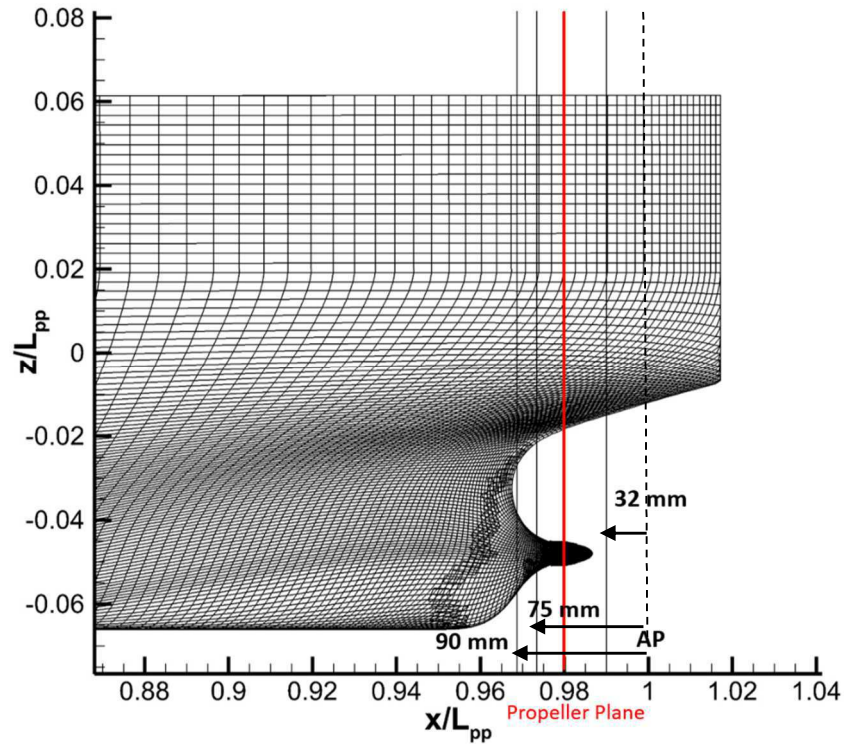Fig. 5-2 Schematic view of the PIV system.

Fig. 5-3 Cross sections of the PIV measurements and CFD.

The measurements are done for KVLCC2 ship model with the hub and propeller in fully-loaded condition. The main particulars of the model scale ship are summarized in Table 4-1 and propeller data are summarized in Table 4-2. The design speed of the ship model is 0.795 m/s which corresponds to Froude number Fr=0.142. The self-propulsion test was carried out for three different wave lengths λ/L=0.6, 1.1 and 1.6. The wave amplitude A=0.03m which corresponds to A/L=0.009375 was used for these wave lengths with consideration of the wave steepness h/λ≤1/30. All of the experimental conditions and coordinate system used in the measurements were mentioned by (Okawa, 2015). The number of revolution was determined as n_d=16.4 rps for λ/L=0.6, n_d=21 rps for λ/L=1.1 and n_d=15.8 rps for λ/L=1.6 for ship point of self-propulsion.

The external force F_0 is used in the experiments for avoiding large stretch of the

spring. Based on the analytical solution of 1DOF surge equation, which is shown in Eq. (38), appropriate values for spring stiffness K and F_0 are found,

$$m\ddot{x} + Kx = X - F_0 \tag{38}$$

where X is the hydrodynamic force, and x is the surge motion and m is the total mass of the moving parts including the model, hull and pitch free gimbals, dynamometer and light weight carriage.

The hydrodynamic force X cannot be recorded directly due to the nature of the EFD test setup, but the hydrodynamic force excluding inertial force $X' = X - m\ddot{x}$ can be recorded. Figure 5-4 (a) shows CFD result of the total hydrodynamic force (in Newton) time history for λ/L=0.6. And the total hydrodynamic force (in Newton) time history, which is estimated from experimental data, is plotted in Fig. 5-4 (b). A slight difference can be seen between the maximum and minimum values of the total hydrodynamic force for CFD and EFD results. However, the amplitude of the total hydrodynamic force is nearly the same for CFD and EFD ($\bar{X} = 2.9154$ (N) for CFD). The total hydrodynamic force time histories for λ/L=1.1 and λ/L=1.6 from CFD results are plotted in Fig. 5-5, below. The mean total hydrodynamic force is $\bar{X} = 4.1958$ (N) for λ/L=1.1 and $\bar{X} = 4.518$ (N) for λ/L=1.6.

Total Hydrodynamic Force - X

(a)

(b)
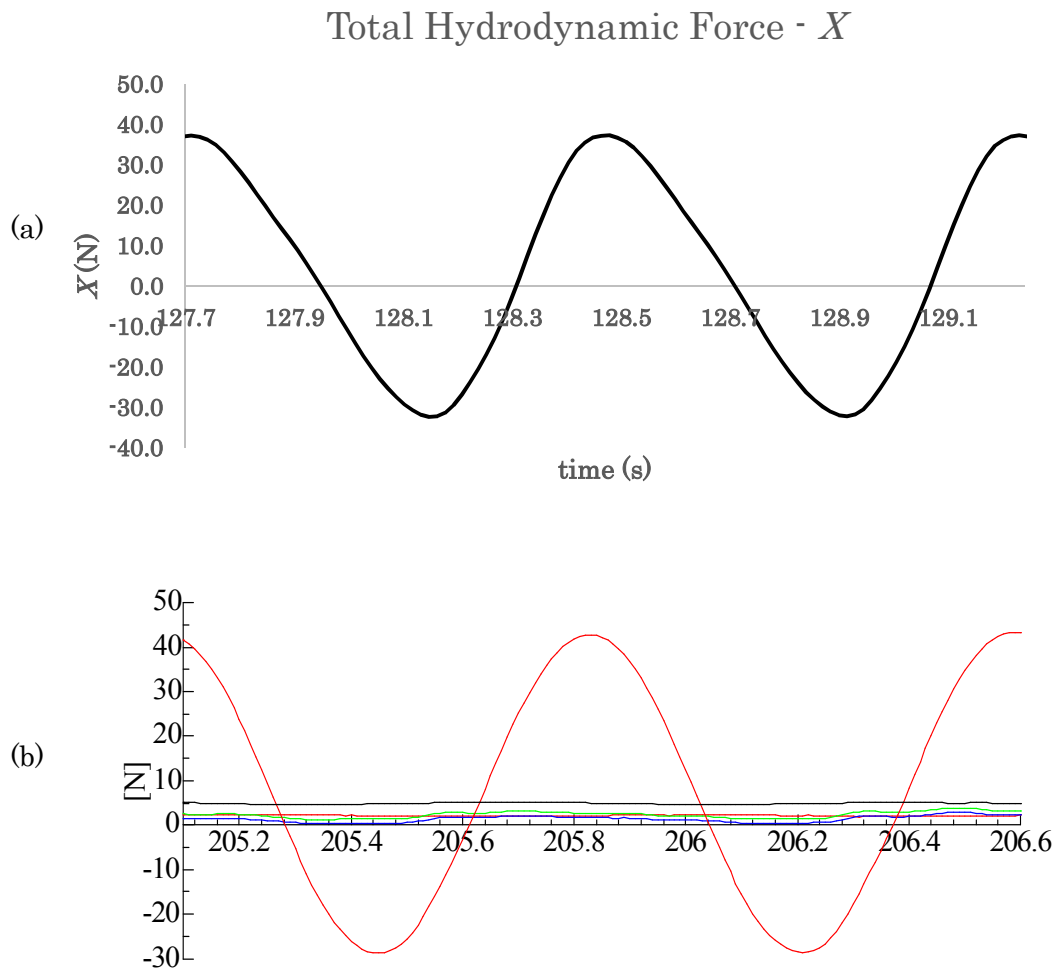
Fig. 5-4 (a) Total hydrodynamic force from CFD (λ/L=0.6).
(b) Total hydrodynamic force from EFD (λ/L=0.6).

5.3 CFD METHOD

The simulations are performed with RANS solver CFDSHIP-IOWA which has 6DOF, parallel and high performance computing (HPC) capabilities. The ship motion is 2DOF: free to heave and pitch with fixed surge motion in the simulations. In this chapter, SST k-ω turbulence model with no wall function is used for turbulent viscosity. The free

surface is modelled by a single phase level set method. All the variables and properties are non-dimensionalized by the ship length between perpendiculars L_{pp}, ship speed U_0, water density ρ and their combinations.

The time discretization schemes used in the turbulence and momentum equations were mentioned in Subsection 4.2.2. The projection method is applied for velocity-pressure coupling.
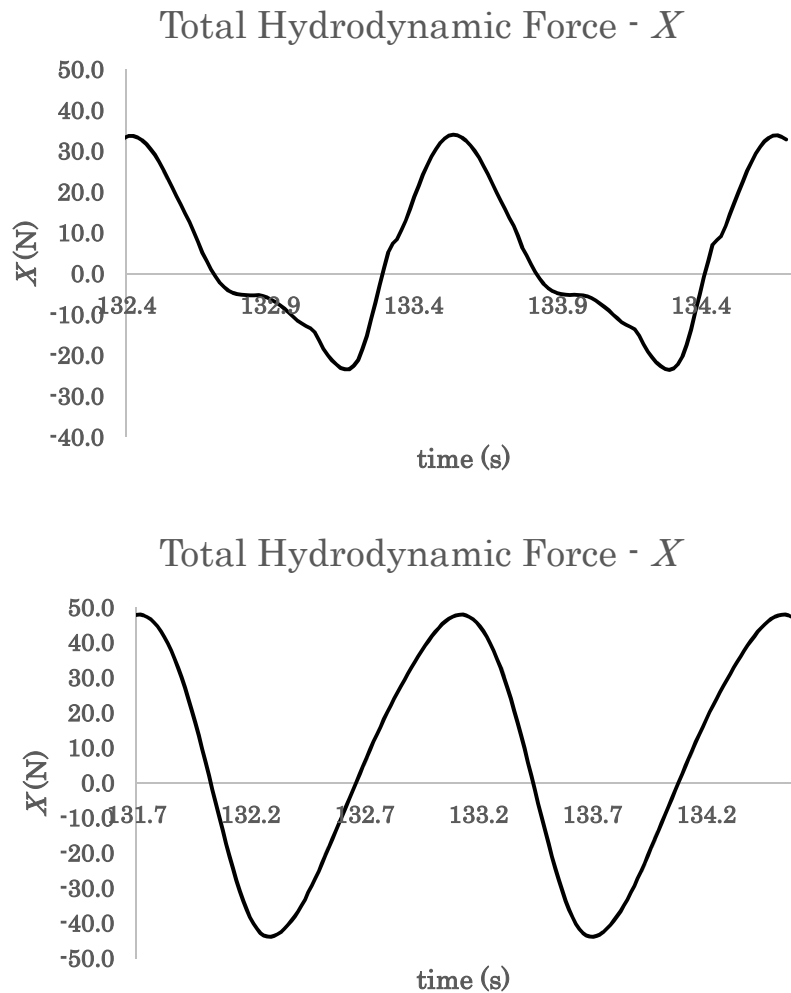

Fig. 5-5 Total hydrodynamic force from CFD
(Top: λ/L=1.1, T_e=1.12, Bottom: λ/L=1.6, T_e=1.41).

The computational domain with the boundary conditions were shown and listed in Subsection 4.2.2. The ship bow (FP) is located at x/L=0 and the stern (AP) is located at x/L=1. The y-axis is positive in starboard direction and the z-axis is positive in upper direction. The undisturbed free surface is laid on z/L=0 initially.

The computational domain consists of several independent grid blocks: the boundary layer (port & starboard), stern bulb (port & starboard), hub (port & starboard), propeller, wake refinement and background. The computational grids are overset and combined together. The details of the overset grid system including the grid topology and the grid points were explained in Subsection 4.2.2. The total grid point is 8M (Million). The simulations are carried out for the fully-loaded KVLCC2 ship model (main particulars are shown in Table 4-1) with the hub and propeller (main particulars of the propeller are shown in Table 4-2). The body-force distribution model is employed to represent the propeller effect on the flow field (Tokgoz et al., 2014). Within this method, the body-forces interact with the RANS solver and all the components of forces in x, y, z directions (T_x, T_y, T_z) and moments in x, y, z directions (Q_x, Q_y, Q_z) are considered in the 6DOF solver. The design speed of the ship model and the simulation cases are the same with EFD as mentioned in the previous chapter. The grid points along the x-axis is nearly 80 per wave length and along the z-axis is about 15 per wave height to capture the waves.

5.4 RESULTS

5.4.1 Time History

Figure 5-6 shows the comparison of thrust time history between EFD (3DOF) and CFD

(2DOF) for λ/L=0.6, 1.1 and 1.6 (from top to bottom) at ship point. The horizontal axis is non-dimensional time and the vertical axis is the thrust values in Newton (N) and the wave elevation at the propeller plane (x/L=0.98) in centimeters (cm). The solid lines represent the EFD measurement results and the dashed lines represent the CFD results. The thrust is shown by the purple lines, and the wave elevation at the propeller cross section is shown by the black lines. As it is seen from Table 5-1, the time histories of the thrust and the wave elevation show good agreement with the EFD measurement results. The average thrust values of EFD and CFD are very similar as understood from Table 5-1. The mean thrust values are obtained from the thrust time histories, which are presented in Fig. 5-6. The errors are insignificant, especially for λ/L=1.1 and 1.6. The average thrust coefficient values in waves with ship motions are lower than the ones in diffraction problem. For λ/L=0.6, the mean thrust coefficient for the diffraction problem is around 0.193862 (see Subsection 4.3.2) and higher than the mean value for the case with ship motions, which is 0.191006. This result confirms the volume average velocity values, which are compared with the diffraction problem in Table 4-5. As it is observed in Fig. 5-6, the fluctuation shape can be predicted very well by CFD. For the longer wave lengths, the higher harmonic and increasing oscillation amplitude occur in the thrust oscillation. It is shown that the phase lag is affected by the ship motions for different wave length ratio cases. For shorter wave length ratio (λ/L=0.6), the phase lag is closer to 180 degree due to small ship motions. The previous diffraction study, which is presented in Chapter 4, also supports this conclusion. However, there is a certain different phase lag with larger motions, i.e. the longer waves (λ/L=1.1 and 1.6). And, their increasing and decreasing slope of the thrust oscillation are clearly different. It might be related to the movement of bilge vortices relative to ship motions and the

pressure gradient between inner and outer boundary layer.

Table 5-1 The mean values of thrust for CFD and EFD.

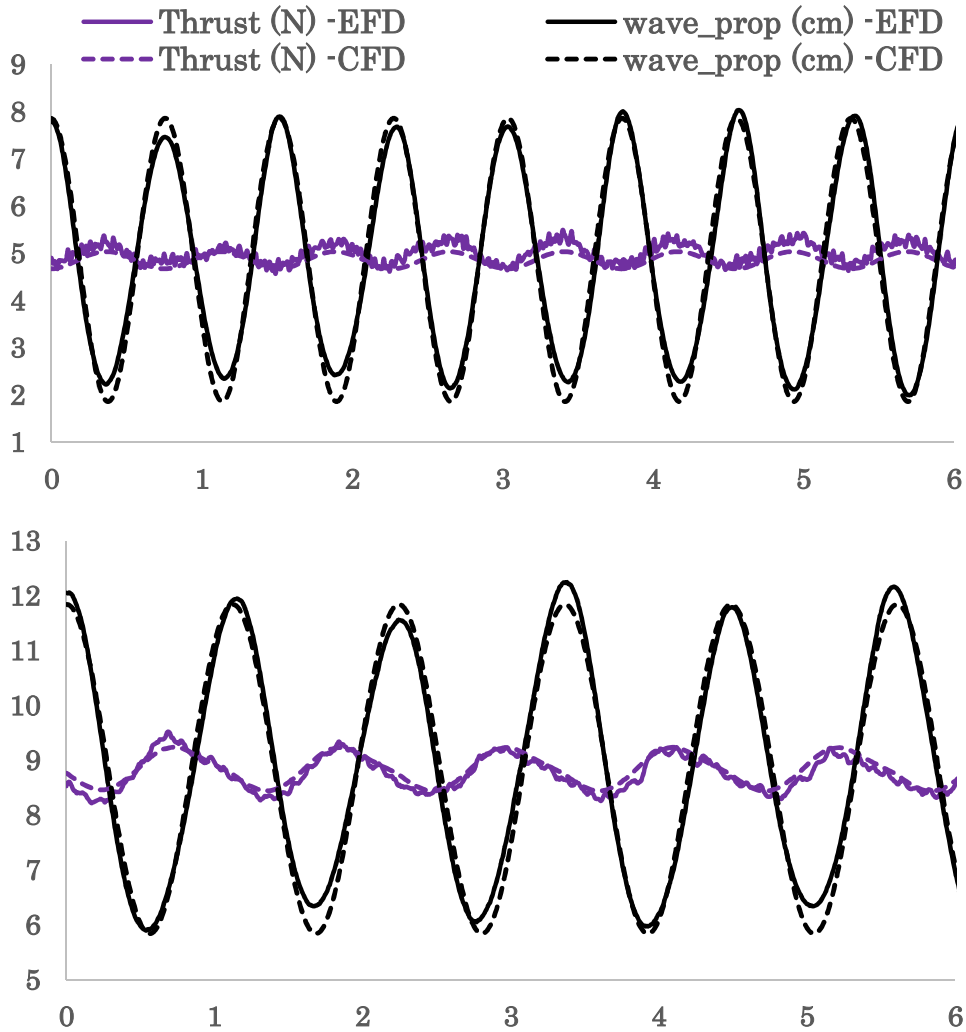|	n_d (rps)	CFD mean thrust value (N)	EFD mean thrust value (N)	*E%D*
λ/L=0.6	16.4	4.8567	5.0011	-2.8868
λ/L=1.1	21	8.8405	8.7632	0.8822
λ/L=1.6	15.8	4.5092	4.5478	-0.8496

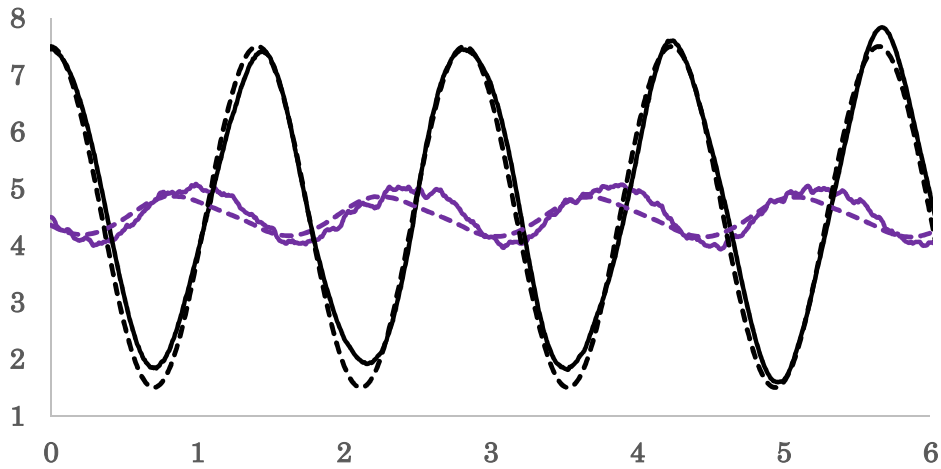Fig. 5-6 Thrust time history of EFD and CFD in λ/L=0.6, 1.1 and 1.6 (from top to bottom) at ship point.

Fig. 5-6 Thrust time history of EFD and CFD in λ/L=0.6, 1.1 and 1.6 (from top to bottom) at ship point.

5.4.2 Wake Field Analyses at Ship Point

The complicated flow field around the self-propelled ship in waves is investigated and the wake flow is compared with the PIV measurements. Figure 5-7 shows the ship motions comparison between EFD and CFD at ship point in λ/L=0.6 (Top) and in λ/L=1.1 (Bottom) for one encounter period (T_e). And, Fig. 5-8 shows the ship motions comparison between EFD and CFD at ship point in λ/L=1.6 for one encounter period. The solid lines represent the CFD results and the dashed lines show the EFD measurement results. The blue lines show the wave elevation in cm at the ship bow and the red lines show the wave elevation at the propeller cross section in cm. The green lines are for the heave motion in cm and the purple lines are for the pitch motion in degrees. The CFD results show good agreement with the experiment results. The amplitude of heave and pitch motions are very close for PIV and CFD. The mean heave values are summarized in Table 5-2 for EFD and CFD. The error is smallest when λ/L=1.1. However, there is a
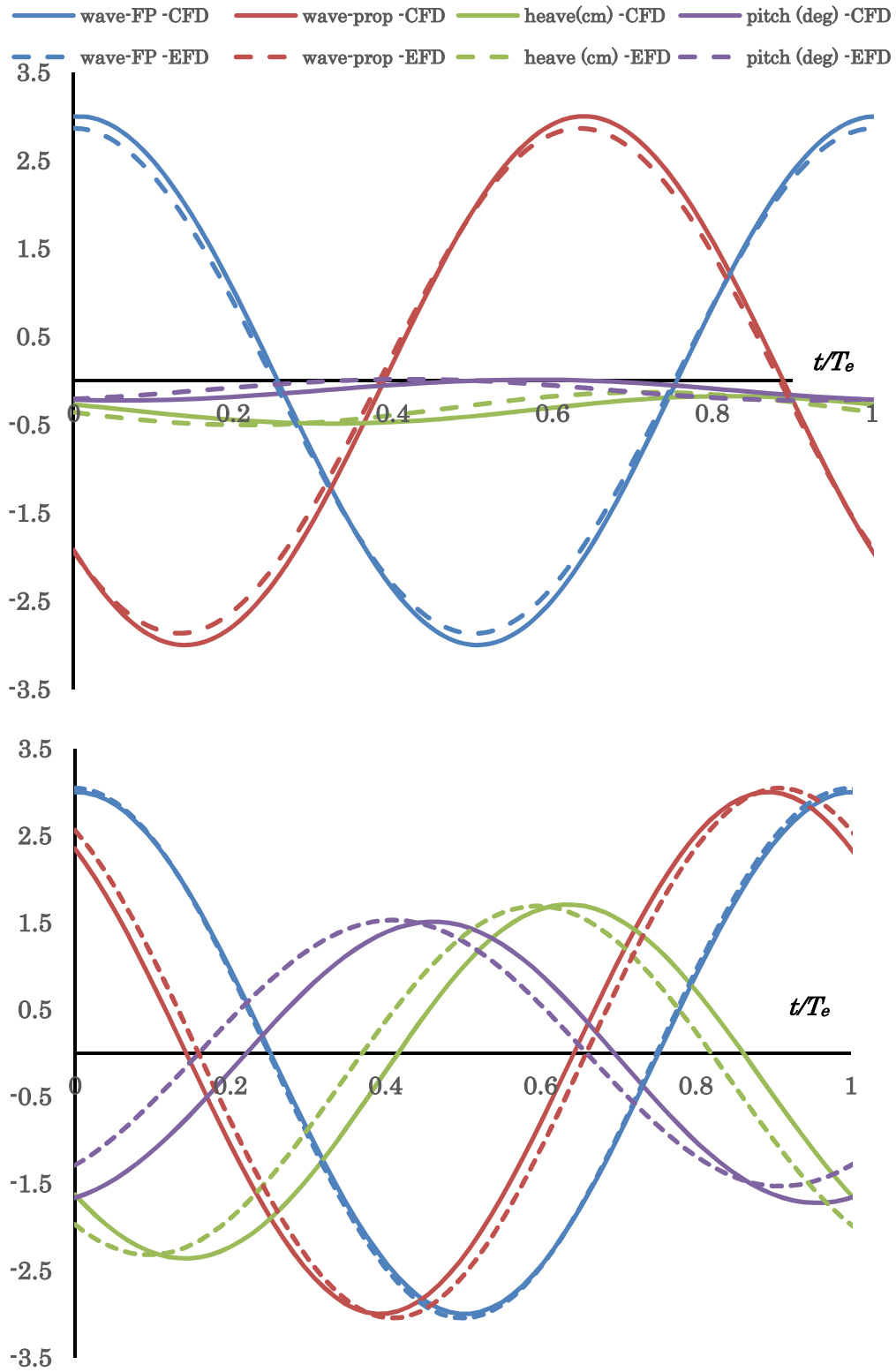
prominent phase difference for heave and pitch motions.

Fig. 5-7 Ship motions in λ/L=0.6 (Top) and λ/L=1.1 (Bottom) (EFD and CFD comparison).
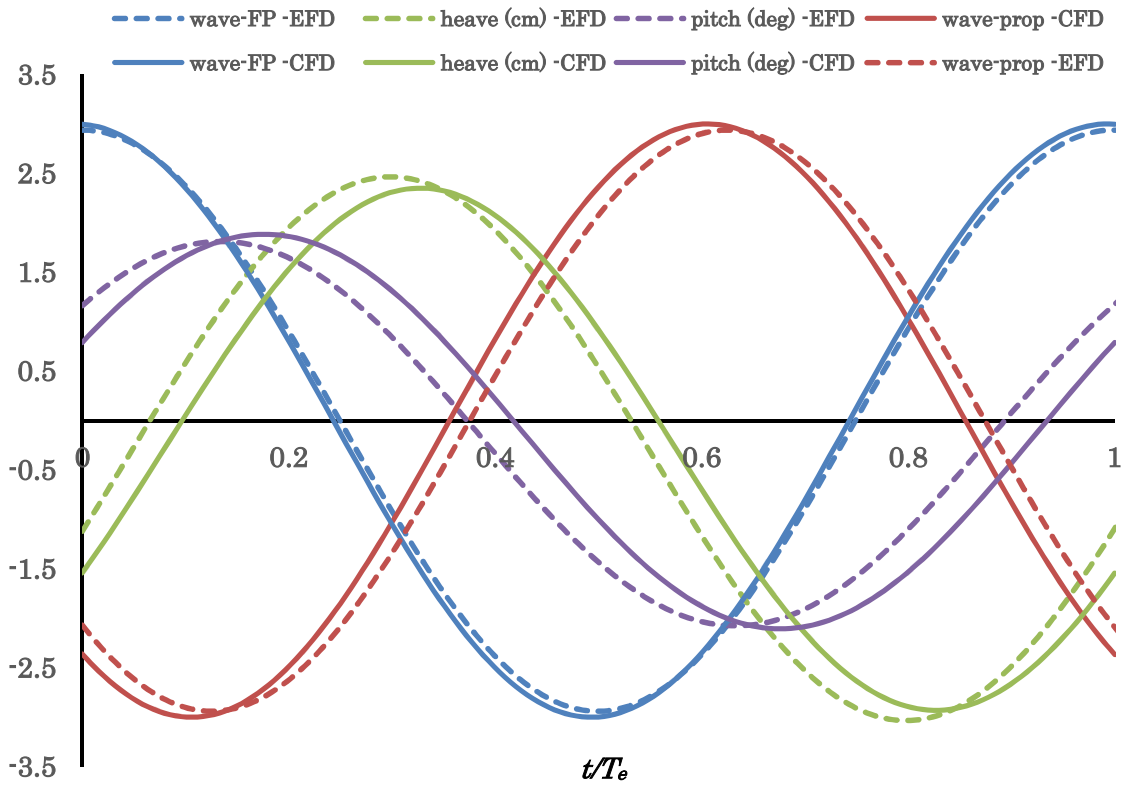
Fig. 5-8 Ship motions in λ/L=1.6 (EFD and CFD comparison).

Table 5-2 The mean value of heave motion of CFD and EFD.

	n_d(rps)	CFD mean heave value (cm)	EFD mean heave value (cm)	E%D
λ/L=0.6	16.4	-0.3348	-0.31	8.00
λ/L=1.1	21	-0.3420	-0.34	0.6
λ/L=1.6	15.8	-0.2781	-0.26	6.98

For the phase deviation, in CFD the error is caused by the space and time discretization. For EFD, several sources could induce damping effects in the oscillations, for instance, the friction among equipment.

The detailed flow field analyses are done for several sections as shown in Fig. 5-3 for PIV measurements and CFD. The sections are located at the propeller section, 32 mm

before the AP (x/L=0.99), 75 mm before the AP (x/L=0.977) and 90 mm before the AP (x/L=0.972). The figures are in one encounter period. And the wave crest is at FP at t/T_e=0. Figure 5-9 shows the axial velocity contours and cross flow vectors at x/L=0.977, upstream of the propeller for λ/L=0.6. Left figures are the results from PIV measurements and right figures are the CFD results. At this cross section, the flow field is greatly affected by the propeller. As it is seen from Fig 5-9, the axial velocity starts increasing within the propeller diameter and the boundary layer gets thinner. The axial velocity changes periodically as the phase changes in waves. The CFD results show good agreement with the PIV measurement results in general.

Figure 5-10 shows the axial velocity contours and cross flow vectors in one encounter period at x/L=0.99, downstream of the propeller for λ/L=0.6. PIV measurement results are shown on the left side and CFD results are shown on the right side. The axial velocity increases and the rotation of the propeller can be observed from the velocity contours and vectors. As is it seen, PIV and CFD have very similar results. It is clear that the vector field is twisted more severe in the starboard than that in the port side because of the clockwise rotating propeller and the upward stern flow. The axial velocity is slightly higher in the starboard side as well. Since the ship motions are small for λ/L=0.6, the difference of the axial velocity between the phases is not significant.
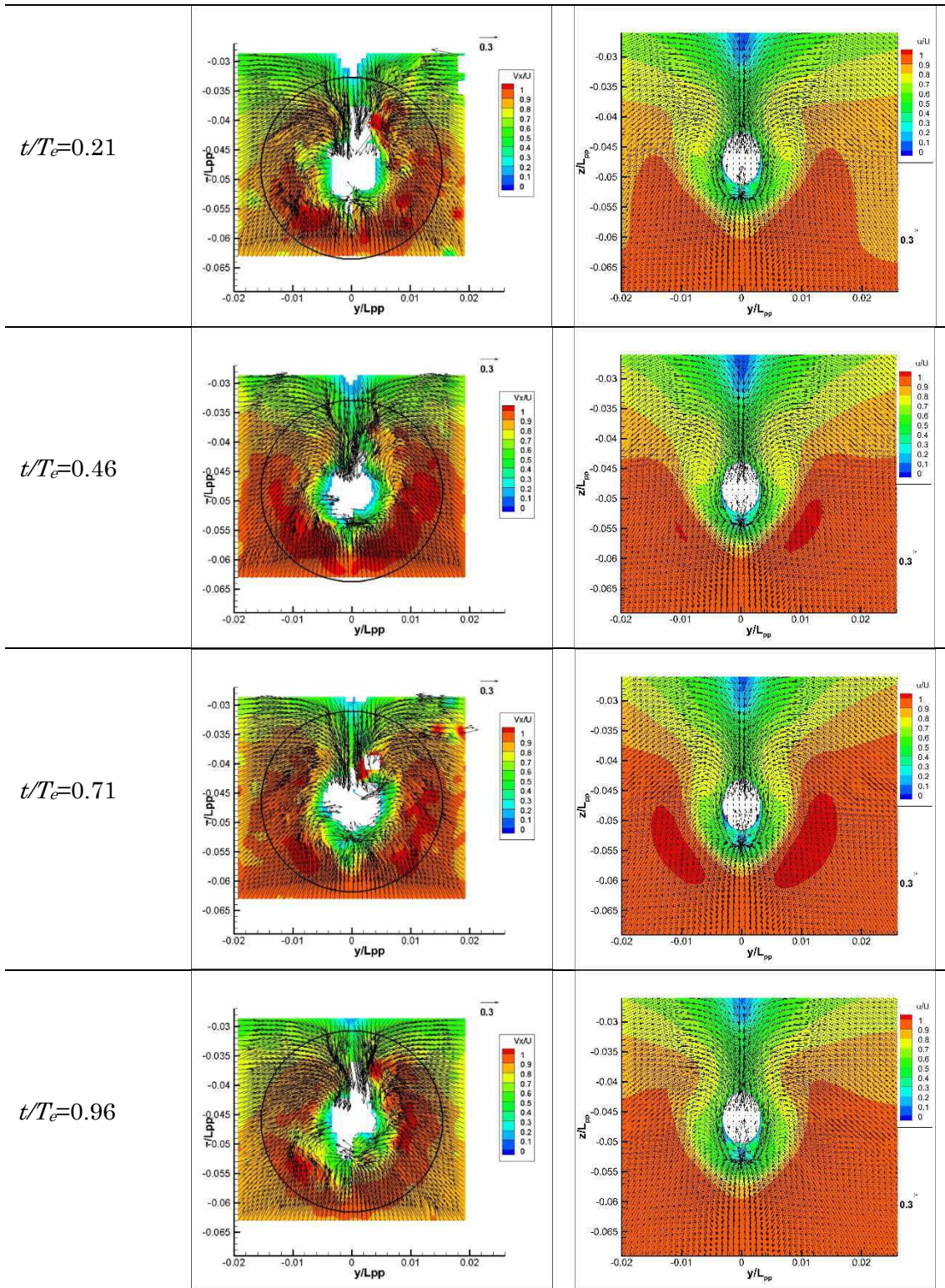
Fig. 5-9 Axial velocity in one encounter period for λ/L=0.6 at *x*/L=0.977
(Left: PIV, Right: CFD).

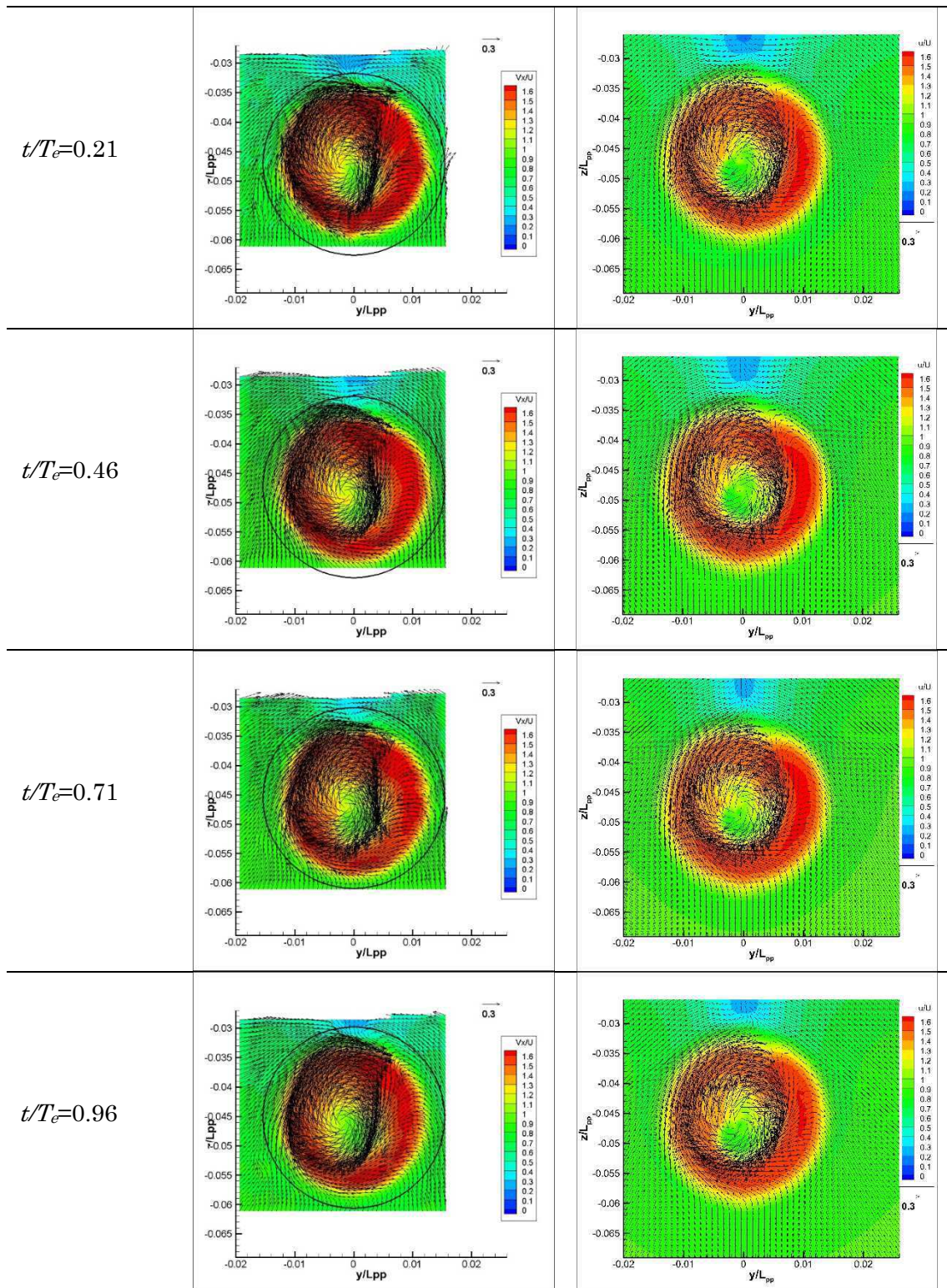Fig. 5-10 Axial velocity in one encounter period for λ/L=0.6 at *x*/L=0.99
(Left: PIV, Right: CFD).

86

The axial velocity contours and cross flow vectors in one encounter period at x/L=0.99, downstream of the propeller for λ/L=1.1 at ship point are plotted in Fig. 5-11. As it is seen, the ship motions are larger compared to λ/L=0.6, and it can be observed from the axial velocity contours. The difference of the velocity change between the phases are more obvious due to motions and waves. The cross flow vectors and velocity contours show good agreement between PIV measurement and CFD results. Figure 5-12 demonstrates the axial velocity contours and cross flow vectors in one encounter period at x/L=0.99 for λ/L=1.6 at ship point. The ship motions are largest in this case compared to λ/L=0.6 and λ/L=1.1. The velocity changes severely between the phases because of the large motions and waves. As a conclusion, the cross flow vectors and velocity contours show good agreement between simulation results and PIV measurements.

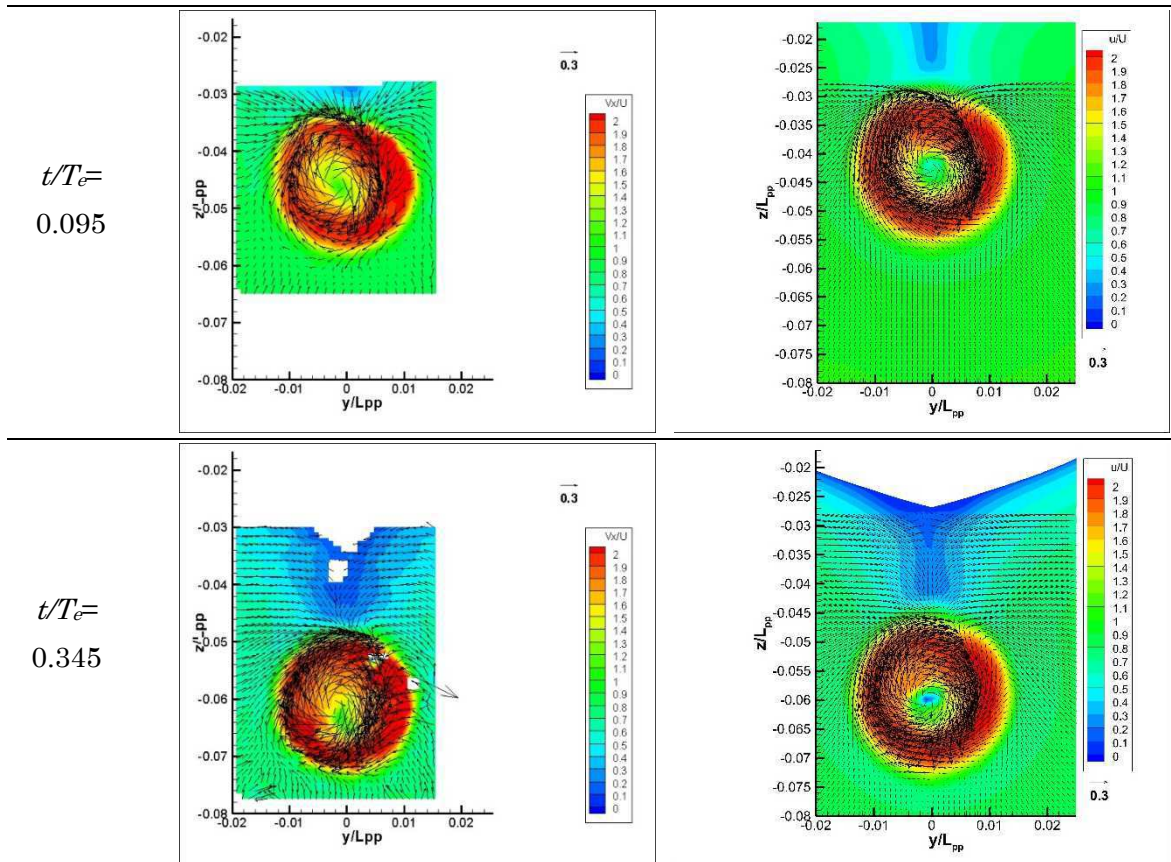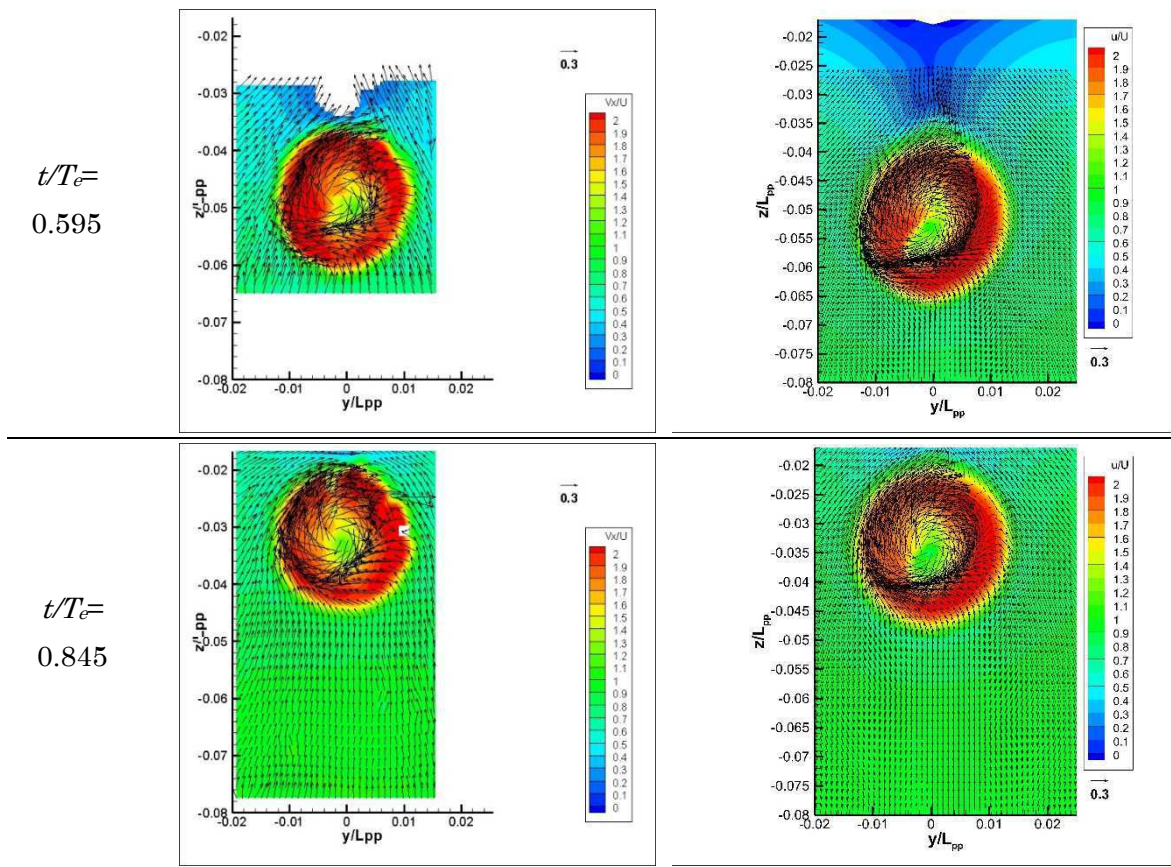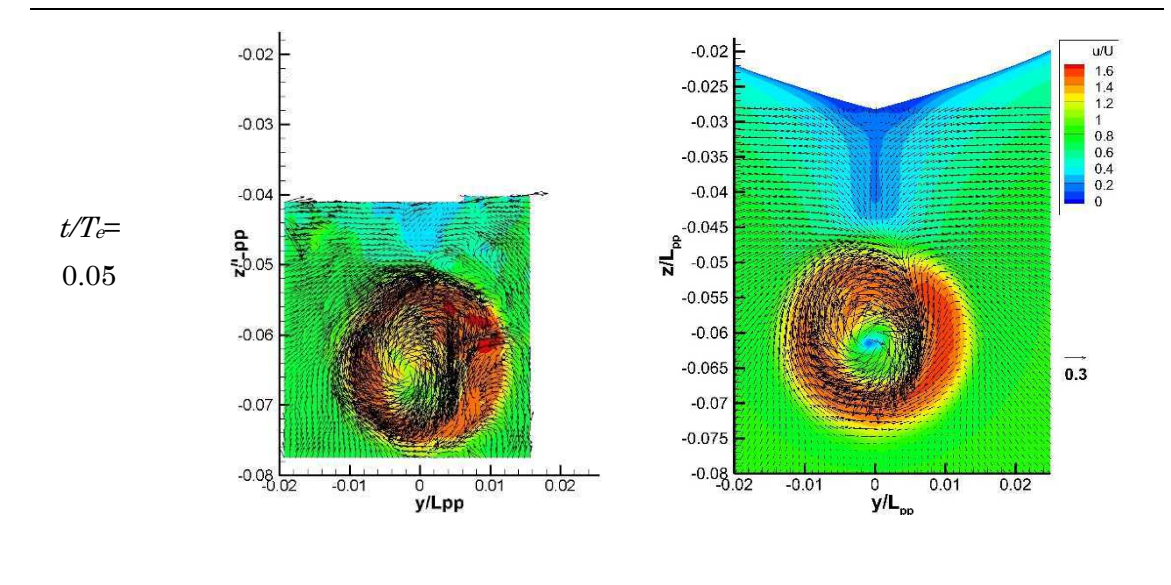Fig. 5-11 Axial velocity in one encounter period for λ/L=1.1 at x/L=0.99 (Left: PIV, Right: CFD).

Fig. 5-11 Axial velocity in one encounter period for λ/L=1.1 at *x*/L=0.99 (Left: PIV, Right: CFD).

Fig. 5-12 Axial velocity in one encounter period for λ/L=1.6 at *x*/L=0.99 (Left: PIV, Right: CFD).
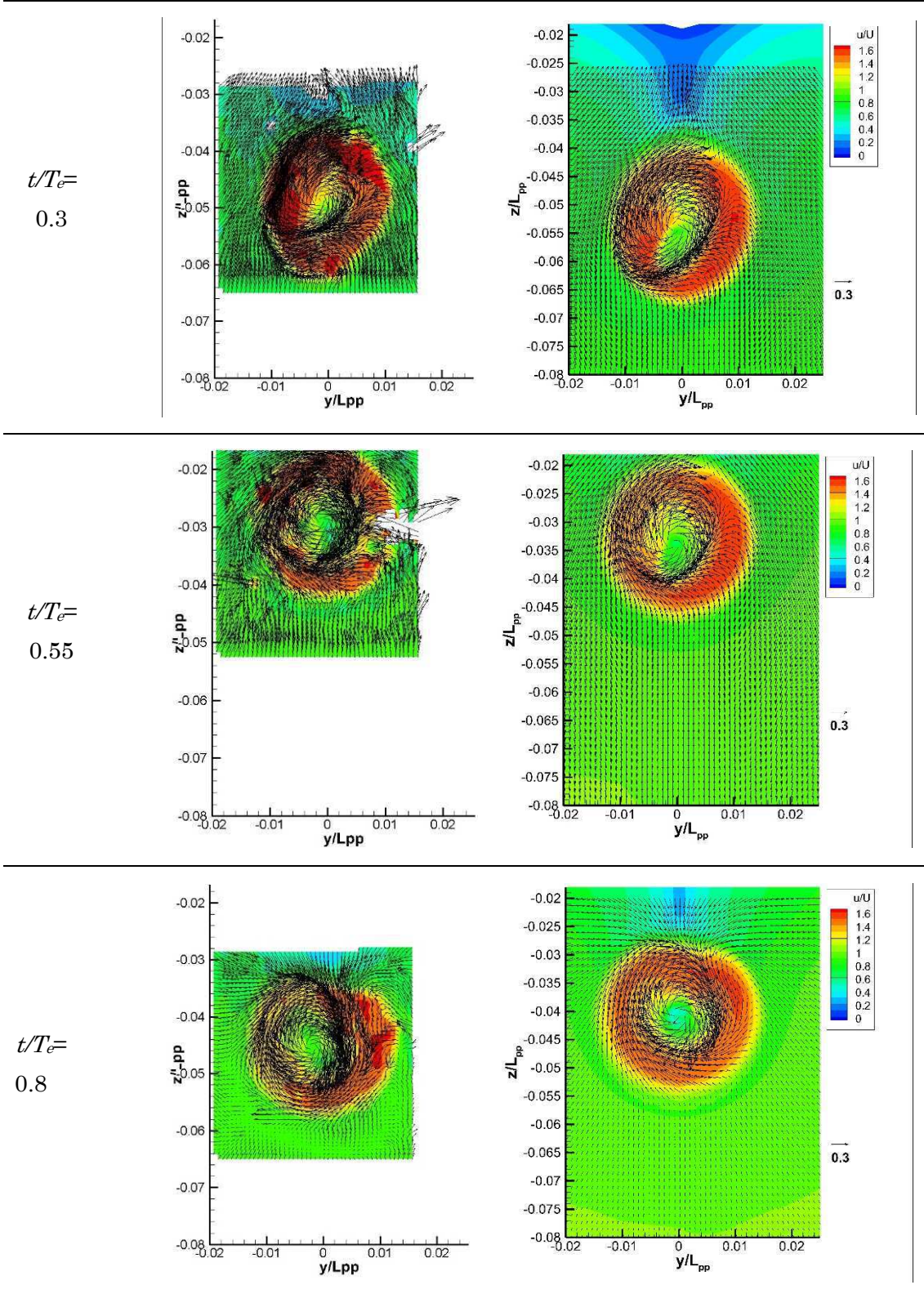
Fig. 5-12 Axial velocity in one encounter period for λ/L=1.6 at *x*/L=0.99 (Left: PIV, Right: CFD).

As it is stated, the side force produced by propeller cannot be treated in the equation of motions, if the axisymmetric prescribed body-force distributions based on ship speed or modified ship speed is used. On the other hand, with the current body-force propeller model the side forces and vertical forces can be calculated as presented in Subsection 2.3.2. For the application of maneuvering problem or ship to ship interaction cases, the side force produced by propeller becomes essential.

Figure 5-13 shows the comparison between KUM and current body-force propeller model for the thrust coefficient (a), side force coefficient F_y (b) and vertical force coefficient F_z (c) in ship coordinate for λ/L=0.6 in one encounter period. The solid green line represents the KUM result for λ/L=0.6 and the dashed green line represents the result for calm water. The solid black lines represent the results for the proposed body-force model. As seen from Fig. 5-13 (a), there is a significant numerical perturbation for KUM results and further investigation is necessary to find out the reason. The fluctuation shape of the thrust coefficient, F_y and F_z are similar for both models. However, the magnitude of F_z for both models are different than each other.

The body-force terms in y and z directions in propeller coordinate for the proposed body-force propeller model are illustrated in Fig. 5-14 for λ/L=0.6 in one encounter period. The colored vertical lines in Fig. 5-13 indicates the time when these body-force terms are plotted. It is confirmed from these two figures that the side and vertical forces changes by phase.

Fig. 5-13 (a) Thrust Coefficient (b) Side force coefficient (F_y) (c) Vertical force coefficient (F_z) in ship coordinate for λ/L=0.6 in one encounter period (comparison with KUM).

$t/T_e=0$

$t/T_e=0.25$

$t/T_e=0.5$

$t/T_e=0.75$

(a)   (b)

Fig. 5-14 Body-force terms in y and z direction for $\lambda/L=0.6$ in one encounter period.

Figure 5-15 shows the comparison between KUM and current body-force propeller model for the thrust coefficient (a), side force coefficient F_y (b) and vertical force coefficient F_z (c) in ship coordinate for $\lambda/L=1.1$ in one encounter period. The fluctuation shape of the thrust coefficient and F_y are similar for both propeller models. The mean thrust coefficient value in waves is slightly smaller than the one in calm water for KUM. Compared to Fig. 5-13, the vertical force coefficient value obtained by current body-force propeller model fluctuates more within one period due to larger motions. The change of side force coefficient F_y within one encounter is not significant while the vertical force coefficient F_z fluctuates expressively due to the ship motions and the wave orbital velocity. However, KUM could not show the 2nd harmonic components for F_z, while it is clearly shown by the current propeller model. Also, the magnitude of the vertical force coefficient for proposed body-force propeller model is much smaller than the KUM value. Further validation is required by EFD or real propeller simulations for these cases.

The body-force terms in y and z direction in propeller coordinate are explained in Fig. 5-16 for $\lambda/L=1.1$ in one encounter period. The colored vertical lines in Fig. 5-15 specifies the time when these body-force terms are plotted. Figures 5-15 and 5-16 correspond with each other.
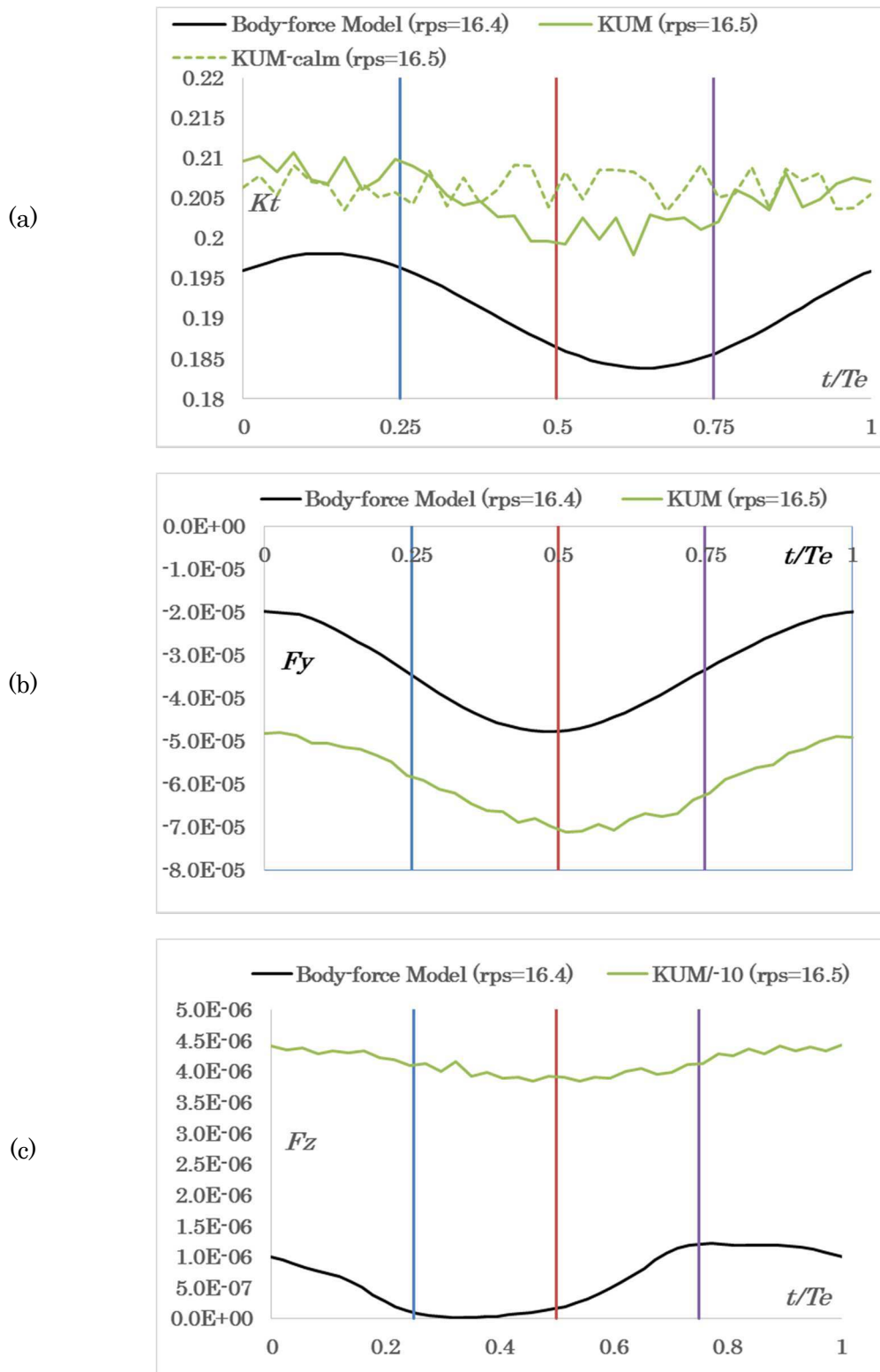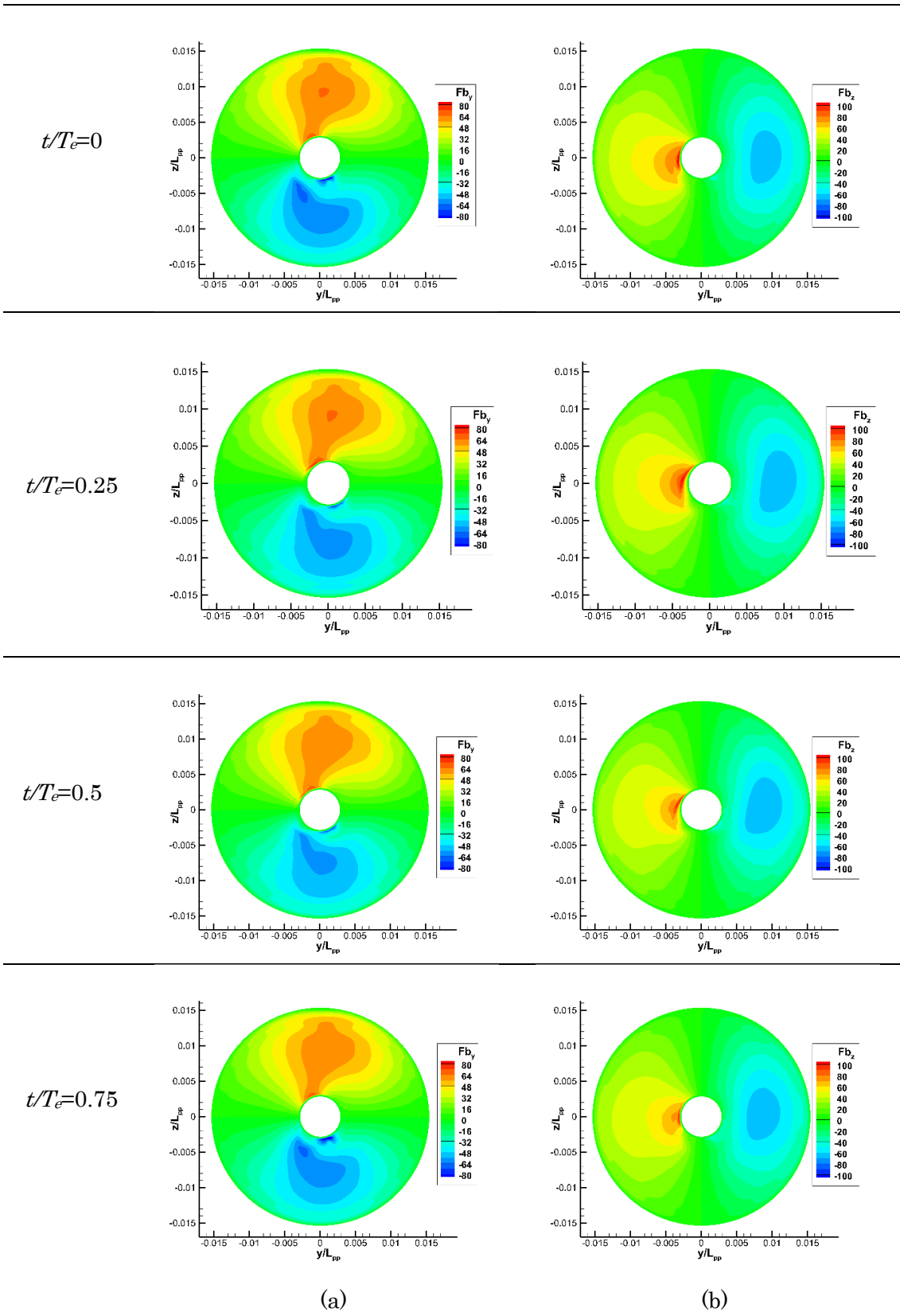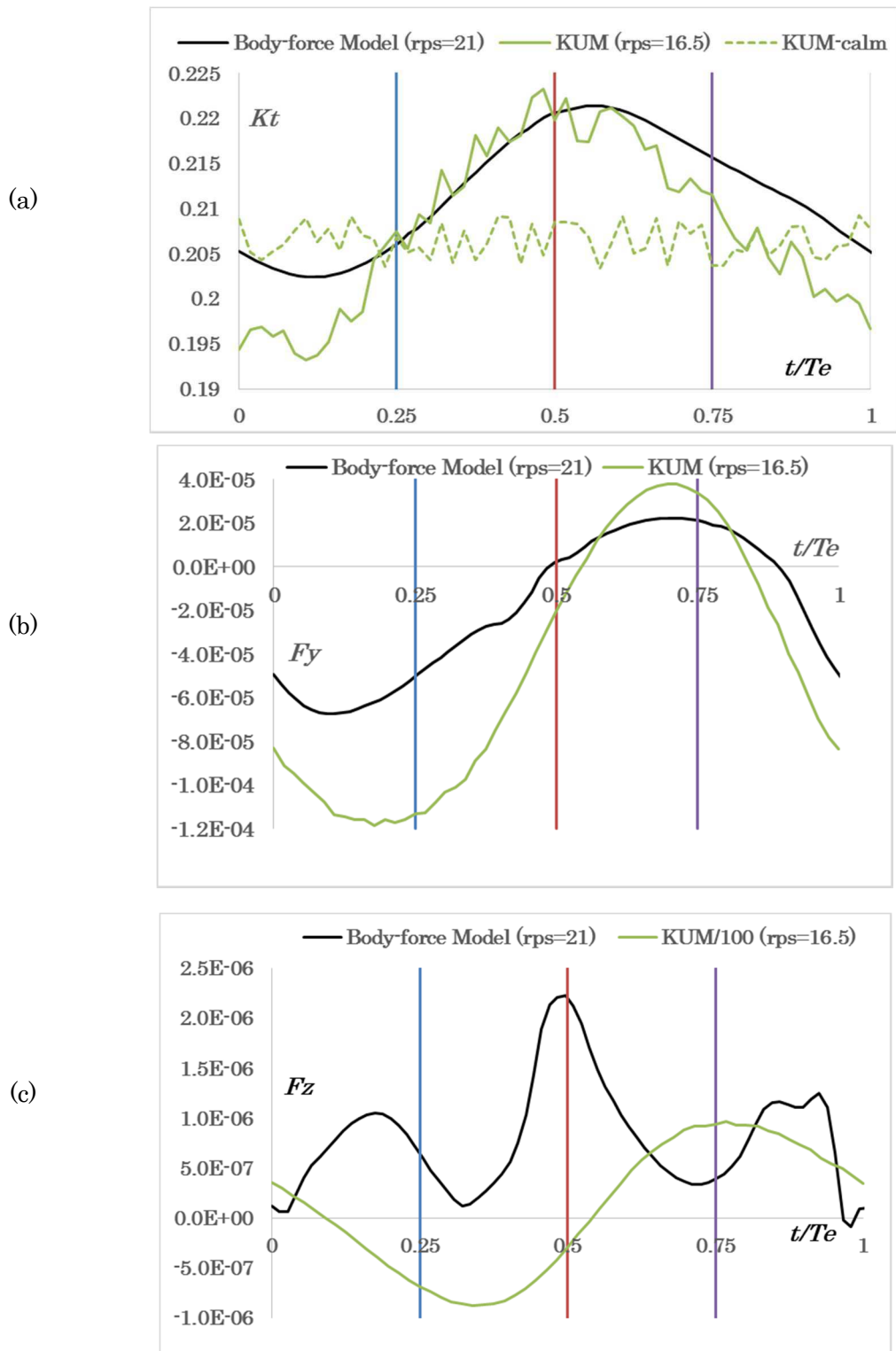
Fig. 5-15 (a) Thrust Coefficient (b) Side force coefficient (F_y) (c) Vertical force coefficient (F_z) in ship coordinate for λ/L=0.6 in one encounter period (comparison with KUM).
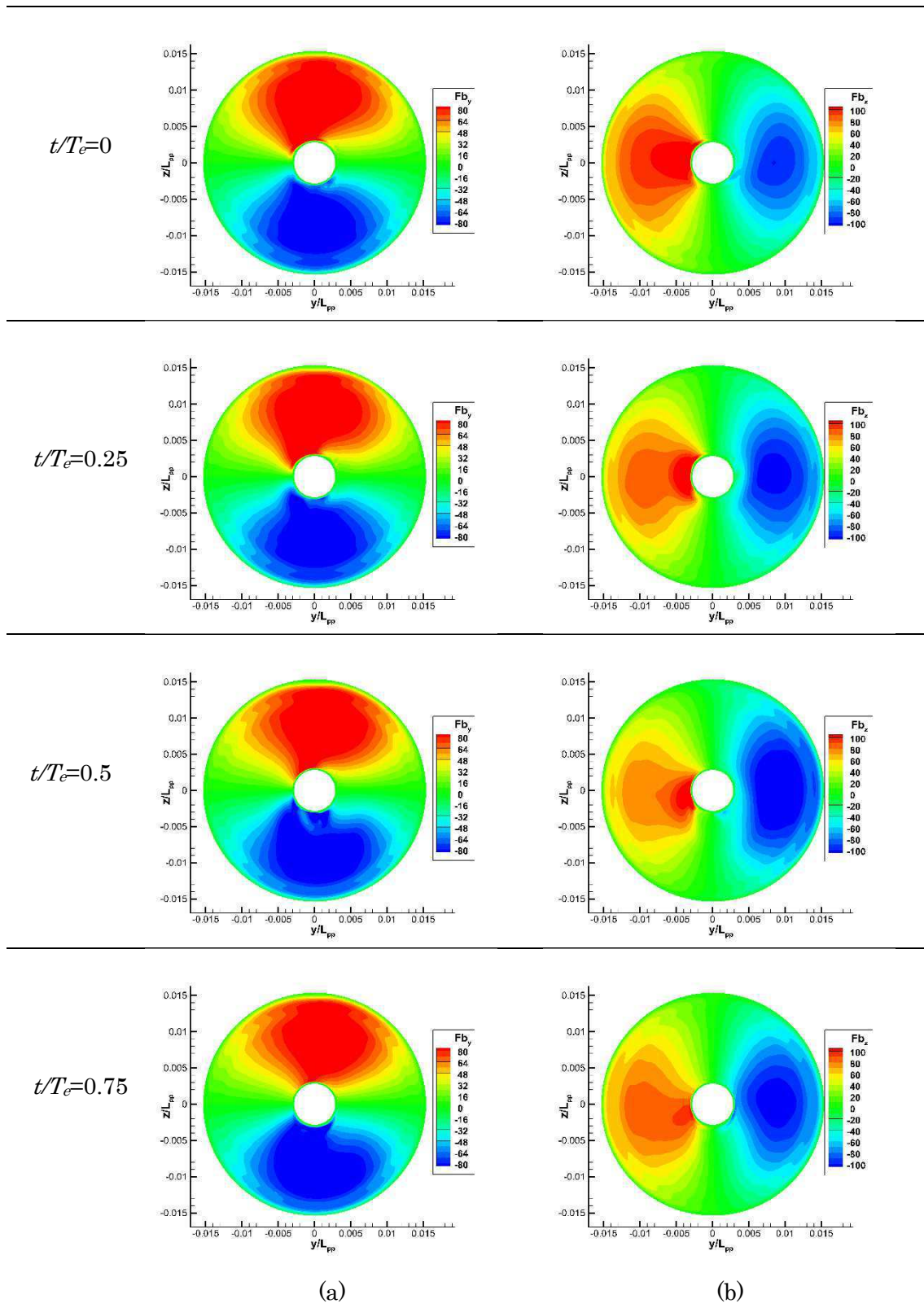
Fig. 5-16 Body-force terms in y and z direction for $\lambda/L=1.1$ in one encounter period.

For understanding the vortex structure, the Q criterion for Q=5000 colored by the axial velocity contours is illustrated in Figure 5-17 for λ/L=1.1 in one encounter period. The Q-criterion is obtained by Eq. (39), written below. It is observed that the tip-vortex shedding can only be seen as a ring shape around the propeller. It is also mentioned by Win (2014), that the tip-vortex shedding can only be estimated by the real propeller geometry. The rotating hub effect is included in the current study and can be detected in this figure. The deformation of the wake vortex system due to ship motions within one period could be captured as realized in the below figure.

Fig. 5-17 Illustration of Q-criterion for Q=5000 colored by the axial velocity contours for λ/L=1.1 in one encounter period.

96

$$Q = \frac{1}{2}\left(\left|W_{ij}\right|^2 - \left|S_{ij}\right|^2\right) \tag{39}$$

where the non-dimensional strain-rate is $S_{ij} = \frac{1}{2}\left(\frac{\partial U_i}{\partial x_j} + \frac{\partial U_j}{\partial x_i}\right)$ and the vorticity tensor is;

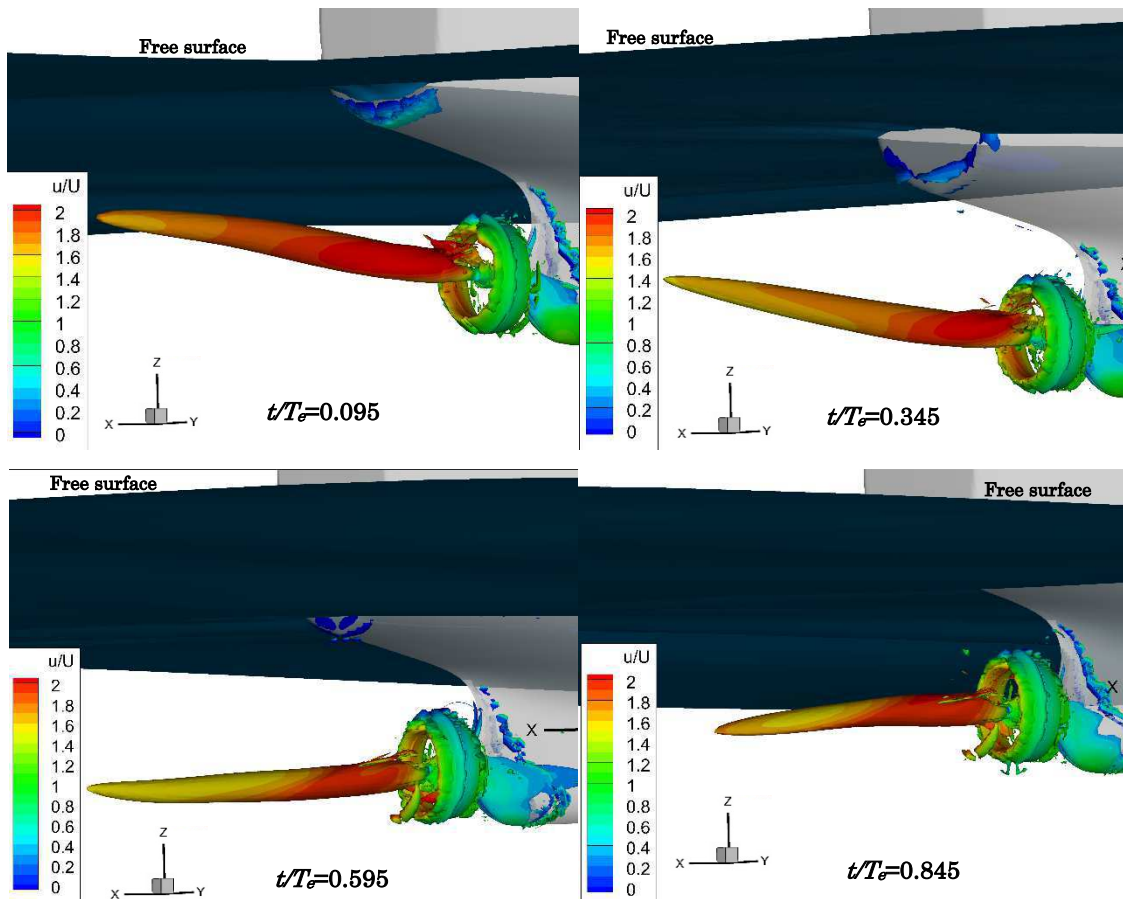$W_{ij} = \frac{1}{2}\left(\frac{\partial U_i}{\partial x_j} - \frac{\partial U_j}{\partial x_i}\right).$

5.5 DISCUSSION

The motions and the propeller performance of KVLCC2 at *Fr*=0.142 in regular head waves with wave lengths λ/L=0.6, 1.1 and 1.6 are studied using CFD and EFD. For the propeller performance in CFD, a body-force distribution model is employed. Thrust time history in waves has been analyzed and compared with the EFD results. For λ/L=0.6, the thrust value is almost minimum when the wave crest is at the propeller cross section. For λ/L=1.1 and 1.6, the thrust oscillation has higher harmonic components and phase lag which require a more comprehensive and further study, such as a ship with forced motions advancing in calm water. The fluctuation shape of the thrust can be predicted very well by CFD. And, the average thrust values for λ/L=0.6, 1.1 and 1.6, are very close to the ones from EFD results.

The flow field analyses for the self-propulsion condition in regular head waves are done by the comparison of CFD simulation and PIV measurement for various sections, including upstream and downstream of the propeller. Both results show the overall agreement.

CHAPTER 6: SUMMARY

In this dissertation, I developed a new body-force propeller model and employed this method for propeller-hull related flow problems. This chapter summarizes them and investigates possible future research.

6.1 OVERALL CONCLUSIONS

While focusing on the interaction of the propeller-hull and rudder system but not the propeller itself, it might not be necessary to capture all features of the propeller flow. But, representing the propeller effect in the velocity field is really essential. From this point of view, many researchers have been proposed numerous body-force propeller models to reduce computational cost. Thus, in this dissertation a new body-force model was developed within viscous code for simple cases; such as uniform flow case and the propeller advancing with the angle of attack. Additionally, the effect of varying solid-surface level was studied in terms of the propeller loading and power. The quasi-steady propeller model provides circumferential and radial variations in axial and tangential inflow. Within quasi-steady BET, the inflow velocity components, including induced velocity effect by time averaged infinite bladed vortex system shed by propeller blade, to the propeller were determined by CFD code and thrust and torque distributions were calculated by BET with some modification similar to potential flow theory. Rather than the inviscid propeller codes like KUM, for calculation of the body-force distribution in CFD computation, an iterative procedure based on the effective inflow velocity

distribution concept was not required in the current procedure. Within this theory, Modified-AU type propeller chord length distribution was employed, eliminating the requirement of modeling the propeller geometry. Therefore the computation took less time. The results of the open water characteristics of the proposed propeller model agreed well with the experimental data.

The effect of free surface on flow around a rotating propeller was studied numerically to investigate the applicability of new body-force concept. The propeller was represented by the time averaged body-force field and for the body-force calculations a simplified quasi-steady BET with the infinite-bladed propeller model was coupled with RANS code CFDSHIP-IOWA. Herein, the body-force calculations were carried out on Cartesian type of grid that verified the application flexibility of the method to any grid point. The open water characteristics results of the proposed model were compared with the experimental data at different immersion depths. The results of the open water characteristics of the propeller model agreed well with the experimental data for moderate loadings. The computation results showed that the locating propeller close to the free surface led to a reduction in the inflow velocity and notably affected the inflow and slipstream region on the upper half of the propeller. Therefore, this reduction of the axial-velocity led to a decrease of the axial momentum in the slipstream and the propeller performance. The presented body-force model could show the inflow and wake of the propeller is greatly affected by the free surface when the propeller centerline is close to the free surface. Consequently, it is believed that this body-force propeller model can find application in areas related to interaction of propeller-hull in ballast condition with waves where the propeller can be partially submerged.

Since it is said that body-force propeller model is promising for the application of

propeller-hull-rudder related flow problems, Win (2014) has coupled the body-force model with RANS code CFDSHIP-IOWA to investigate the flow field around S60 simple hull form. The computational results were validated against the available EFD results. Moreover, the hub effect was also included. In conclusion, the ability of the proposed propeller model has been proved in the computation of with-hub and without-hub and both gave satisfactory outcomes, especially with the hub. Also, the propeller-hull interaction was studied with and without rudder for KVLCC2 model tanker in calm water by employing the proposed body-force propeller model. The results were agreeable with experiments (Win, 2014).

Further in this dissertation, the forward speed diffraction problem of KVLCC2 model tanker at Fr=0.142 in fully-loaded condition has been done. The computations were carried out for ship advancing in regular head waves (λ/L=0.6, 1.1 and 1.6) with propeller and without propeller for (λ/L=0.6, 1.1 and 1.6). The body-force distribution model was applied to represent the propeller effect in the flow field. According to the results, it was shown that the mean value for the diffraction problem was very similar to the calm water one based on the volume averaged axial velocity analysis, Fourier analysis, and thrust coefficient predictions. The thrust coefficient oscillated due to waves and the oscillation amplitude increased for longer waves. Additionally, it was proven that the body-force model could capture the effect of propeller on the flow field by comparing the results with and without propeller.

Furthermore, the propeller performance and the ship motions of KVLCC2 model tanker in fully-loaded condition at Fr=0.142 in regular head waves with wave lengths λ/L=0.6, 1.1 and 1.6, were investigated using CFD and EFD techniques. The proposed body-force distribution model was coupled with RANS code CFDSHIP-IOWA for

propeller performance. The computational results were validated against the EFD results. Thrust time history in waves has been analyzed and compared with the EFD results. For $\lambda/L=0.6$, the thrust value was almost minimum when the wave crest was at the propeller cross section, which was similar to the diffraction problem case. For $\lambda/L=1.1$ and 1.6, the thrust oscillation had higher harmonic components and phase lag which require a more comprehensive and further study, such as a ship with forced motions advancing in calm water. According to the results, the fluctuation shape of the thrust could be predicted very well by CFD. And, the average thrust values for $\lambda/L=0.6$, 1.1 and 1.6, were very similar to the ones from EFD results. The flow field analyses for the self-propulsion condition in all wavelength cases were completed by the comparison of CFD simulation and PIV measurement for various sections, including upstream and downstream of the propeller. Overall the results showed good agreement.

6.2 FUTURE WORK

The computation of propeller-hull-rudder interaction has been done in calm water, in which a real propeller geometry is employed to predict the complicated flow field. In this dissertation, I employed a body-force propeller model in an interactive and iterative way to investigate the complex flow field around the self-propelled ship in waves with fixed or free to heave and pitch motion conditions. So, our near future study might be using a real propeller geometry to predict numerically the propeller performance and motions of a self-propelled ship in waves. As it is mentioned above, a study on a ship with forced motions advancing in calm water can be carried out as well. Besides, this body-force concept is very simple and flexible which allows us to employ it to any types of grid and

might find application in propulsion field such as; free-running computations, ship to

ship interaction cases and so on.

References

Benini E.: Significance of Blade Element Theory in Performance Prediction of Marine Propellers. Ocean Engineering, Vol. 31, pp. 957-974, 2004.

Carrica P. M. et al.: An Unsteady Single-Phase Level Set Method for Viscous Free Surface Flows. International Journal of Numerical Methods for Fluids, Vol. 53, pp. 229-256, 2007.

Carrica P.M. et al.: Ship Motions using Single-Phase Level Set with Dynamic Overset Grids. Computers & Fluids, Vo. 36, pp. 1415-1433, 2007.

Carrica P. M. et al.: CFD Analysis of Broaching for a Model Surface Combatant with Explicit Simulation of Moving Rudders and Rotating Propellers. Computer &Fluids, Vol. 53, pp. 117-132, 2012.

Chen C. et al.: Solutions of Reynolds-averaged Navier-Stokes Equations for Three Dimensional Incompressible Flows. Journal of Computational Physics, Vol. 88, pp. 305-336, 1990.

Dai C.M.H. et al.: Computation of an Integrated Ducted Propulsor/Stern Performance in Axisymmetric Flow. Proceedings Propeller/Shafting 91, Virginia Beach, Va., 1991.

Goldstein S.: On the Vortex Theory of Screw Propellers. Proceedings of the Royal Society of London, Vol. 123, Issue No. 792, pp. 440-465.

Hayashi Y.: Phase-averaged 3DPIV Flow Field Measurement for KVLCC2 Model in Waves. M.Sc. thesis (in Japanese), Osaka University, 2012.

Hough G. and Ordway D.: The generalized actuator disk. Technical Report TAR-TR 6401,

Therm Advanced Research, Inc., 1964.

Menter F. R.: Two-Equation Eddy Viscosity Turbulence Models for Engineering Applications. AIAA Journal, Vol. 32, No. 8, August 1994.

Moriyama F.: On an Approximate Numerical Method for Estimating the Performance of Marine Propellers. National Maritime Research Institute Report, Vol. 16, No. 6, pp. 361-376, 1979.

Naito S. and Nakamura S.: Open Water Characteristics and Load Fluctuations of Propeller at Racing Condition in Waves. Journal of the Japan Society of Naval Architects and Ocean Engineers, No. 192, pp. 51-63, 1979.

Ohmori T. and Miyata H.: Oblique Tow Simulation by a Finite-Volume Method. Journal of the Society of Naval Architectures of Japan, Vol. 173, pp. 27-34, 1993.

Okawa H.: On Fluctuating Flow Field around Self-propelled Ship Stern in Waves. M.Sc. thesis (in Japanese), Osaka University, 2015.

Paterson G.: General-purpose Parallel Unsteady RANS Ship Hydrodynamics Code: CFDSHIP-IOWA, IIHR Report No. 432, pp.2-21, 2003.

PETSc. Retrieved from http://www.mcs.anl.gov/petsc/.

Phillips A. B.: Comparison of CFD Simulations and In-Service Data for the Self-Propelled Performance of an Autonomous Underwater Vehicle. 27th Symposium of Naval Hydrodynamics, Seoul, Korea, pp., 5-10 October 2008.

Phillips A. B.: Evaluation of Maneuvering Coefficients of a Self-propelled Ship Using a Blade Element Momentum Propeller Model Coupled to a Reynolds Averaged Navier Stokes Flow Solver. Ocean Engineering, Vol.36, No. 15-16, pp. 1217-1225, 2009.

Piquet J. et al.: Computation of Viscous Flows past Axis-Symmetric Bodies with and without a Propeller in Operation. Numerical Methods in Laminar and Turbulent Flows, Vol. 5, No. 1, pp. 644-655.

Sadat-Hosseini H. et al.: CFD Verification and Validation of Added Resistance and Motions of KVLCC2 with Fixed and Free Surge in Short and Long Head Waves. Ocean Engineering, Vol. 59, pp. 240-273, 2013.

Simonsen D. and Stern F.: RANS Maneuvering Simulation of Esso Osaka with Rudder and a Body-Force Propeller. Journal of Ship Research, Vol. 49, No. 2, pp. 98-120, 2005.

Stern F. et al.: A Viscous-Flow Approach to the Computation of Propeller-Hull Interaction. Journal of Ship Research, Vol. 32, pp. 246-262, 1988a.

Stern F. et al.: Computation of Viscous Flow around Propeller-Shaft Configurations. Journal of Ship Research, Vol. 32, pp. 263-284, 1988b.

Stern F. et al.: Computation of Viscous Flow around Propeller-Body Configurations: Iowa Axis-symmetric Body. Journal of Ship Research, Vol. 35, No. 2, pp. 151-161, 1991.

Tokgoz E. et al.: A New Method to Predict the Propeller Body-force Distribution for Modelling the Propeller in Viscous CFD Code without Potential Flow Code. Proceedings of the 2nd East Asia International Student Symposium on Maritime Sciences (EAISS2012), pp. 20-24, Kobe, Japan, 2012.

Tokgoz E. et al.: A New Method to Predict the Propeller Body Force Distribution for Modeling the Propeller in Viscous CFD Code without Potential Flow Code. Journal of the Japan Society of Naval Architects and Ocean Engineers, Vol. 19, pp. 1-7, 2014.

Tokgoz E. et al.: Application of New Body-force Concept to the Free Surface Effect on the

Hydrodynamic Force and Flow around a Rotating Propeller. Proceedings of 24th International Ocean and Polar Engineering Conference, pp. 607-612, Busan, South Korea, 2014.

Tokgoz E. et al.: Computation of the Propeller-hull Interaction Flow in Waves for Diffraction Problem Using Body-Force Distribution Model. Conference Proceedings of the Japan Society of Naval Architect and Ocean Engineering, Vol. 20, pp. 251-254, Kobe, Japan, 2015.

Tokgoz E. et al.: Computation and SPIV Measurement of the Flow Field around Self-Propelled Ship in Waves Using Body-force Model. Conference Proceedings of the Japan Society of Naval Architects and Ocean Engineers, Vol. 20, pp. 255-258, Kobe, Japan, 2015.

Weymouth G. et al.: RANS CFD Predictions of Pitch and Heave Motions in Head Seas. Journal of Ship Research, Vol. 49, pp. 80-97, 2005.

Win Y. N.: Computation of the Propeller-Hull and Propeller-Hull-Rudder Interaction Using Simple Body-Force Distribution Model. Doctoral Dissertation, Graduate School of Engineering, Osaka University, 2014.

Wu P.-C. et al.: Nominal Wake Fluctuation Due to Waves: Volume Mean and Distribution Based on CFD and PIV. Conference Proceeding of the Japan Society of Naval Architect and Ocean Engineering, Vol. 16, Hiroshima, Japan, 2013.

Yamazaki R.: On the Propulsion Theory of Ships on Still Water (Improved Theoretical Method), Memoirs of the Faculty of Engineering, Kyushu University, Vol. 34, No. 1, pp. 65-88, 1977.

Yang C. I. et al.: A Navier-Stokes Solution of Hull-Ring Wing-Thruster Interaction.

Proceedings 18th ONR Symposium on Naval Hydro., Ann Arbor, Mich., pp. 687-696.

Yazaki A.: The Design of AU-Type Ship Screw Propellers. Report of Transportation Technical Research Institute. Vol. 11, No. 7, 1961.

Yokota S. et al.: A Simple Method to Include the Propeller Effect in CFD Code - computation of body-force distribution on any grid point-. Conference Proceedings of the Japan Society of Naval Architects and Ocean Engineers, Vol. 17, pp. 361-364, 2013.

Zhang D.-H. et al.: A Method for Computing Stern Flows with an Operating Propeller. Royal Institution Naval Architects, 1991.

Acknowledgements

List of publications

JOURNAL PAPERS

Tokgoz, E., Win, Y. N., Kuroda, K. and Toda, Y., (2014), "A New Method to Predict the Propeller Body Force Distribution for Modeling the Propeller in Viscous CFD Code without Potential Flow Code", Journal of the Japan Society of Naval Architects and Ocean Engineers, Vol. 19, pp. 1-7.

Win, Y., *Tokgoz, E.,* Wu, P.-C., Stern, F. and Toda, Y., (2013), "Computation of Propeller-Hull interaction using Simple Body-Force Distribution Model around Series 60 C_B=0.6", Journal of the Japan Society of Naval Architects and Ocean Engineers, Vol. 18, pp. 17-27.

CONFERENCE PAPERS

Tokgoz, E., Win, Y. N., Kuroda, K. and Toda, Y., (2012), "A New Method to Predict the Propeller Body-force Distribution for Modelling the Propeller in Viscous CFD Code without Potential Flow Code", Proceedings of the 2nd East Asia International Student Symposium on Maritime Sciences (EAISS2012), pp. 20-24, Kobe, Japan.

Tokgoz, E., Win, Y. N., Kuroda, K. and Toda, Y., (2013), "A New Method to Predict the Propeller Body-force Distribution for Modelling the Propeller in Viscous CFD Code without Potential Flow Code", Conference Proceedings of The Japan Society of

Naval Architects and Ocean Engineers, Vol. 16, pp. 215-218, Hiroshima, Japan.

Yokota, S., *Tokgoz, E.,* Win, Y. and Toda, Y., (2013), "A Simple Method to Include the Propeller Effect in CFD Code: Computation of Body Force Distribution on any Grid Point", Conference Proceedings of the Japan Society of Naval Architects and Ocean Engineers, Vol. 17, pp. 361-364.

Tokgoz, E., Wu, P.-C., Yokota, S. and Toda, Y., (2014), "Application of New Body-force Concept to the Free Surface Effect on the Hydrodynamic Force and Flow around a Rotating Propeller", Proceedings of 24th International Ocean and Polar Engineering Conference, pp. 607-612, Busan, South Korea.

Win, Y., *Tokgoz, E.,* Wu, P.-C., Stern, F. and Toda, Y., (2014), "Computation of Propeller-Hull interaction using Simple Body-Force Distribution Model around modified Series 60 C_B=0.6 with hub", Proceedings of 24th International Ocean and Polar Engineering Conference, pp. 759-765, Busan, South Korea.

Tokgoz, E., Wu, P.-C. and Toda, Y., (2015), "Computation of the Propeller-Hull Interaction Flow in Waves for Diffraction Problem Using Body-force Distribution Model", Conference Proceedings of the Japan Society of Naval Architects and Ocean Engineers, Vol. 20, pp. 251-254, Kobe, Japan.

Tokgoz, E., Wu, P.-C., Okawa, H., Tamaki, K. and Toda, Y., (2015), "Computation and SPIV Measurement of the Flow Field around Self-Propelled Ship in Waves Using Body-force Model", Conference Proceedings of the Japan Society of Naval Architects and Ocean Engineers, Vol. 20, pp. 255-258, Kobe, Japan.

Curriculum vitae

Education

Doctoral Course, Naval Architecture and Ocean Engineering   **2012 - present**
Osaka University (OU) - Suita, Japan
Adviser: Prof. Yasuyuki Toda

> *Areas of research: Computational fluid dynamics, ship hydrodynamics.*
> *Current topic: CFDSHIP-IOWA V4.5, computation of self-propelled ship in*
> *head waves using interactive propeller model.*
> ***Scholarship by MEXT (Japanese Government Scholarship) (2010~2015).***

Master of Science, Naval Architecture and Ocean Engineering   **2010-2012**
Osaka University (OU) - Suita, Japan
Adviser: Prof. Yasuyuki Toda

> *Thesis: "The new method to predict the propeller body force distribution for modeling the*
> *propeller in viscous CFD code without potential flow code"*
> *Areas of research: Computational fluid dynamics, ship hydrodynamics, propeller*
> *performance code.*

Bachelor of Science, Naval Architecture and Marine Engineering   **2005 -2010**
Istanbul Technical University (ITU) – Istanbul, Turkey
Overall GPA: 3.50/4.0

> *Thesis: "2D CFD applications of a flat plate"*

Bachelor of Science, Ship Science   **2007-2008**
Transfer to University of Southampton – Southampton, UK within Erasmus Program
Overall GPA: 74.7/100

Work Experience

2007.06 - 2007.07	Internship at Haliç Shipyard / Istanbul/Turkey
2008.08 - 2008.09	Internship at Eregli Shipyard / Zonguldak/Turkey
2009.08 - 2009.09	Internship at Gentech Ltd. (Soraya Yachts) / Antalya/Turkey